Title
A Multi-Wavelength Spectroscopic and Photometric Study of Star Formation and Dust in Galaxies in the Early Universe

Author
Shivaei, Irene

Publication Date
2017

UNIVERSITY OF CALIFORNIA
RIVERSIDE

A Multi-Wavelength Spectroscopic and Photometric Study of Star Formation and Dust in Galaxies in the Early Universe

A Dissertation submitted in partial satisfaction
of the requirements for the degree of

Doctor of Philosophy

in

Physics

by

Irene Shivaei

September 2017

Dissertation Committee:

Prof. Naveen Reddy, Chairperson
Prof. Bahram Mobasher
Prof. Brian Siana
Prof. Laura Sales

The Dissertation of Irene Shivaei is approved:

Committee Chairperson

University of California, Riverside

Acknowledgments

I would like to gratefully thank all the people who have helped me in this journey. Foremost, I thank my academic advisor, Prof. Naveen Reddy. It has been an honor to be your first Ph.D. student. You taught me how to be an independent and determined researcher. Without your guidance, I would not be standing where I am today in my professional life.

I am deeply thankful to the endless support of my committee member, Prof. Bahram Mobasher, and his lovely wife, Azin. I am very grateful for all your help and kindness since my very first days at UCR. I also thank all the astronomy faculty of the Physics department for providing a friendly and cooperative atmosphere in the department. Special thanks goes to my other committee members, Profs. Brian Siana and Laura Sales, whose enthusiasm and excitement were always inspiring.

The results of this thesis were accomplished with the help and support of my collaborators. I was very fortunate to be a part of the MOSDEF collaboration and work closely with the talented and eminent members of the team. I particularly thank Prof. Mariska Kriek who hosted me at UC Berkeley during the summer of 2015, an experience that marked a turning point in my career.

My friends at UC Riverside, who are an important part of my life, had a great role in making my experience so enjoyable. I cannot say enough how fortunate I was to have my best friend, Mostafa Khezri, by my side all these years. You were always there in hardness and in happiness, encouraging me to aim higher. I will miss our times together, your perfectionism, and your immediate solutions and justifications to almost every problem! I am very grateful for the time I spent with our small Persian community ('bar-o-bach'):

Shooby (thanks for your continuous advice and friendship), Hooshang, Behnam, Mohammad Reza, and Ali. You make living in a foreign country much easier and more enjoyable. I am also thankful to my new friends, Abtin and Nassim, who made this past couple of months fun and enriching and making it very hard to leave Riverside!

I finish with my homeland country, Iran, and all the amazing people there who made me the person I am today. I cannot imagine a better family to grow up in.

First, my parents, Sofia and Vahid, you are my role models in my professional and personal life. Your wisdom has always been the light on my path. Your constant support and encouragement give me the courage and confidence to follow my passions.

My little sister, Shirin, you are my soulmate. Your energy and joy make my life colorful!

My dearest aunt, Ame Zari, I grew up in your home. I do not know any human being with a heart kinder than yours. Your endless love taught me to be gracious, caring, and kind to others.

My cousins, Nazanin, Rouzbeh, and Negar, you are no different to me than siblings. After all these years, I miss every second of being with you.

My aunt, Khaleh Mansoureh, I wish you were here with us. You were the strongest woman I know, and you made it possible for me to come to this country to pursue my passion.

My lovely uncle, Amu Mohammad, and his kind and bright wife, Farzaneh jun, who helped me to settle down in Riverside, as if I was their own daughter. Having you by my side these years was invaluable.

My kind and talented uncle, Dai Sassan, I do not even remember how many times I stayed with you and Negar jun at your house (from Sanandaj to Buffalo to Newton)! I have so many good memories with you. Thanks for always being there for me and Shirin.

My teachers, Babak Tafreshi and Pejman Norouzi, you ignited the passion for astronomy in me. I remember my first astronomy classes with you when I was 14, and the observing nights in the deserts of Iran when, for the first time, I was mesmerized by the beauty of the night sky. I always looked up to your enthusiasm and dedication and owe my passion for astronomy to you.

My undergraduate advisor at University of Tehran, Prof. Mohammad Taghi Tavassoly, my interest in optics and experimental physics started in your lab, and I learned much from your scientific and professional character.

Last, but not least, my awesome friends who I left behind in Iran (some are now living in other parts of the world), you are always in my mind and my heart: Zeinab, Helia, Banafsheh, Pouria, Siavash, Amin, Nasrin, Kazem, Houman, and many more.

I acknowledge support from the National Science Foundation (through NSF Graduate Research Fellowship DGE-1326120) for providing the funding that allowed me to undertake this research. This thesis is based partly on research that has been published in the Astrophysical Journal: 2017ApJ...837..157S, 2016ApJ...820L..23S, 2015ApJ...815...98S, and 2015ApJ...804..149S.

To my parents

Thanks for your endless love, support, and encouragement

ABSTRACT OF THE DISSERTATION

A Multi-Wavelength Spectroscopic and Photometric Study of Star Formation and Dust in Galaxies in the Early Universe

by

Irene Shivaei

Doctor of Philosophy, Graduate Program in Physics
University of California, Riverside, September 2017
Prof. Naveen Reddy, Chairperson

Redshift of $z \sim 2$ is an important era in the history of the universe, as it contains the peak of star formation rate (SFR) and quasar activity. In this work, we investigate the properties of galaxies during this era from two different, yet complementary, aspects: star formation and stellar mass (M_*) assembly, and dust enrichment. We utilize rest-UV to optical photometric data from the *Hubble Space Telescope* and Keck Observatory, and a wealth of rest-optical spectroscopic data from the MOSFIRE Deep Evolution Field survey using Keck/MOSFIRE spectrometer. We incorporate mid- and far-IR data from the *Spitzer* and *Herschel* telescopes to obtain a complete census of obscured and unobscured star formation. By comparing Hα-derived SFRs with those inferred from panchromatic SED modeling, we show that the Balmer decrement accurately predicts the obscuration of the nebular lines and can be used to robustly calculate SFRs of galaxies at $z \sim 2$ with SFRs up to $\sim 200\,M_\odot\,\mathrm{yr}^{-1}$. We dissect the scatter and slope of the SFR-M_* relation at $z \sim 2$, using multi-wavelength SFR tracers (UV, Hα, 24μm, and far-IR). We find a large intrinsic scatter of 0.36 dex and a shallower slope of ~ 0.7 than found previously. Moreover, for the first time, we investigate the variation of PAH emission at 7.7μm, traced by *Spitzer*/MIPS 24μm, in galaxies spanning a wide range in metallicity at $z \sim 2$. Our results indicate a higher IR luminosity density at $z \sim 2$ than previously measured, corresponding to a $\sim 30\%$ increase in the SFR density. Lastly, we utilize Hα and Hβ spectroscopic measurements to constrain the ionizing photon production efficiency ($\xi_{\rm ion}$) of galaxies at $z \sim 2$. $\xi_{\rm ion}$ is elevated in galaxies with blue UV slopes, low metallicity, and high ionization parameter. We show that the scatter in $\xi_{\rm ion}$ distribution reflects galaxy-to-galaxy variations in stellar properties, including IMF, metallicity, binarity, and star formation burstiness. Our results pave the way for future observations with the *James Webb Space Telescope* to improve our understanding of dust enrichment during the epoch of peak of star formation activity, and to investigate the role of galaxies in the reionization era at $z \gtrsim 6$.

Contents

List of Figures

List of Tables

Chapter 1

Introduction

1.1 Overview

Understanding the formation and evolution of galaxies throughout cosmic time is among the most challenging questions in modern cosmology. To capture a complete view of galaxies, we need to observe them across a wide range of wavelengths, from ultraviolet (UV) to infrared (IR). UV is dominated by emission from massive newly-born stars, near-IR originates from older stars, and stellar emission that is absorbed by dust grains inside galaxies re-emits at longer IR wavelengths (Figure 1.1, top).

Over the past decade, technological advances have put us in a unique position to capture a panchromatic view of galaxies across cosmic time. I use powerful ground- and space-based facilities, such as the Keck observatory, the *Hubble*, *Spitzer*, and *Herschel* space telescopes to observe the sky across the electromagnetic spectrum, and explore star formation and dust enrichment during the epoch of peak of star formation activity in the

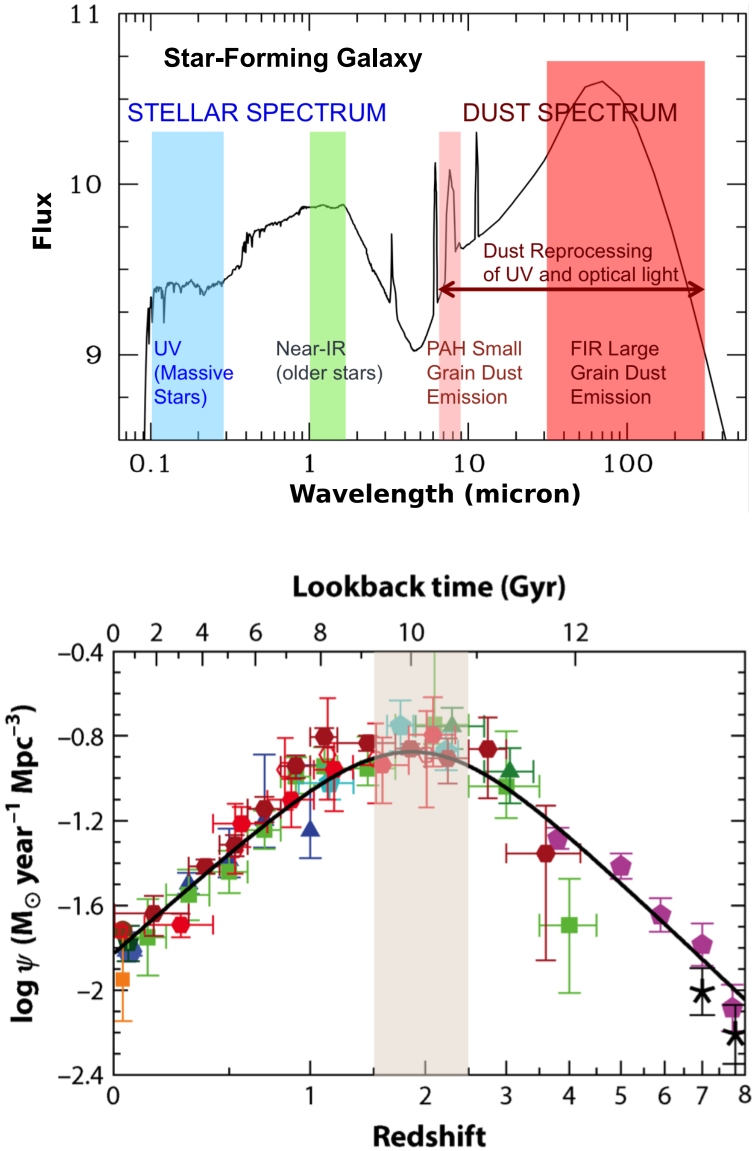

Figure 1.1 *Top:* spectral energy distribution (SED) of a typical star-forming galaxy. Each part of the spectrum is dominated by the emission from different types of stars and dust particles. Credit: N. Reddy. *Bottom:* evolution of the cosmic star-formation rate density. The shaded region marks the epoch of peak of star formation activity. I study properties of galaxies during this epoch. Source: Madau & Dickinson (2014).

universe (redshift of $z \sim 2$). This is an important era in the history of the universe, as galaxies were in the process of assembling most of their stellar mass, the structural patterns observed among local galaxies were not yet in place, and quasar activity was at its peak (Madau & Dickinson 2014, Figure 1.1, bottom).

1.1.1 How Do We Measure Star Formation Rate?

Galaxies are dynamically bound systems consisting of stars and gas. They grow and accumulate mass by converting their gas into stars (i.e., star formation). Young galaxies with large reservoirs of gas, or those that have recently merged with another galaxy, have high rates of star formation, while older galaxies are quiescent with little or no star formation.

The bolometric luminosity of star-forming galaxies is dominated by their massive stars, mostly emitted in UV or absorbed by dust and reemitted in IR. Massive stars are proper diagnostics of current star formation rate (SFR) as they have relatively short main sequence lifetimes. By assuming a distribution of stellar masses we extrapolate the formation rate of massive stars to that of all stars and calculate the total SFR.

The most commonly-used SFR diagnostics are UV stellar continuum and nebular emission lines (e.g., hydrogen Balmer and Paschen lines; Kennicutt 1998; Kennicutt & Evans 2012). Nebular lines originate from H II regions around the most massive early-type O stars with lifetimes of $\sim 10\,\mathrm{Myr}$, making them almost "instantaneous" SFR indicators. On the other hand, UV light emerges from both O and B type stars over longer timescales of $\sim 50-100\,\mathrm{Myr}$. Although both SFR tracers are frequently used in high-redshift studies, a major challenge is that UV and optical light are easily absorbed by dust grains inside galaxies. Therefore, to measure the *intrinsic* SFR, it is necessary to correct the observed light for dust absorption (Cardelli et al. 1989; Calzetti et al. 2000; Gordon et al. 2003; Reddy et al. 2010, among many more). Correcting for dust can be a challenging task, especially for high redshift galaxies, that I tried to address in the following chapters.

1.1.2 Why Is Dust Important?

The inter-stellar medium (ISM) is pervaded by dust. Dust grains are solid particles with sizes of $\lesssim 1\,\mu$m that absorb the optical and UV light emitted from stars and re-radiate the absorbed light at IR wavelengths, thereby modifying our view of galaxies. IR emission from dust particles points to obscured stellar regions that we would otherwise miss. More fundamentally, dust particles have important roles in the process of star formation: dust grains are catalysts for formation of certain molecules in the ISM, and they are important for cooling and heating processes, ISM gas dynamics, and charge transfer.

Two main pieces of observational evidence of the presence of the interstellar dust in galaxies are *attenuation* (extinction) of UV and optical starlight and thermal *emission* at mid-IR to sub-millimeter wavelengths. There are spectral features in both the dust extinction and emission that provide clues about the composition and size distribution of dust grains.

A key component of the dust population is polycyclic aromatic hydrocarbon (PAH) molecules. PAHs are organic molecules that contain ~ 50 carbon atoms, arranged in a honey comb structure of aromatic rings with peripheral hydrogen atoms. These molecules are commonly found on Earth in coal, tar, and the exhaust fumes of car engines (Haynes & Wagner 1981). In space, PAHs are found in various environments, including the general

ISM, reflection nebulae, supernovae remnants, around young and massive stars, and around evolved carbon-rich stars (Tielens 2008). PAHs can be transiently heated by absorbing single UV photons, and will subsequently cool by emitting an IR photon. Therefore, PAHs are mainly observed through their strong emission in certain mid-IR bands at 3.3, 6.2, 7.7, 8.6, and 11.2 μm. These emission features are characteristic of the vibrational modes of PAHs. PAHs contribute substantially to dust attenuation, account for up to $\sim$ 20% of the IR emission of galaxies (Smith et al. 2007; Dale et al. 2009), play an important role in the physics and chemistry of ISM by providing surfaces for chemical reactions (such as the formation of H_2 molecules), carrying an important fraction of the gas electronic charge, and efficiently heating the ISM gas in regions where UV starlight is present (Tielens 2005). Studying PAHs is therefore crucial for understanding the evolution of interstellar gas.

1.1.3 Necessity of Near-IR Spectroscopy to Study $z \sim 2$ Galaxies

Many of the physical characteristics of galaxies are revealed from their optical light. Emission lines in the optical spectra of galaxies, such as those of ionized hydrogen, oxygen, and nitrogen, can be used to determine the amount of dust, SFR, chemical composition, ionization state of the gas, and the ratio of ionizing to non-ionizing photons. However, due to the expansion of the universe, the light of distant galaxies shifts to longer wavelengths. Therefore, to observe the rest-frame optical spectra of galaxies at $z \sim 2$, we require near-IR observations.

Until recently, obtaining large samples of near-IR spectra of galaxies at $z \sim 2$ was extremely challenging, owing to the relatively lower sensitivity and lack of multiplexing capabilities of near-IR spectrographs on 10-meter-class telescopes. Consequently, previous similar studies had small samples, consisting of only ~ 100 galaxies (e.g., Erb et al. 2006; Kriek et al. 2008). During my Ph.D. years, I played a leading role in the multi-institutional MOSFIRE Deep Evolution Field (MOSDEF) survey (Kriek et al. 2015). MOSDEF is a large spectroscopic program that used the multi-object near-infrared MOSFIRE spectrometer (McLean et al. 2012) on Keck to obtain rest-optical spectra of ~ 1800 galaxies at $1.4 \leq z \leq 3.8$ and study their stellar, gaseous, metal, dust, and black hole content. At the time of writing this thesis, MOSDEF is the largest survey of the rest-frame optical properties of galaxies at $1.37 \leq z \leq 3.80$.

1.2 Outline of the Thesis

Rate of Star Formation in Distant Galaxies: As discussed in Section 1.1, the UV, optical emission lines (Hα), and IR emission are often used as indicators of SFR in galaxies. However, calibration of these SFR indicators is a subject of debate in high-redshift studies. The most commonly-used calibrations are derived from local galaxies, and hence, can be affected by differences in star formation histories, chemical compositions, and distribution of stars and dust between nearby and distant galaxies. In **Chapter 2** (Shivaei et al. 2015a), we compare the UV, optical, and IR SFR indicators for a large sample of galaxies at $z \sim 2$, and investigate the validity of each of these SFR diagnostics for different populations of galaxies (such as galaxies with different ages). Moreover, in **Chapter 4** (Shivaei et al. 2016), we show that the optical Hα and Hβ emission lines, which are often used as SFR diagnostics in local galaxies, accurately trace the total SFR of even the dusty galaxies at

$z \sim 2$. This is the first time that optical SFR indicators are compared with SFRs inferred from the best-fit UV-to-far-IR galaxy templates at $z \sim 2$.

Star Formation and Mass Assembly: Galaxies grow in two plausible modes: by merging with other galaxies, or by gravitationally accreting cold gas from the intergalactic medium and converting it into stars. In the latter "cold gas accretion" scenario, star formation is a steady function of time and galaxies assemble their stellar mass smoothly. A main consequence of this smooth mass assembly is that there is a correlation between SFR and stellar mass of galaxies, commonly called the "star-forming main sequence." Galaxies that have undergone a recent merger are outliers in this correlation, as their SFR has rapidly increased. Comparing the observational results with those of simulations gives us insight about the processes that govern galaxy formation and growth, such as feedback processes from galactic winds.

In **Chapter 3** (Shivaei et al. 2015b), we study the star-forming main sequence using accurate and robust SFR measurements (from Hα and Hβ) for a large and representative sample of galaxies at $z \sim 2$. We determine the properties of this relation, as well as possible observational assumptions that can lead to inconsistent results.

Dust in Distant Galaxies: As stars evolve, they synthesize elements heavier than hydrogen and helium (i.e., metals). These elements are eventually injected into the ISM, either after the star death or during its life through stellar winds, enriching the ISM and increasing the gas-phase "metallicity" of galaxies. The heavy elements are also responsible for the production of dust particles.

In **Chapter 5** (Shivaei et al. 2017), we investigate variations of the PAH intensity in galaxies with different metallicities. We find that in metal-poor galaxies, the PAH emission is suppressed relative to that of large dust grains. The paucity of PAHs can be due to (1) fewer carbon atoms available in the ISM, or (2) the destruction of PAHs with more energetic photons that are present in metal-poor environments. This is the first time that variations of PAH emission is explored in distant galaxies. These results have important implications for high-redshift studies that use the PAH emission as an indicator of SFR.

Ionizing Photon Production Efficiency: The emission rate of ionizing photons that are produced by massive stars impact our observables, such as SFR and gas-phase metallicity. To quantify the production efficiency of ionizing photons, $\xi_{\rm ion}$ parameter is defined as the production rate of ionizing photons per unit UV luminosity (see Robertson et al. 2013; Bouwens et al. 2016a). Constraining the value of $\xi_{\rm ion}$ helps us to better understand the properties of massive star populations and improve our stellar population synthesis models. $\xi_{\rm ion}$ is also an important input in models of reionization (e.g., Robertson et al. 2015).

In **Chapter 6**, we use the large and unique spectroscopic Hα and Hβ dataset of MOSDEF to estimate the rate of Lyman continuum photons and constrain $\xi_{\rm ion}$ at $z \sim 2$. We explore $\xi_{\rm ion}$ relation with commonly measured properties of galaxies, such as UV continuum slope, stellar mass, ionization parameter, and metallicity. Moreover, we investigate the plausible physical sources of the large intrinsic scatter in $\xi_{\rm ion}$ distribution by comparing our observations with predictions from the stellar population synthesis models. Our results demonstrate the utility of Balmer emission lines in constraining $\xi_{\rm ion}$ for future observations with *JWST* at higher redshifts.

Chapter 2

Investigating Hα, UV, and IR star-formation rate diagnostics for a large sample of $z \sim 2$ galaxies*

Abstract We use a sample of 262 spectroscopically confirmed star-forming galaxies at redshifts $2.08 \leq z \leq 2.51$ to compare Hα, UV, and IR star-formation-rate diagnostics and to investigate the dust properties of the galaxies. At these redshifts, the Hα line shifts to the K_s-band. By comparing K_s-band photometry to underlying stellar population model fits to other UV, optical, and near-infrared data, we infer the Hα flux for each galaxy. We obtain the best agreement between Hα- and UV-based SFRs if we assume that the ionized gas and stellar continuum are reddened by the same value and that the Calzetti attenuation

*A version of this chapter was published in: Shivaei, I., Reddy, N. A., Steidel, C. C., & Shapley, A. E., *The Astrophysical Journal* 804, 149 (2015) curve is applied to both. Aided with MIPS 24 μm data, we find that an attenuation curve steeper than the Calzetti curve is needed to reproduce the observed IR/UV ratios of galaxies younger than 100 Myr. Furthermore, using the bolometric star-formation rate inferred from the UV and mid-IR data (SFR_{IR}+SFR_{UV}), we calculated the conversion between the Hα luminosity and SFR to be $(7.5 \pm 1.3) \times 10^{-42}$ for a Salpeter IMF, which is consistent with the Kennicutt (1998) conversion. The derived conversion factor is independent of any assumption of the dust correction and is robust to stellar population model uncertainties.

2.1 Introduction

One of the most important diagnostics in understanding the evolution of galaxies is the star-formation rate (SFR). The evolution of the SFR of galaxies can give clues as to how galaxies were enriched with heavy elements, how they build up their stellar mass through cosmic time, and helps us to understand the bolometric output of galaxies. At redshift $z \sim 2$, when the universe was just ~ 3 Gyr old, star-formation activity in the universe was at its peak and galaxies were in the process of assembling most of their stellar mass (see Reddy & Steidel 2009; Bouwens et al. 2010; Shapley 2011; Madau & Dickinson 2014). Studying this critical epoch is essential to gaining a better understanding of the evolution of the progenitors of the local galaxy population.

The ultra-violet (UV) continuum (1500 to 2800 Å) intensity of a galaxy is one of the most commonly used diagnostics for the SFR as it is observable over a wide range of redshifts and intrinsic luminosities. It is sensitive to massive stars ($M_* \gtrsim 5\,M_\odot$), making it a direct tracer of current SFR. By extrapolating the formation rate of massive stars to lower masses, for an assumed form of the initial mass function (IMF), one can estimate the total SFR (Madau et al. 1998). Another widely used diagnostic for measuring the SFR is nebular emission, with Hα being the most common because of its higher intensity compared to the other hydrogen recombination lines such as Hβ, Paα, Paβ, etc., and it is easier to interpret than the Lyα line. Hα is an "instantaneous" tracer of SFR because it is sensitive only to the most massive stars ($M_* \gtrsim 10\,\mathrm{M_\odot}$). However, it becomes more challenging to observe Hα from the ground at $z \gtrsim 1$ because the line is redshifted to the near-IR where the terrestrial background is much higher than at optical wavelengths.

The main disadvantage of using UV/optical luminosities as tracers of the SFR is their sensitivity to dust attenuation. The dust absorption cross-section is larger for shorter wavelengths and choosing the appropriate attenuation curve to correct the observed luminosities plays an important role in determining intrinsic physical quantities. Aside from the assumed attenuation curve, the geometry of dust with respect to the stars can lead to different color excesses, $E(B-V)$, between the ionized gas and the stellar continuum. $E(B-V)$ is the color excess measured between the B and V bands, $E(B-V) \equiv A_B - A_V$, where A_λ is the total extinction at wavelength λ in magnitudes. In particular, the nebular recombination lines arise from the HII regions around the most massive O and early-type B stars (with masses of $\mathrm{M_*} \gtrsim 10\,\mathrm{M_\odot}$ and main sequence lifetimes of $\lesssim 10\,\mathrm{Myr}$). On the other hand, for a Salpeter IMF, solar metallicity, and a constant or rising star-formation history, the UV continuum in starburst galaxies originates from stars over a broader range of mass that includes later-type B stars with lifetimes $\lesssim 100\,\mathrm{Myr}$ (Kennicutt 1998; Madau & Dickinson 2014). These older non-ionizing stars have more time to migrate to regions of lower dust density in the galaxy, while H-ionizing stars with shorter lifetimes do not have enough time to escape from their dusty birthplace or let the parent molecular clouds to dissipate. As a result, the nebular lines can be subject to a higher degree of reddening than the UV continuum.

Calzetti et al. (1994) found that the nebular emission is more attenuated than the stellar continuum at the same wavelengths for a sample of local UV-bright galaxies. Subsequently, Calzetti et al. (2000) studied a similar sample of local galaxies and argued that the *color-excess* is 2.27 times larger for the nebular emission lines than for the stellar continuum. This relationship was derived under the assumption that the Calzetti curve is applied to the stellar continuum and a Galactic extinction curve is applied to the nebular emission lines. In a separate study, Cid Fernandes et al. (2005) found that for an SDSS sample of ~ 50000 galaxies, $A_{V,nebular} \sim 1.8\ A_{V,stellar}$, both assuming a Cardelli et al. (1989) extinction curve.

There have been several studies of relative attenuation of the stellar continuum and nebular regions in high-redshift galaxies. In most of the high-redshift studies, the Calzetti curve is assumed for both the nebular and stellar regions. Frequently, the Calzetti et al. (2000) relation between the stellar and nebular $E(B-V)$ is used to correct the nebular lines, while this relation was originally derived based on using a Galactic extinction curve for the nebular lines. At present it is unclear what type of attenuation curve should be applied to the nebular regions. These issues are discussed in detail in Steidel et al. (2014).

At $z \sim 2$, Förster Schreiber et al. (2009) selected a sample from various imaging surveys in the optical, near-IR, mid-IR, and sub-millimeter regime, with SED-derived SFRs of $\sim 10-1000\,\mathrm{M_\odot\,yr^{-1}}$ and stellar masses $\gtrsim 10^{10}\,\mathrm{M_\odot}$, assuming a Chabrier IMF. In their study, the predicted Hα luminosities from the best-fit SED models for 62 galaxies were compared with the observed line luminosities measured from integral field spectroscopy. The latter were then corrected for reddening assuming the A_V returned from stellar population modeling of their galaxies. Förster Schreiber et al. (2009) found that assuming a factor of two redder color excess towards the HII regions relative to the stellar continuum yielded the best agreement between the predicted and observed Hα luminosities. Similarly, Wuyts et al. (2011a) investigated 25 star forming galaxies at $z \sim 2$ and compared the Hα SFRs, dust-corrected by the Calzetti attenuation curve, with the SED modeled SFRs. They showed that Hα SFRs are consistent with the SED SFRs, provided that $E(B-V)_{neb} = 2.27E(B-V)_{stellar}$ when assuming the Calzetti curve for both.

Muzzin et al. (2010) presented two galaxies at redshifts $z = 2.122$ and 2.024, and added ten other galaxies at similar redshifts from van Dokkum et al. (2005), Kriek et al. (2007), and Kriek et al. (2009) to compare $\mathrm{A}_{V,nebular}$ derived from the Balmer decrement ($\frac{F(H\alpha)}{F(H\beta)}$) with $\mathrm{A}_{V,stellar}$ derived from the SED models, both assuming the Calzetti curve. The only two galaxies with detected Hβ line measurements showed evidence for higher nebular attenuation, but about half of the non-detections were consistent with equal attenuation for the nebular and stellar regions. In Yoshikawa et al. (2010), Hα attenuation was investigated through several comparisons for a sample of optically-selected star-forming galaxies at $z \sim 2$. Aided with near-infrared spectroscopic observations, Yoshikawa et al. (2010) used the Balmer decrement along with the Calzetti curve to correct the Hα SFR. The dust-corrected SFR was then compared with the Hα SFR corrected by the SED color-excess and also with the SFRs inferred from UV, IR, radio, and X-ray. The comparisons yield contradictory results. Their analysis favored a higher nebular color-excess for galaxies with larger intrinsic SFRs.

In separate studies, Erb et al. (2006c) and Reddy et al. (2010) used a large sample of UV-selected galaxies at $z \sim 2$ and corrected both the Hα and UV SFRs with the color-excess derived from the best-fit SED models and applied the Calzetti attenuation curve. They showed that using different color excesses for the continuum and lines generally resulted in Hα-inferred SFRs that over-predicted those calculated from the dust-corrected UV emission and direct IR measurements.

The apparently conflicting results mentioned above may be reconciled if the relation between the nebular and stellar color-excesses depends on the physical properties of galaxies, such as their SFRs (Yoshikawa et al. 2010) or specific SFRs (Wild et al. 2011). For example, Wild et al. (2011) showed that the ratio of the line optical depth to the continuum optical depth decreases with increasing sSFR and at sSFR$\sim 10^{-9}\,\mathrm{yr}^{-1}$ the line-to-continuum optical depth ratio reaches the Calzetti et al. (2000) ratio assuming the Wild et al. (2011) attenuation curve. Price et al. (2014) investigated the attenuation of the nebular regions at $z \sim 1.5$ using the Balmer decrement from stacked *HST* grism spectra assuming the Calzetti curve, and found no strong trend of $A_{\mathrm{v,neb}}/A_{\mathrm{v,stellar}}$ with SFR or sSFR. In Price et al. (2014) study, at sSFR$\sim 10^{-8.5}\,\mathrm{yr}^{-1}$ the ratio is consistent with 1.

The primary goal of this paper is to understand the relationship between the UV and Hα emission in high-redshift star-forming galaxies, with a large sample that is immune to uncertainties in slit loss corrections that affects the Hα flux estimation (c.f. Erb et al.

2006c; Yoshikawa et al. 2010), the small sample sizes inherent in previous spectroscopic studies of Hα (Kriek et al. 2007; Muzzin et al. 2010), and not subject to the bias of selecting high equivalent width objects from narrow-band selected samples (Garn & Best 2010). We consider in our analysis only spectroscopically-confirmed galaxies, enabling us to estimate the Hα flux from broad-band photometric excess techniques without the additional uncertainties that plague photometric redshifts (Wuyts et al. 2011a).

The impact of nebular lines on the broad-band photometry was known and studied for many years (e.g., Guiderdoni & Rocca-Volmerange 1987; Fioc & Rocca-Volmerange 1997; Zackrisson et al. 2008; de Barros et al. 2014). Using the photometric excesses to determine the line strengths was pioneered by Shim et al. (2011), where they showed that the excess in *Spitzer*/IRAC 3.6 μm relative to the SED model continuum is due to the redshifted Hα emission line for their sample of galaxies at $3.8 < z < 5.0$. Stark et al. (2013) also investigated a sample of galaxies at the same redshift range of Shim et al. (2011) and inferred the Hα emission line strengths by comparing the observed flux in *Spitzer*/IRAC 3.6 μm band and the continuum flux as expected from the SED model. Following that, Schenker et al. (2013) verified the photometric excess technique by applying it to a small sample of 9 galaxies at $3.0 < z < 3.8$; for 8 galaxies the [O III] line fluxes inferred by the same technique as Stark et al. (2013) were within a factor of 2.5 of the spectroscopically measured [O III] fluxes.

An additional advantage of our study is that we include IR data to independently assess the dust-obscured SFR. Comparing Hα, UV, and IR SFRs in a statistical sense allows us to understand how to correct extinction-sensitive measures of SFR for the effects of dust.

The outline of this paper is as follows. In §2.2 we discuss the properties of our sample, the assumptions that have been made to model the stellar populations using the rest-frame UV to near-IR photometry, the *Spitzer*/MIPS photometry and stacking method. A detailed description of how we estimated the Hα line flux is provided in §2.3. The analysis of the MIPS 24 μm data and IR luminosities is described in §2.4. In §2.5 we compare the two different tracers of SFR - Hα and UV - and discuss the dust correction recipe most consistent with our measured values. §2.6 focuses on combining SFR diagnostics (e.g., Hα and UV with IR) to deduce bolometric SFRs. The results are summarized in §2.7. Throughout this paper, a Salpeter (1955) IMF is assumed and a cosmology with $H_0 = 70$ km s^{-1} Mpc^{-1}, $\Omega_\Lambda = 0.7$, and $\Omega_m = 0.3$ is adopted. All magnitudes are given in the AB system (Oke & Gunn 1983).

2.2 Sample

2.2.1 Sample Selection and Optical Photometry

The galaxies used in this study are drawn from a parent sample that is part of an imaging and spectroscopic survey of UV-selected galaxies at z $\sim$ 2-3 (Steidel et al. 2004; Reddy et al. 2012b). The galaxies were selected based on the BX, BM, and Lyman break galaxy rest-UV color criteria (Steidel et al. 2003, 2004; Adelberger et al. 2004), where U_nGR optical data were obtained with the Palomar Large Format Camera (LFC) or Keck Low Resolution Imaging Spectrograph (LRIS; Steidel et al. 2003, 2004). Rest-UV spectroscopic follow-up with Keck/LRIS was conducted for galaxies brighter than R = 25.5 (Steidel et al. 2003, 2004). Near-IR J and K_s imaging was obtained using the Palomar/WIRC and

Magellan/PANIC instruments (Shapley et al. 2005; Reddy et al. 2012b). *H*-band (F160w) data were obtained with the *Hubble Space Telescope* WFC3 camera (Law et al. 2012; Reddy et al. 2012b). All galaxies in the sample have coverage in at least one of the *Spitzer*/IRAC four channels (3.6, 4.5, 5.8, and 8.0 μm; Reddy et al. 2006a, 2012b). The objects are located in the GOODS-North field and 11 additional fields that were primarily selected to have one or more relatively bright background QSOs for studying the interface between the intergalactic medium (IGM) and galaxies at z $\sim$ 2-3 (Steidel et al. 2004; Steidel et al. 2010).

Out of the final sample of 2283 objects with spectroscopically confirmed redshifts, a subset of galaxies is selected based on the following criteria: (1) the galaxy must be covered by the *K*-band imaging, (2) it must have a redshift in the range 2.08 $\leq$ z $\leq$ 2.51 so that the Hα line falls into the K_s band, and (3) it must be detected in at least two of the IRAC channels or one of the IRAC channels and either J or F160w bands. The third condition ensures a more robust estimate of the stellar mass and the continuum level at 6564 Å . Furthermore, AGNs (making up $\approx$ 9% of the parent sample) were identified by either strong UV emission lines (e.g., Lyα, CIV) or by a power law SED through the IRAC bands. These AGNs are removed from our sample. Eventually, 262 galaxies remain that satisfy the aforementioned criteria.

2.2.2 Stellar Population Modeling

For each galaxy in our sample, the best-fit stellar population model is found by using the rest-frame UV through near-IR broad-band photometry. As mentioned above, all the galaxies in our sample have spectroscopically-confirmed redshifts, thus removing a key degeneracy in the modeling of the stellar populations. In addition, for a better estimation of stellar mass and age, all galaxies in our sample have at least two detections long-ward of the 4000 Å break - excluding K_s-band.

C. Charlot & G. Bruzual (2007) models with a Salpeter (1955) IMF and solar metallicities are used for the fitting. For each individual galaxy, different star-formation histories are assumed, including constant, exponentially declining, and exponentially rising with characteristic timescales of τ = 10, 20, 50, 100, 200, 500, 1000, 2000, 5000 Myr for exponentially declining and τ = 100, 200, 500, 1000, 2000, 5000 Myr for exponentially rising histories. Ages are allowed to vary between 50 Myr and the age of the universe at the redshift of each galaxy. The > 50 Myr limit corresponds to the typical dynamical timescale of star-forming galaxies at $z \sim 2$ as inferred from velocity dispersion and size measurements of these galaxies (Reddy et al. 2012b). For interstellar dust obscuration, the Calzetti et al. (2000) attenuation curve is used, allowing $E(B-V)$ to vary between 0.0 and 0.6. The χ^2 values have been determined for each set of observed broad-band and model magnitudes. The best-fit model is determined through χ^2 minimization. There is generally no significant difference between the best-fit χ^2 values of the six different population models (constant, exponentially rising, and exponentially declining star-formation histories, for each considering all ages and ages greater than 50 Myr). As previous studies have shown, the assumption of declining star-formation histories at these redshifts results in systematically lower SED-inferred SFRs compared to the observed IR+UV SFRs (Wuyts et al. 2011a; Reddy et al. 2012b). Furthermore, Reddy et al. (2012b) showed that assuming a constant star-formation history for $z \sim 2$ galaxies predicts specific SFRs (SFR/M_*) at higher redshifts ($z \sim 2.6$) that are substantially larger than the observed values. Given these, we adopt the models that assume exponentially rising star-formation histories with ages greater than 50 Myr.

The SED models used to fit the observed magnitudes do not include nebular emission lines. For example, the Hα line can significantly affect the photometry and we use its contribution to the K-band to estimate the Hα line flux. The [O III] emission line is the other strong line which falls into the F160w filter given the redshift range of our galaxies. Only 20% of the galaxies have F160w observations, for which we did not correct the broadband photometry for the contamination. The SED-inferred SFR of these galaxies is consistent with the SFR(UV) estimates within the uncertainties. At this redshift, J band is contaminated by the [O II] emission line, but this line is generally weaker than the Hα line and its effect on the SED inferred SFRs is negligible compared to the uncertainties.[1]

2.2.3 MIPS data

To further investigate the bolometric properties of our sample, we use *Spitzer*/MIPS 24 μm wherever available. Out of 12 fields, GOODS-North (Dickinson et al. 2003), and four other fields (Q1549, Q1623, Q1700, and Q2343; Reddy & Steidel 2009) have MIPS 24 μm coverage to a typical 3 σ depth of 10-15 μJy.

Photometry on 24 μm images is performed by using point-spread function (PSF) fitting with priors determined by the locations of the objects in the higher resolution IRAC images (IRAC data exist in all fields). A 40×40 pixel region centered on each target is extracted with pixel size of 1.″2. PSFs are then fitted simultaneously to all known sources

[1] For galaxies with similar SFRs at $z \sim 2$, the typical [O II] line flux is $\sim 6 \times 10^{-17}$ erg s^{-1} cm^{-2} (Kriek et al. 2015). The ratio of the [O II] flux to the typical J-band flux errors in our observations is only ~ 0.07.

in the sub-image and one random background position. This procedure is repeated many times to obtain sufficient statistics for proper background estimation based on the random background flux measurements. The other source of uncertainty is Poisson noise, which for objects in our sample is negligible compared to the background dispersion. We remove objects whose photometry may be compromised due to blending with nearby sources, using the criteria specified in Reddy et al. (2010). This results in 115 galaxies with secure PSF fits.

Out of 115 objects with MIPS data, 47 are detected with S/N $\leq$ 3. Undetected objects, those with S/N $<$ 3, are considered using either survival analyses or through stacking of the 24 μm data.

Stacking Method

Throughout the paper, we employ a stacking method to determine the median 24 μm fluxes of objects that are individually detected and undetected, following the procedures described in Reddy et al. (2010, 2012a). We performed aperture photometry on the stacked images, and applied an aperture correction based on the 24 μm PSF. The average background level and noise were determined by placing many apertures of the same size used for the stacked signal at random positions in the stacked image and measuring the average flux level and dispersion in flux of these "background" apertures. Furthermore, we used bootstrap resampling simulations to estimate the dispersion in the fluxes of objects contributing to each stack. This was accomplished by creating 100 samples of random images in each bin and measuring the standard deviation of the median stacked fluxes. The intrinsic dispersion in the stacked flux is larger than the background error by a factor of ~ 2.

2.3 Hα and UV Luminosity

2.3.1 Hα Fluxes and Equivalent Widths

Using the procedure discussed in §2.2.2, we fit all the photometry, excluding K_s-band, in order to determine the continuum level at 6564 Å. The continuum magnitude is calculated by multiplying the best-fit SED model by the K_s filter transmission curve. The difference between the observed K_s-band magnitude and the continuum magnitude is used to extract the Hα line flux as follows. The observed K_s magnitude is considered as the sum of the continuum and the Hα fluxes, while the SED-inferred K_s magnitude represents only the continuum flux. Assuming a Gaussian form for the redshifted Hα line, the change between these fluxes will yield the Hα flux (Figure 2.1):

$$\frac{\int \frac{d\nu}{\nu}\ f_{H\alpha}(\nu)\ T_K(\nu)}{\int \frac{d\nu}{\nu}\ T_K(\nu)} = 10^{\frac{(m_{obs}+48.6)}{-2.5}} - 10^{\frac{(m_{SED}+48.6)}{-2.5}}. \tag{2.1}$$

Here, $f_{H\alpha}(\nu)$ is the flux density of the Hα line in units of erg s^{-1} cm^{-2} Hz^{-1}, $T_K(\nu)$ is the K_s filter transmission curve, and m_{obs} and m_{SED} are the observed and the continuum magnitudes, respectively. The Hα flux is corrected for contamination from the [NII] line based on the mass-dependent [NII]-to-Hα flux ratios of Erb et al. (2006a). The stellar masses are determined from the SED models and the corresponding [NII] line contamination, as

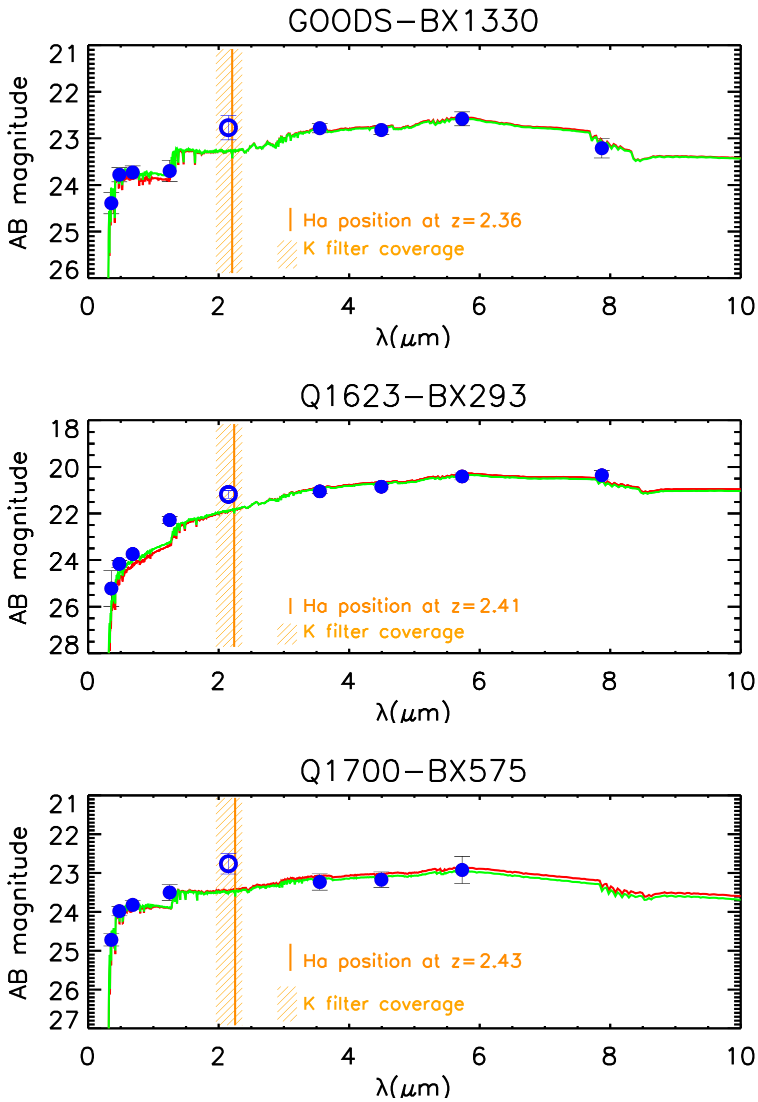

Figure 2.1 Best-fit SED models for three objects in our sample: BX1330 in GOODS-North (top), BX293 in Q1623 (middle), and BX575 in Q1700 (bottom). All the models assume an exponentially rising star-formation history, with a lower limit in age of 50 Myr. The K_s band data are shown with an open circle in each plot. The green and red lines show the best-fit models when we exclude and include, respectively, the K-band photometry in the fitting. The two fits are similar because the K_s photometry is down-weighted in the fitting due to larger measurement errors. The vertical orange line shows the position of the redshifted Hα line. The dashed area represents the K_s filter coverage. At redshifts of $z \sim 2.08 - 2.50$, the K_s filter is affected by the Hα emission line, and the difference between the K_s-band flux and the underlying stellar population model can be used to estimate the line flux.

listed in Table 2.1, is used to correct the Hα flux. The SFRs are then calculated using the Kennicutt (1998) relation to convert the Hα line luminosity to an SFR.

There are three main sources of uncertainty in the derived Hα fluxes. The largest uncertainty is the photometric error. The typical error in the observed K_s-band magnitude is $\simeq 0.27$. The second source of uncertainty is the [NII] correction. The uncertainty on the Erb et al. (2006a) [NII]-to-Hα line ratios (see Table 2.1) is added in quadrature to the photometric error. The third source of uncertainty is the error associated with the continuum flux. In order to account for this uncertainty, we estimated the continuum flux at 6564Å from the best-fit model assuming six different star-formation histories: exponentially rising, exponentially declining, and constant, for each considering all ages and ages greater than 50 Myr. For 94% of the galaxies the difference in the mean of the continuum fluxes assuming different star-formation histories to those assuming a rising star-formation history with ages ≥ 50 Myr is less than 0.1 magnitude. The average error in the estimated continuum magnitude is ~ 0.05 mag, which is negligible compared to the observed K_s-band magnitude errors. Combining the three sources of uncertainty discussed above yields a typical relative error in Hα flux of ~ 0.29.

The equivalent width of the Hα line is estimated by dividing the Hα flux derived from Equation 2.1 by the continuum flux density at the wavelength of the Hα line:

$$(1+z)EW_0 = \frac{F_{H\alpha}}{f_\lambda^{cont}}. \tag{2.2}$$

Table 2.1. Hα Flux Corrections for [NII] Contamination[a]

Mass Range (10^{10} $M_{\odot}$)[b]	N2[c]
< 0.88	< -1.22
0.88 – 2.00	$-1.00^{+0.07}_{-0.09}$
2.00 – 3.69	$-0.85^{+0.05}_{-0.06}$
3.69 – 6.03	$-0.78^{+0.05}_{-0.05}$
6.03 – 8.82	$-0.66^{+0.03}_{-0.04}$
> 8.82	$-0.56^{+0.02}_{-0.02}$

[a]Based on Erb et al. (2006a)

[b]Assuming a Salpeter (1955) IMF

[c]$N2 \equiv \log(\frac{F([\mathrm{NII}])}{F(\mathrm{H}\alpha)})$

The f_{λ}^{cont} is the continuum flux density in units of erg s^{-1} cm^{-2} $Å^{-1}$ that is estimated through the best-fit SED model, $F_{H\alpha}$ is the Hα line flux in erg s^{-1} cm^{-2}, z is the redshift of the galaxy, and EW_0 is the rest-frame equivalent width in Å.

We define whether a galaxy has a "detected" Hα line according to the following. Galaxies whose K_s-band photometry exceeds the continuum level by more than the K_s-band magnitude error are referred to as "Hα detections". Galaxies where the K_s-band photometry is consistent with the continuum level to within 1 σ are referred to as "Hα non-detections", and an upper limit of 1σ above the measured K photometry is used for these objects. Out of 262 galaxies in our sample, 149 are detections and 94 are non-detections. There are 19 objects with K_s magnitudes fainter than the continuum by more than 1σ. We removed these galaxies from our discussion due to their K_s photometry being inconsistent with the photometry from adjacent bands.

As discussed in §2.1, our method of computing Hα fluxes and EWs has the advantage of being immune to slit-loss corrections. Our sample covers a wide range of Hα

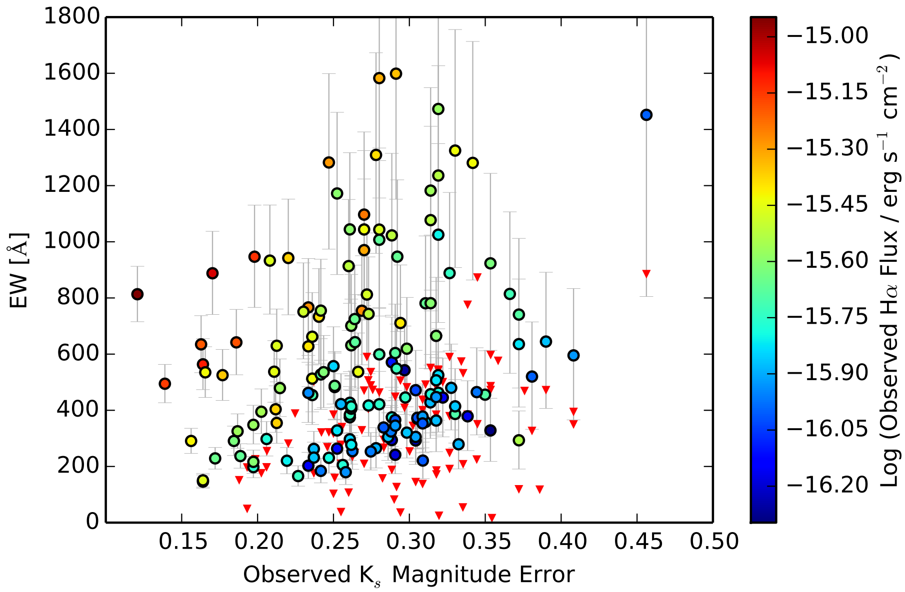

Figure 2.2 Estimated Hα rest-frame equivalent widths as a function of the error of the observed K_s-band magnitude. The circles are detected galaxies and are color coded based on their observed Hα fluxes (uncorrected for extinction). The red triangles show 1σ upper limits. Detecting the Hα emission requires that the observed K_s magnitude lies more that 1σ above the underlying continuum, where 1σ is defined by the K_s magnitude error. The K_s magnitude includes the light both from the Hα emission line and the brightness of the continuum at 6564 Å. There is a tight correlation between the continuum brightness and the K_s magnitude error; the fainter continuum results in larger uncertainty in the observed magnitude. As a result, there are more undetected objects with large K_s-band errors. On the other hand, the brightest Hα objects have bright continuum and small K_s-band uncertainties. The deficiency of objects in the upper-left corner is mainly because very bright Hα objects that also have bright continuum are rare.

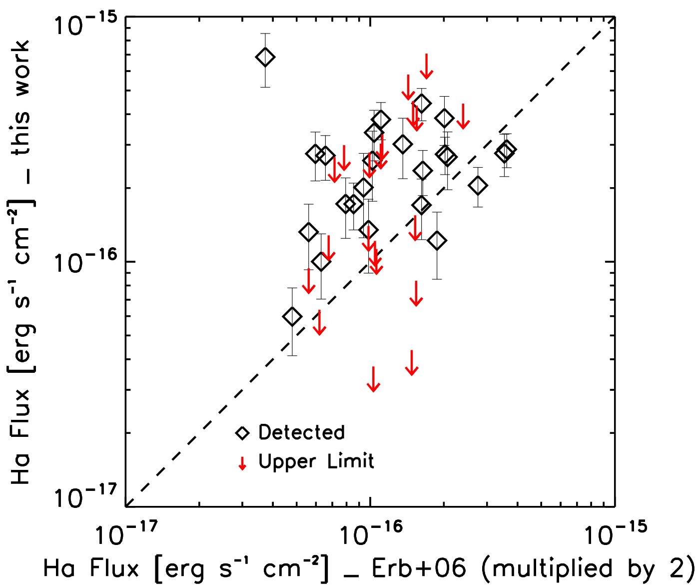

Figure 2.3 A comparison of observed Hα fluxes of the objects in common between our sample and that of Erb et al. (2006c). The diamonds are the detected objects and downward arrows show 1 σ upper limits, as discussed in the text. The fluxes are measured based on the difference between the observed and the continuum K_s magnitudes predicted from the best-fit model. The error bars are dominated by the uncertainty in the observed K_s photometry. The Erb et al. (2006c) spectroscopic fluxes are multiplied by a factor of 2 to account for slit losses. The dashed line denotes the one-to-one relationship.

fluxes and EWs. Figure 2.2 shows the distribution of Hα EWs and fluxes as a function of the K_s magnitude 1σ uncertainty. The detection of Hα with the method adopted here depends on both the Hα line flux and the brightness of the continuum at 6564 Å. As we have defined detections to be those objects where the K_s magnitude exceeds the continuum level by more than 1σ , the number of undetected objects increases for objects that are fainter in the continuum (Figure 2.2).

The Hα observed fluxes of 44 objects in common with the Erb et al. (2006c) spectroscopic sample are compared in Figure 2.3. The Erb et al. (2006c) spectroscopic fluxes are multiplied by a factor of two to account for slit losses and the aperture used to extract the spectra (Erb et al. 2006c; Reddy et al. 2010). The slit loss correction factor applied to the spectroscopic fluxes depends on various factors such as the accuracy of the astrometry, the size of the object convolved with the seeing at the time of observation in comparison with the size of the slit, and the accuracy of the mask alignment during the observation. As noted in Erb et al. (2006c), the factor of two slit-loss correction is an average estimate and the slit losses will of course vary from object to object, likely accounting for some of the scatter in Figure 2.3. On the other hand, while broadband photometry has its advantages, our K_s-band measurements suffer from a larger measurement (random) uncertainty relative to the other methods given the depth of our ground-based images. Although most of the detected Hα fluxes in this study (the black symbols in Figure 2.3) are higher that the spectroscopic fluxes, about half of the sample is estimated as upper limits (the red arrows). Considering both the detections and non-detections, the broad-band estimated fluxes are generally consistent with the spectroscopic fluxes. To quantify the degree of the correlation we conduct a generalized Kendall's tau (τ) statistic. The generalized Kendall's τ rank correlation coefficient is a non-parametric test that permits non-detections in both variables (here, our estimated Hα fluxes). Kendall's τ correlation coefficient for our flux estimation with the Erb et al. (2006c) measurements, excluding the one outlier object, is $\tau = 0.17$, with significance of p-value = 0.11.

2.3.2 UV Luminosities and SFRs

UV luminosities are calculated using the fluxes of the best-fit SED models at 1700 Å. The Kennicutt (1998) relation to convert the UV luminosity (over the wavelength range 1500-2800 Å) to SFR applies only to galaxies where star formation proceeds for $\gtrsim$ 100 Myr. However, there are galaxies in our sample with inferred ages between 50 and 100 Myr. For these younger galaxies, we used an age- and star-formation-history-dependent relation in the conversion of the UV luminosity to SFR, as discussed in Reddy et al. (2012b). The age-dependent conversion resulted in UV SFRs that are at most 14% larger than the Kennicutt (1998) SFRs for young galaxies. Throughout this analysis, we also use SFRs inferred from the best-fit SED models. As expected, within the uncertainties, the SED SFRs are highly correlated with dust corrected UV SFRs.

2.4 The IR Luminosity and Bolometric Properties

To estimate the bolometric luminosities of galaxies in our sample, we infer the infrared luminosity (integrated between 8-1000 μm) as discussed below, and add this to the unobscured UV luminosity (i.e., observed UV luminosity; §2.3.2), as in Reddy et al. (2010).

Infrared luminosities, $L_{\rm IR}$, are estimated by using the *Spitzer*/MIPS 24 μm observations. The 24 μm band is sensitive to the rest-frame 7.7 μm PAH emission, which correlates with $L_{\rm IR}$ (e.g., Chary & Elbaz 2001; Dale & Helou 2002; Elbaz et al. 2011). To convert observed 24 μm magnitudes to total IR luminosity (L_{IR}), we used several dust SED templates, including those of Chary & Elbaz (2001), Dale & Helou (2002), and Rieke et al. (2009). Luminosities determined from the rest-frame 8 μm flux density alone, regardless of the dust template used, tend to over predict L(IR), particularly for LIRGs (e.g., Reddy et al. 2012a) and ULIRGs (e.g., Nordon et al. 2010; Magnelli et al. 2011). In order to account for the luminosity-dependent overestimation of the derived L(IR), we use a correction equation described in Reddy et al. (2012a). The correction is calculated by comparing the L(IR) computed from 24, 100, 160 μm, and 1.4 GHz fluxes, and the L(IR) determined solely from 24 μm data for a similarly-selected sample of galaxies:

$$\log L_{\rm IR}(\text{all data}) = 0.537 \times \log L_{\rm IR}(24\mu\text{m}) + 5.136. \tag{2.3}$$

All luminosities are in $L_\odot$.

Equation 2.3 is based on the Chary & Elbaz (2001) models. There is a factor of ~ 2 variation in L(IR) derived from 24μm data using Dale & Helou (2002) and Rieke et al. (2009) dust templates (e.g., see Reddy et al. 2012a). However, once corrected using the appropriate equations similar to Equation 2.3, all the templates result in L(IR) estimates that are consistent with each other and with the L(IR) computed from 24, 100, 160 μm, and 1.4 GHz fluxes, within the uncertainties of the measured IR luminosity as explained in §2.2.3 (see also Reddy et al. 2012a). In the subsequent analysis, we use infrared luminosities inferred from the Chary & Elbaz (2001) templates.

The IR luminosity is converted to IR (dust-obscured) SFRs using the Kennicutt (1998) relation. The sum of IR- and UV-inferred SFRs are then used to estimate the bolometric SFRs.

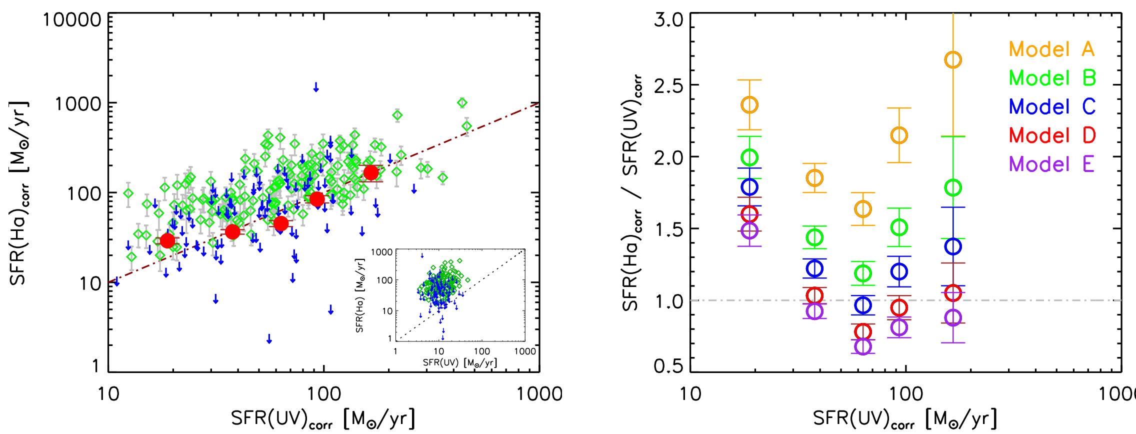

Figure 2.4 (*Left:*) Comparison of SFR(Hα) and SFR(UV), both corrected for dust assuming the Calzetti attenuation curve and assuming that the same color excess applies for the stellar and nebular regions. The uncorrected values are shown in the inset panel. Green diamonds denote "detected" objects, those whose K_s-band magnitudes are more than $1\,\sigma$ brighter than the continuum. Blue arrows show the remaining "undetected" objects. Red filled circles are the results of stacked SEDs in bins of dust-corrected SFR(UV), including both the detected and undetected objects. Undetected objects bring the stacks lower than the average of the individually detected green diamonds. The dashed lines indicate the one-to-one relationships. (*Right:*) Ratio of SFR(Hα)$_{corrected}$ to SFR(UV)$_{corrected}$ in bins of SFR(UV)$_{corrected}$. The colors denote different recipes for the nebular dust correction. Using the same color excess for nebular extinction together with the Calzetti curve (model D; see text) gives the best agreement between Hα and UV SFRs, while assuming higher nebular attenuation (i.e., $E(B-V)_{nebular} = 2.27\,E(B-V)_{stellar}$) with the Calzetti curve results in SFR(Hα) that is significantly larger than SFR(UV) (model A). The details of each model are summarized in Table 2.2.

2.5 Dust Attenuation of the Nebular Regions and Stellar Continuum

SFRs inferred from the UV luminosity and the Hα fluxes are shown in the left panel of Figure 2.4. Without dust corrections, the UV and Hα SFRs have a large discrepancy due to the smaller dust absorption cross-section at 6564 Å relative to that at 1700 Å (see the inset panel in Figure 2.4). The main left panel of Figure 2.4 shows Hα and UV SFRs, both corrected for dust attenuation based on the Calzetti attenuation curve and assuming that the same color-excess, $E(B-V)$, as derived from the best-fit SED model, applies to the stellar continuum and the nebular regions. To better quantify the mean trend, measurements have also been performed in bins of UV dust-corrected SFR (filled circles in Figure 2.4). The bins are $\Delta\log(\text{SFR}_{UV,corrected}) = 0.3$ dex wide. For all the galaxies in each bin, regardless of their redshift, we calculate the median flux densities in the observed filters. With the new set of median fluxes, the best-fit stellar population model is determined through χ^2 minimization for the mean redshift of the galaxies in each bin. The Hα and UV luminosities are then derived from the stacked SED in the same way as for individual galaxies (see § 2.3). Reported errors are calculated based on the $1\,\sigma$ standard error of the mean of the K_s magnitudes contributing to each bin.

The appropriate dust corrections to apply to the nebular emission lines is still a subject of debate, as discussed in Section 2.1. The attenuation of the nebular lines and the UV stellar continuum are not completely decoupled as both arise from dust around massive stars. On the other hand, whether the color-excess is the same for the nebular and

Table 2.2 Dust Corrected Hα SFRs Using Different Attenuation Recipes, in Bins of SFR(UV)$_{corr}$

SFR(UV)$^{a}_{corr}$	N^{b}	SFR(Hα)$^{c}_{corr}$				
		Calzetti Diff $E(B-V)^{d}$ (Model A)	Galactic Diff $E(B-V)^{e}$ (Model B)	SMC Diff $E(B-V)^{f}$ (Model C)	Calzetti Eq $E(B-V)^{g}$ (Model D)	Galactic Eq $E(B-V)^{h}$ (Model E)
18 ± 3	26	44 ± 3	38 ± 3	34 ± 2	30 ± 2	28 ± 2
32 ± 6	63	70 ± 4	54 ± 3	46 ± 3	38 ± 2	35 ± 2
65 ± 12	83	103 ± 7	75 ± 5	61 ± 4	49 ± 3	43 ± 3
120 ± 22	56	200 ± 18	140 ± 12	112 ± 10	88 ± 8	76 ± 7
258 ± 94	15	443 ± 88	295 ± 59	228 ± 45	174 ± 35	146 ± 29

[a] The mean and standard deviation of the corrected SFR(UV) in each bin, in units of $M_{\odot}\,yr^{-1}$.
[b] Number of objects in each bin.
[c] The SFR(Hα)$_{corr}$ is derived based on the stacked SEDs in bins of dust-corrected SFR(UV), in units of $M_{\odot}\,yr^{-1}$. The errors are $1\,\sigma$ standard error of the mean of the K_s magnitudes contributing to each bin, which is converted to the error in SFR.
[d] $A_{H\alpha} = 2.27\ \kappa_{\rm Calz}(H\alpha)\ E(B-V)_{\rm stellar}$; $A_{H\alpha}$ is the total nebular extinction at 6564 Å and $\kappa_{\rm Calz}(H\alpha)$ is the Calzetti reddening at 6564 Å.
[e] $A_{H\alpha} = 2.27\ \kappa_{\rm Gal}(H\alpha)\ E(B-V)_{\rm stellar}$; $\kappa_{\rm Gal}(H\alpha)$ is the Cardelli Galactic reddening at 6564 Å.
[f] $A_{H\alpha} = 2.27\ \kappa_{\rm SMC}(H\alpha)\ E(B-V)_{\rm stellar}$; $\kappa_{\rm SMC}(H\alpha)$ is an SMC reddening at 6564 Å.
[g] $A_{H\alpha} = \ \kappa_{\rm Calz}(H\alpha)\ E(B-V)_{\rm stellar}$; $\kappa_{\rm Calz}(H\alpha)$ is the Calzetti reddening at 6564 Å.
[h] $A_{H\alpha} = \ \kappa_{\rm Gal}(H\alpha)\ E(B-V)_{\rm stellar}$; $\kappa_{\rm Gal}(H\alpha)$ is the Cardelli Galactic reddening at 6564 Å.

stellar regions (e.g., Erb et al. 2006c; Reddy et al. 2010) or not (e.g., Calzetti et al. 2000; Förster Schreiber et al. 2009; Garn & Best 2010) in high-redshift galaxies has yet to be fully investigated.

Calzetti et al. (2000) found that $E(B-V)_{\rm stel} = 0.44 \times E(B-V)_{\rm neb}$ for a sample of local star-forming galaxies. In the absence of direct measurements of the nebular color-excess (e.g., via the Balmer decrement), this relationship can in principle be used to estimate the nebular color excess and apply a dust correction to the Hα line; e.g.,

$$
\begin{aligned}
\mathrm{A}_{H\alpha} &= \kappa_{\mathrm{Gal}}(H\alpha)\ E(B-V)_{\mathrm{nebular}} \\
&= 2.27\ \kappa_{\mathrm{Gal}}(H\alpha)\ E(B-V)_{\mathrm{stellar}} \\
&= 2.27 \times 2.52\ E(B-V)_{\mathrm{stellar}} \\
&= 5.72\ E(B-V)_{\mathrm{stellar}},
\end{aligned} \tag{2.4}
$$

where κ_{Gal} is the Cardelli et al. (1989) Galactic extinction curve, assuming that the nebular regions in the high-redshift galaxies abide by such a dust curve. $A_{H\alpha}$ is the absolute extinction of Hα emission line, and $E(B-V)_{\mathrm{stellar}}$ is the SED-inferred stellar color excess.

We investigate several of the more commonly used dust-correction recipes, as described below. The Hα SFRs are corrected using five different methods:

A. the Calzetti attenuation curve for both gas and stars, but 2.27× larger color-excess for the nebular lines than the stellar continuum (as we call it "different $E(B-V)$"),

B. the Calzetti attenuation curve for the stellar continuum, and the Cardelli et al. (1989) Galactic curve for the nebular lines assuming 2.27× larger color-excess,

C. the Calzetti attenuation curve for the stellar continuum, and an SMC extinction curve (Gordon et al. 2003) for the nebular lines assuming 2.27× larger color-excess,

D. the Calzetti attenuation curve for both gas and stars, and the same color-excess (as we call it "equal $E(B-V)$"), and

E. the Calzetti attenuation curve for the stellar continuum, an SMC extinction curve (Gordon et al. 2003) for the nebular lines assuming the same color-excess.

We choose to compare these different dust-correction scenarios for the stacked values instead of the individual galaxies as the former represent an average over many points including both detected and undetected quantities, each of which may be relatively uncertain. The results are plotted in the right panel of Figure 2.4 and are reported in Table 2.2.

To summarize, these are the values that are used to correct the observed Hα SFRs in each model according to Equation 2.4:

$$\begin{aligned}
\mathrm{A}_{H\alpha}^{(A)} &= 2.27\ \kappa_{\mathrm{Calz}}(H\alpha)\ E(B-V) = 7.56\ E(B-V), \\
\mathrm{A}_{H\alpha}^{(B)} &= 2.27\ \kappa_{\mathrm{Gal}}(H\alpha)\ E(B-V) = 5.72\ E(B-V), \\
\mathrm{A}_{H\alpha}^{(C)} &= 2.27\ \kappa_{\mathrm{SMC}}(H\alpha)\ E(B-V) = 4.54\ E(B-V), \\
\mathrm{A}_{H\alpha}^{(D)} &= \kappa_{\mathrm{Calz}}(H\alpha)\ E(B-V) = 3.33\ E(B-V), \\
\mathrm{A}_{H\alpha}^{(E)} &= \kappa_{\mathrm{Gal}}(H\alpha)\ E(B-V) = 2.52\ E(B-V).
\end{aligned} \tag{2.5}$$

In these equations, $E(B-V)$ is the SED-inferred color-excess observed for the stellar continuum and $\mathrm{A}_{H\alpha}$ is the total nebular extinction at 6564 Å.

In model (A) with a larger color excess for the nebular regions with the Calzetti curve, Hα-inferred SFRs are significantly larger than UV SFRs. Taking the average of the SFR(Hα) (model A) to the corrected SFR(UV) in the five bins of SFR(UV) indicated in Tables 2.2 yields a value of 2.1 ± 0.2 which shows a $\sim 5\sigma$ discrepancy from unity.

Using either model (C) or (D), results in $\mathrm{SFR}_{corrected}(H\alpha)$ that are in good agreement with $\mathrm{SFR}_{corrected}(UV)$. Model (B) reproduce systematically higher SFRs but is still consistent with the range of $\mathrm{SFR}_{corrected}(UV)$ in higher bins, and model (E) estimations are lower than expected.

Based on the data provided in Table 2.2 and the right panel of Figure 2.4, model (D) provides the best agreement between SFRs among the five models. The average of the SFR(Hα)-to-SFR(UV) ratios in the five SFR(UV) bins of this model shows less than 1σ discrepancy from unity. This suggests that *on average* the best recipe to correct the Hα-inferred quantities of star-forming galaxies at $z \sim 2$ is to use $E(B-V)_{\rm nebular} = E(B-V)_{\rm stellar}$ with the Calzetti reddening curve.

2.6 Bolometric Star-Formation Rates

As discussed above, a primary disadvantage of using Hα and UV SFR diagnostics is that we must account for dust extinction, though this is less of a problem for Hα as it is for the UV. The attenuation curves (e.g., the Calzetti et al. 2000 curve) that are used to correct the luminosities encode information regarding the dust grain size distribution and the geometrical distribution of dust with respect to stars (e.g., whether the dust is clumpy or uniform, a homogeneous mixture or a foreground screen, etc.). On the other hand, the IR luminosity is a direct tracer of dust and thus provides an independent and more robust diagnostic of dust attenuation.[2] Adding the IR luminosity, which accounts for the obscured

[2]The dust heated by the visible light from older stellar populations (i.e., the cold component) also contributes to the IR luminosity. However, in case of the star-forming galaxies the contribution of the UV radiation of massive stars (the warm component) is expected to dominate the total IR luminosity (Kennicutt 1998).

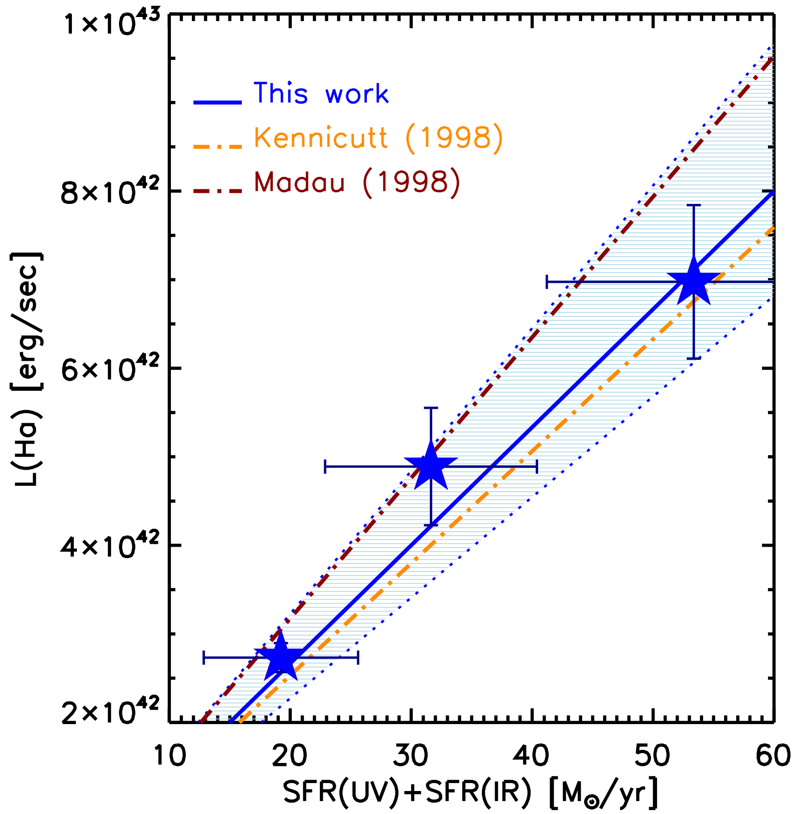

Figure 2.5 The observed Hα line luminosity as a function of bolometric SFR. The stars indicate the average values in bins of SFR(SED). Galaxies with SFR(SED) < 32 $M_\odot\,yr^{-1}$ are in the first bin; those with SFR(SED) between 32 $M_\odot\,yr^{-1}$ and 100 $M_\odot\,yr^{-1}$ are in the middle bin; and last bin consists of galaxies with SFR(SED) > 100 $M_\odot\,yr^{-1}$. The error in SFR(UV)+SFR(IR) is determined by the dispersion error in IR luminosity of the objects contributing to each stack. L(IR) dispersion error is estimated through bootstrap resampling simulations. The solid blue line is the best linear fit. The slope of this fit gives us the conversion factor for $L(H\alpha)_{obs}$-to-SFR_{total} relation. The shaded area is the 68% confidence interval of our estimated slope. The orange and dark-red dashed lines show the conversion factors of Kennicutt (1998) and Madau et al. (1998), respectively.

star formation, to the unobscured (UV and Hα) tracers of SFR can give a more reliable estimate of the bolometric SFR.

2.6.1 The Relationship between Observed Hα Luminosity and Total SFR

To convert the observed Hα luminosity to total SFR, the most commonly used calibration is that of Kennicutt (1998), which is computed using an evolutionary synthesis model, assuming Case B recombination with T_e=10,000 K. In the absence of Balmer decrement measurements, the observed Hα SFR must be corrected for dust with some assumption of the attenuation curve and color-excess of the ionized gas. In this section, we examine the $L_{H\alpha}$-to-SFR conversion by relying only on the observed data, without making any assumptions about the dust correction or electron temperature of the ionized gas. With this conversion, one can use the Hα observed luminosity as a proxy for total SFR without assuming a dust attenuation curve and its associated uncertainties. The conversion applies to stellar populations with constant star formation at least over 100 Myr. For bursty star formation histories over timescales shorter than 100 Myr, the Hα and UV+IR luminosities diverge as the Hα luminosity traces more instantaneous star formation over timescales of $\sim$ 10 Myr, while IR+UV is not sensitive to the change of star formation on timescales $\lesssim$ 100 Myr. Here, we are deriving the conversion factor based on the stacked data that represents the "average" quantities and thus should be used with caution for galaxies that may be undergoing bursty star formation.

Bolometric SFR (SFR(IR)+SFR(UV)) is plotted as a function of the Hα luminosity in Figure 2.5. As both the Hα and IR measurements have non-detections, we decided to bin the data with respect to the SED-inferred SFR. We chose the bins so that in each bin the SFR(SED) is consistent with the stacked SFR(IR)+SFR(UV) within the uncertainties, because ultimately we are using SFR(IR)+SFR(UV) to calculate the Hα luminosity-to-SFR conversion factor. MIPS data are stacked in each bin and the total IR luminosity is extracted in the same way as for individual galaxies. The UV and Hα luminosities are derived from the stacked SEDs.

A weighted least squares regression method is used to find the slope of the relation:

$$\mathrm{SFR}_{bol}\,(M_{\odot}\,\mathrm{yr}^{-1}) = (7.5 \pm 1.3) \times 10^{-42}\,\mathrm{L}_{obs}(H\alpha)\,(\mathrm{erg\,s}^{-1}). \tag{2.6}$$

This relation can be used to convert the observed Hα luminosity in units of erg s^{-1} to the bolometric SFR. The factor given in Kennicutt (1998) and Kennicutt et al. (1994), to convert observed/intrinsic luminosity to observed/intrinsic SFR, is 7.9 $\times 10^{-42}$ $\mathrm{M}_{\odot}\,\mathrm{yr}^{-1}\,\mathrm{erg}^{-1}\,\mathrm{s}$. Madau et al. (1998) reported a conversion factor of 6.3 $\times 10^{-42}\,\mathrm{M}_{\odot}\,\mathrm{yr}^{-1}$ erg^{-1} s. These factors are computed using evolutionary synthesis models and are subject to those models' uncertainties as well as the initial assumptions that went into these models, such as IMF, star-formation history, and the stellar evolution and atmosphere models. For the same galaxy type and assumed IMF, Kennicutt (1998) reports $\sim 30\%$ variation among different calibrations, which mainly reflects the sensitivity to the SED modeling stellar evolution input data. In our analysis, converting L(IR) and L(UV) to SFR still rely on the model assumptions, but previous studies have shown that in the absence of the Balmer decrement measurements, the sum of SFR(IR) and SFR(UV) is the most reliable estimate of total SFR (Hirashita et al. 2003; Reddy et al. 2012b). Our derived slope for a Salpeter IMF is consistent with Kennicutt (1998) and Madau et al. (1998) within the errors.

Excluding galaxies with ages < 100 Myr (see § 2.6.2) results in a best-fit slope of $7.8 \times 10^{-42}\,M_{\odot}\,yr^{-1}\,erg^{-1}\,s$ that is consistent with the slope found above.

2.6.2 Validity of the Calzetti Dust Attenuation for Young Galaxies

Figure 2.6 shows the bolometric SFR vs. median SFR inferred from the best-fit SED model, in bins of SFR(SED). Both quantities are representative of the total SFR of the galaxies, the only difference being the method by which dust is accounted for. The bolometric SFR, as mentioned before, is the sum of SFR(IR) and SFR(UV), and is independent of any dust correction. On the other hand, for SFR(SED), the effect of dust is considered by using the Calzetti attenuation curve in the SED fitting procedure. We would like to determine whether for all types of galaxies at $z \sim 2$ the bolometric SFRs agree with SED SFRs that are corrected by the Calzetti attenuation curve. We stack the MIPS data of individual detected and undetected galaxies in three bins of SFR(SED) as described in §2.2.3. The three bins in log(SFR(SED)) are < 1.5, 1.5 to 2, and > 2, with respectively 44, 56, and 15 galaxies in each bin. SFR(SED) and SFR(UV) are the median SFRs of the individual galaxies in each bin. The results of stacking is shown with open blue circles in Figure 2.6. In the last two bins, the SED SFR is overestimated compared to the bolometric SFR. Stacking the MIPS images for only objects that are inferred to be older than 100 Myr produces different results. The number of objects in bins with galaxies older than 100 Myr reduces to 43, 50, and 8, respectively from the lowest SFR(SED) bin to the highest.

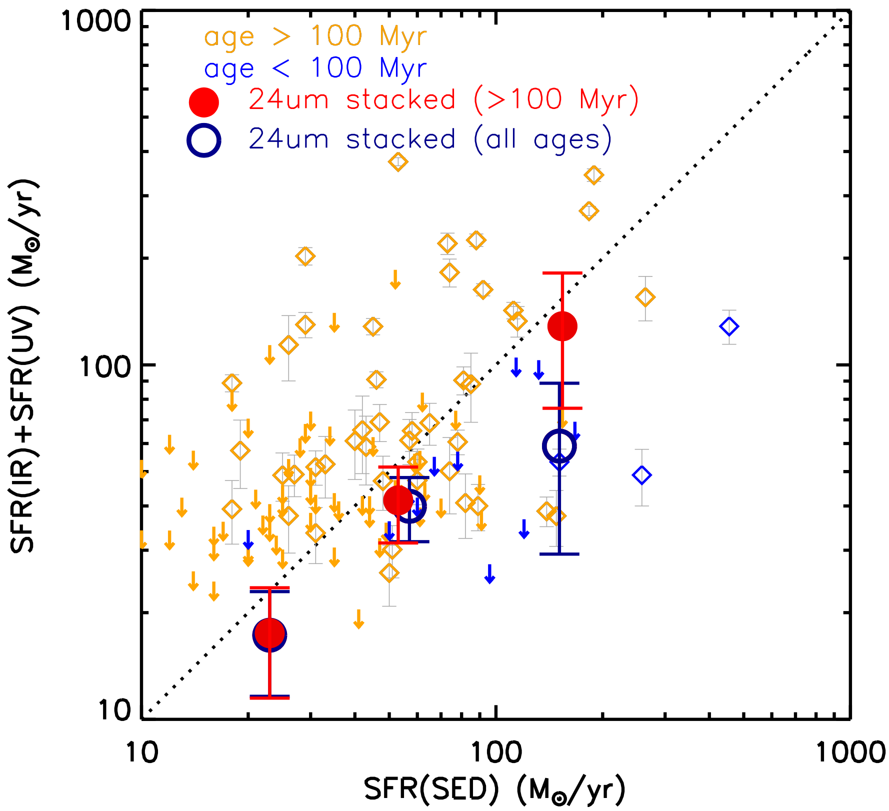

Figure 2.6 Comparison of the bolometric SFR and SED-inferred SFR. The values are divided into three bins of SFR(SED) including individual detections and individually undetected galaxies at 24 μm; Open blue circles include all objects and filled red circles include only those galaxies older than 100 Myr. Diamonds are individual detected objects and downward arrows represent 3σ upper limits in SFR(IR)+SFR(UV) for the MIPS undetected galaxies. Young galaxies (ages $<$ 100 Myr) are colored blue and galaxies with ages $>$ 100 Myr are orange. SFR(IR) error bars are estimated through bootstrap simulations and show the dispersion in the SFRs contributing to each stack. The last bin consists of galaxies with SFR(SED) $>$ 100 $M_{\odot}\,yr^{-1}$; by removing young galaxies (ages $<$ 100 Myr) about half of the sample in this bin is dismissed and we see the change between the two measurements (including and excluding the young ones). The dotted line indicates a one-to-one correspondence.

Once we remove galaxies with ages < 100 Myr, SFR(SED) agrees well with SFR(UV) + SFR(IR). An age-dependent L(UV)-to-SFR calibration (as we use here) does not decrease the difference between SFR(SED) and the bolometric SFR for stacks of all galaxies. It seems younger galaxies are at the same time less dusty (smaller bolometric SFR) but redder (larger SFR(SED)) than their older counterparts. These results are consistent with those of Reddy et al. (2006b), Reddy et al. (2010), and Wuyts et al. (2012), who find that galaxies with young stellar population ages are less dusty for a given UV slope than older galaxies. An SMC-like curve may be more appropriate for these galaxies. One possibility is that young galaxies have larger dust covering fractions than older galaxies (Reddy et al. 2010). A large dust covering fraction makes the UV slope redder for a given amount of dust attenuation. This study confirms that at $z \sim 2$ the Calzetti attenuation curve is applicable to star-forming galaxies older than 100 Myr, but a steeper attenuation curve may be necessary for the younger galaxies.

2.7 Summary

We have studied the multi-wavelength properties of a sample of ~ 200 galaxies with spectroscopically confirmed redshifts at $2.08 \leq z \leq 2.51$, to study the validity of commonly used dust correction recipes and to compare SFRs inferred from the Hα line luminosity, the UV continuum luminosity, and *Spitzer*/MIPS 24 μm measurements that are converted to the total IR luminosity. In this study, we benefit from using the broad-band photometry excess techniques to determine the Hα fluxes and, hence, conduct a large sample of $z \sim 2$ Hα measurements that is immune to uncertainties in the spectroscopic slit-loss corrections. The galaxies' properties are determined from stellar population model fitting to the rest-frame UV through near-infrared data. The main conclusions are as follows.

- By investigating several recipes for dust correcting the nebular emission lines, we find that assuming the same color excess of the ionized gas and the stellar continuum (i.e., $E(B-V)_{\rm neb} = E(B-V)_{\rm stel}$), and assuming that the Calzetti attenuation curve applies to both, results in the best agreement between SFR(Hα) and SFR(UV). If we assume the Calzetti curve to both the stellar and nebular regions but use $E(B-V)_{nebular}$=2.27 $E(B-V)_{stellar}$, the corrected SFR(Hα) measurements are inconsistent with the corrected SFR(UV)s at $\sim 5\sigma$ level, averaged on the five bins of SFR(UV) (see the right panel of Figure 2.4).

- Using the available *Spitzer*/MIPS data for $\sim$ 100 galaxies in our sample, we derive an observed $L_{H\alpha}$-to-SFR_{total} conversion factor of $(7.5 \pm 1.3) \times 10^{-42}$ $M_\odot$ yr^{-1} erg^{-1} s. This calibration is independent of any assumptions on the dust correction and can be used to convert the observed (extincted) Hα luminosity to a bolometric SFR when no dust attenuation measurements for the Hα luminosity is available.

- By comparing the stacks of SFR(UV)+SFR(IR) with the SED-inferred SFRs that are corrected for dust by the locally-derived Calzetti curve we conclude that a steeper attenuation curve (such as an SMC curve) may be necessary for galaxies younger than 100 Myr, as previous studies (Reddy et al. 2006b, 2010; Wuyts et al. 2012) have found. We find that applying the Calzetti curve to the stacks of all galaxies, including the young ones, results in SFR(SED)s that are inconsistent with the SFR(UV)+SFR(IR) at $\sim 2\sigma$ significance (the SFR(SED) in three mass bins of Figure 2.6 are inconsistent with SFR(UV)+SFR(IR) by 1, 2, and 3σ, from the lowest to highest mass bins respectively). The young galaxies have redder UV slope and at the same time lower bolometric SFR compared to their older counterparts. As a result, applying the Calzetti curve to the young galaxies overestimates the SED-inferred SFR when compared with their bolometric SFR. The Calzetti attenuation curve shows a good overall agreement for galaxies older than 100 Myr.

A more detailed investigation will include direct tracers of nebular dust extinction (i.e., the Balmer decrement). In the future studies, we plan to investigate this aspect with the MOSFIRE Deep Evolution Field (MOSDEF) survey, which uses the near-IR multi-object spectrograph MOSFIRE on the Keck I telescope to obtain spectroscopic measurements of the nebular emission lines for a sample of $\approx$ 1500 galaxies (Kriek et al. 2015).

Chapter 3

The MOSDEF Survey: Dissecting the star-formation rate vs. stellar mass relation using Hα and Hβ emission lines at $z \sim 2$*

Abstract We present results on the SFR-M_* relation (i.e., the "main sequence") among star-forming galaxies at $1.37 \leq z \leq 2.61$ using the MOSFIRE Deep Evolution Field (MOSDEF) survey. Based on a sample of 261 star-forming galaxies with observations of Hα and Hβ emission lines, we have estimated robust dust-corrected instantaneous star-formation

*A version of this chapter was published in: Shivaei, I., Reddy, N. A., Shapley, A. E., Kriek, M., Siana, B., Mobasher, B., Coil, A. L., Freeman, W. R., Sanders, R., Price, S., de Groot, L, & Azadi, M., *The Astrophysical Journal* 815, 98 (2015) rates (SFRs) over a large dynamic range in stellar mass ($\sim 10^{9.0} - 10^{11.5}\,\mathrm{M}_\odot$). We find a tight correlation between SFR(Hα) and M_* with an intrinsic scatter of 0.36 dex, 0.05 dex larger than that of UV-based SFRs. This increased scatter is consistent with predictions from numerical simulations of $0.03 - 0.1$ dex, and is attributed to Hα more accurately tracing SFR variations. The slope of the $\log(\mathrm{SFR}) - \log(M_*)$ relation, using SFR(Hα), at $1.4 < z < 2.6$ and over the stellar mass range of $10^{9.5}$ to $10^{11.5}\,\mathrm{M}_\odot$ is 0.65 ± 0.09. We find that different assumptions for the dust correction, such as using the stellar $E(B-V)$ with a Calzetti et al. (2000) attenuation curve, as well as the sample biases against red and dusty star-forming galaxies at large masses, could yield steeper slopes. Moreover, not correcting the Balmer emission line fluxes for the underlying Balmer absorption results in overestimating the dust extinction of Hα and SFR(Hα) at the high-mass end by 2.1 (2.5) at $10^{10.6}\,\mathrm{M}_\odot$ ($10^{11.1}\,\mathrm{M}_\odot$) and artificially increases the slope of the main-sequence. The shallower main-sequence slope found here compared to that of galaxy evolution simulations may be indicative of different feedback processes governing the low- and/or high-mass end of the main sequence.

3.1 Introduction

Star-forming galaxies show a relatively tight correlation between their star-formation rate (SFR) and stellar mass. This relation, commonly known as the star-forming *"main sequence"* (Noeske et al. 2007a), has been intensively studied over the past decade (e.g., at $z \sim 2$, Reddy et al. 2006a; Daddi et al. 2007a; Pannella et al. 2009; Rodighiero et al. 2011; Whitaker et al. 2012b; Wuyts et al. 2011b; Reddy et al. 2012b; Sawicki 2012; Schreiber et al. 2015; Whitaker et al. 2014b; Atek et al. 2014). The main sequence is generally assumed to be a linear relation between log(SFR) and log(M_*) with an associated scatter due to observational uncertainties and intrinsic scatter. The slope of the relation is primarily set by star formation efficiency as a function of stellar mass. The intrinsic scatter of the main-sequence relation is predicted to be due to variations in the gas accretion histories of different galaxies (Dutton et al. 2010) and indicates the level of burstiness in star formation history. The common physical interpretation of the tightness of the SFR-M_* relation is that the bulk of the stellar mass in star-forming galaxies is built in a relatively steady process, as opposed to a rapid starburst mode, as occurs in major mergers. The merger-driven starburst galaxies with high specific SFRs tend to lie above the main sequence relation (Rodighiero et al. 2011; Atek et al. 2014) and the quiescent galaxies that have little ongoing star formation, identified by their red near-infrared colors (Williams et al. 2009; Nayyeri et al. 2014), populate a region below the sequence (Noeske et al. 2007a; Wuyts et al. 2011b).

It has been argued that the majority of galaxies spend most of their lifetime on the main sequence (Noeske et al. 2007a). Therefore, studying the parameters of the main sequence and comparing them with the galaxy formation models can shed light on our understanding of processes that govern galaxy evolution, such as stellar and AGN feedback (Kannan et al. 2014; Torrey et al. 2014; Sparre et al. 2015a), gas accretion rates (Dutton et al. 2010), and gas inflows and outflows (Davé et al. 2011a). The SFR-M_* relation can be used as a test for galaxy evolution simulations to see how well the simulations can reproduce the observed universe (e.g., Behroozi et al. 2013b).

Determining the slope and intrinsic scatter of the main sequence can be hindered by sample selection effects, the diagnostic used to infer the SFR, and the method used to correct observed SFR for dust attenuation (for a summary see, Speagle et al. 2014). The UV-selected samples and the UV-inferred SFRs are biased against massive and dusty galaxies where the bulk of star formation is obscured and the UV slope is decoupled from extinction. Moreover, as SED- and UV-based SFRs are dependent on the same stellar population models used to infer the stellar masses, the scatter in the SFR-M_* relation may be underestimated when using SED or UV based SFR tracers (Reddy et al. 2012b). In order to overcome this issue, and more robustly measure SFRs for dustier galaxies, some studies have used SFR(IR)+SFR(UV) as a proxy for bolometric SFR (e.g., Reddy et al. 2006a; Schreiber et al. 2015; Whitaker et al. 2014b). However, estimating the SFR(IR) based solely on *Spitzer*/MIPS 24μm imaging has its shortcomings and could artificially tighten the main sequence if the scatter in L(IR) at a given L(8μm) luminosity is not taken into account (e.g., Utomo et al. 2014; Hayward et al. 2014).

We improve upon previous high-redshift studies by utilizing a representative sample of galaxies with measurements of the Hα and Hβ emission lines. These lines offer the advantage of probing star formation on shorter timescales than the UV and IR, they are largely independent of the stellar population, and thus can be used to more accurately assess the intrinsic scatter in the SFR-M_* relation.

The star-formation activity was at its peak at $z \sim 2$ (Reddy & Steidel 2009; Shapley 2011), making that redshift a critical epoch to study the evolution of galaxies. Obtaining rest-frame optical spectra of large samples of galaxies at $z \sim 2$ has been challenging until recently due to the high terrestrial background in the near-IR and the lack of multi-object near-IR spectrographs on 10-meter-class telescopes. The newly-commissioned MOSFIRE spectrograph (McLean et al. 2012) on the 10 m Keck I telescope has enabled us to build a large sample of galaxies at $z \sim 2$ with coverage in both the Hα and Hβ lines. In this study, we use a large sample of 261 rest-frame optically selected and spectroscopically confirmed galaxies at $1.4 < z < 2.6$, which was obtained as part of the MOSFIRE Deep Evolution Field (MOSDEF) survey (Kriek et al. 2015). To study the SFR-M_* relation, we use SFRs based on the Hα luminosity that are robustly corrected for dust attenuation using the Balmer decrement (L(Hα)/L(Hβ)). We demonstrate how different SFR diagnostics and dust correction recipes can alter the slope and scatter of the main sequence, and thus potentially affect our conclusions regarding the way in which galaxies build up their stellar mass at high redshift.

The outline of this paper is as follows. In Section 3.2, we present our sample properties and our measurements including SFRs and stellar masses. In Section 3.3, we describe the methodology we used to derive the main-sequence parameters. We compare the scatter of the SFR-M_* relation for different SFR indicators in Section 3.4. In Section 3.5, we discuss the slope of the SFR-M_* relation and the potential biases arising from sample selection, dust correction, and Balmer absorption correction. We compare our findings to previous studies in Section 3.6, and finally, the results are summarized in Section 3.7. Throughout this paper, a Chabrier (2003) Initial Mass Function (IMF) is assumed and a cosmology with $H_0 = 70$ km s^{-1} Mpc^{-1}, $\Omega_\Lambda = 0.7$, and $\Omega_m = 0.3$ is adopted.

3.2 Sample and Measurements

3.2.1 The MOSDEF Survey

The MOSDEF survey is a large multi-year survey with the MOSFIRE multi-object spectrometer on the Keck I telescope (McLean et al. 2012). The aim of the survey is to obtain rest-frame optical spectra of ~ 1500 H-selected galaxies to study their stellar, gaseous, metal, dust, and black hole content. The MOSDEF observations are conducted in five fields of the Cosmic Assembly Near-IR Deep Extragalactic Legacy Survey (CANDELS; Koekemoer et al. 2011; Grogin et al. 2011), consisting of AEGIS, COSMOS, GOODS-N, GOODS-S, and UDS, targeting three redshift bins: $1.37 \leq z \leq 1.70$, $2.09 \leq z \leq 2.61$, and $2.95 \leq z \leq 3.80$. Targets for spectroscopy are prioritized by their H-band magnitude (using the 3D-HST catalogs, Skelton et al. 2014) and the availability of spectroscopic, grism, and photometric redshifts, down to $H = 24.0$, 24.5, and 25.0 magnitude, for each redshift bin respectively.

Details of the survey strategy, observations, data reduction, and characteristics of the full galaxy sample are described in Kriek et al. (2015). In this study, we use the data accumulated from the first two years of the survey.

3.2.2 Hα Sample

Out of the full MOSDEF sample we selected a subsample of 342 galaxies that have secure redshifts and coverage of both the Hα and Hβ lines. These criteria limited our sample to the low and middle redshift bins that correspond to $1.37 \leq z \leq 1.70$ and $2.09 \leq z \leq 2.61$, respectively. There were 49 AGN that were identified and removed from the sample based on their IR and X-ray properties, as well as high [NII]/Hα ratios ([NII]/Hα> 0.5, Coil et al. 2015). In order to have secure SFR measurements, we further limited our sample to objects where the Hα line was detected with signal-to-noise (S/N) > 3. This selection resulted in a sample of 264 objects.

Among the Hα-detected galaxies, the Hβ fluxes of 19% (48 out of 264) were below 3σ. Out of these 48 Hβ-undetected objects, 40 (83%) had a bright sky line close to the Hβ line, while for the detected Hβ sample the fraction was only 34%. The higher frequency of skyline contamination in the Hβ-undetected sample contributes to the lower Hβ detection rate among these galaxies.

To assess the relation between SFR and M_* for star-forming galaxies, we proceeded to remove all those galaxies that were deemed to be "quiescent". In particular, we used a rest-frame U–V versus V–J color selection (Williams et al. 2009) to identify the quiescent galaxies. There was only one object in the Hα-Hβ detected sample and two in the Hβ undetected sample that were identified as quiescent and thus removed from the sample, leaving a final sample of 261 galaxies, with 215 detected in both lines. The redshift distribution is shown in Figure 3.1.

3.2.3 Line Flux and Balmer Absorption Measurements

For each object, an initial redshift was estimated based on the emission line with the highest S/N ratio. The line fluxes were then measured by fitting Gaussian functions to the line profiles. The Hα and [NII]$\lambda\lambda$6548,6584 doublet were fit using three Gaussian functions. To estimate the uncertainty in the line fluxes, the spectra were perturbed within

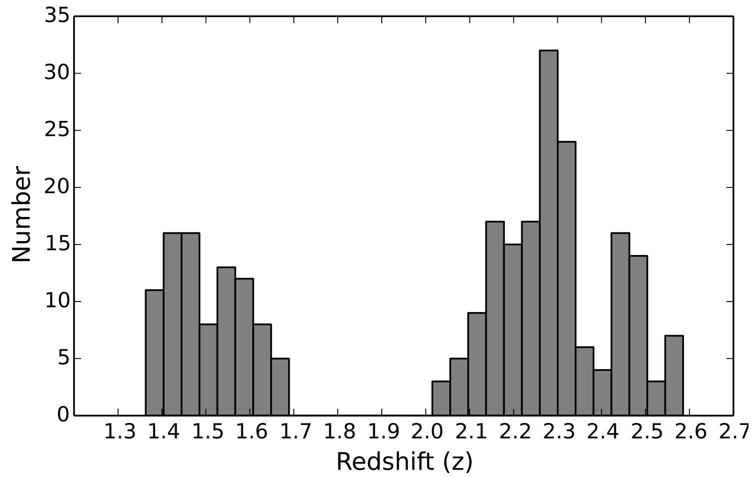

Figure 3.1 Redshift distribution of 261 star-forming galaxies in our sample with Hα detections and coverage of the Hβ line. There are 88 objects at $z \sim 1.5$ and 173 at $z \sim 2.3$.

the error spectra and all emission lines were re-fit. The dispersion among perturbed spectra was taken as the uncertainty in the line fluxes (Kriek et al. 2015).

An important aspect in determining the Balmer emission line fluxes is to correct for the underlying absorption that is produced in the atmosphere of primarily A-type stars. The Balmer absorption fluxes were determined from the best-fit SED models to the multi-wavelength photometry (see Section 3.2.4), and were added to the emission line fluxes to get the total, absorption-corrected fluxes. For objects with Hα (Hβ) detected at $> 3\sigma$ level, ratio of the average Hα (Hβ) Balmer absorption flux to the average Hα (Hβ) observed flux is $\sim 2\%$ ($\sim 15\%$).

3.2.4 Mass and SFR Determination

The stellar masses were determined through a χ^2 minimization SED fitting procedure assuming Bruzual & Charlot (2003) models for solar metallicity, a Chabrier IMF, the Calzetti et al. (2000) dust attenuation curve with $0.0 \leq E(B-V) \leq 0.6$, rising star-formation histories and a 50 Myr lower limit on the age of the galaxies, assumed to be the typical dynamical time scale at this redshift (see, Reddy et al. 2015). The SED-fitting was performed using photometry from the 3D-HST catalogs (Brammer et al. 2012; Skelton et al. 2014) that has been corrected for the strongest emission lines measured in the MOSDEF survey, including [OII]$\lambda\lambda$3727,3730, [OIII]$\lambda\lambda$4960,5008, Hβ, and Hα (Reddy et al. 2015). Errors in the SED parameters were estimated through Monte Carlo simulations; each photometric flux was randomly perturbed assuming a Gaussian distribution centered at the measured value with a standard deviation equal to the photometric error. This procedure was repeated many times and each photometric realization was refit to find the best-fit SED model. The standard deviation of the simulated SED parameters was taken as the error in the respective parameter.

We converted the Hα luminosity to SFR using the Kennicutt (1998) relation modified for a Chabrier (2003) IMF, and corrected for dust attenuation using the nebular $E(B-V)$ derived from the Balmer decrement (Hα/Hβ), assuming a Galactic extinction curve taken from Cardelli, Clayton, & Mathis (1989, CCM). To determine the standard deviations in the corrected SFRs, we perturbed the measured Hα and Hβ fluxes according to their uncertainties many times and recalculated the corrected SFRs based on each flux realization. We also accounted for spectroscopic slit losses[1] by adding an additional uncertainty of 16% (20%) to the Hα (Hβ) measurement uncertainties in quadrature (Kriek et al.

[1]The slit loss uncertainty accounts for the loss of flux of a resolved source outside of the slit aperture. We calculated the slit loss uncertainty in our flux calibration by comparing the SED-inferred fluxes of the continuum detected galaxies in MOSDEF with their spectroscopic fluxes. For a full description, see Section 3.3, Kriek et al. (2015).

2015). Where Hβ is undetected, a 3σ upper limit on the Hβ flux was used to estimate a lower limit on the nebular $E(B-V)$ and the corresponding dust-corrected SFR.

We used the ancillary 3D-HST broad- and medium-band photometry at rest-wavelengths 1268 – 2580 Å to find the UV luminosity at 1600 Å and the UV slope by fitting a power law to the photometry ($f_\lambda \propto \lambda^\alpha$). The UV slope was used to correct the UV luminosity for dust attenuation, following the Meurer et al. (1999) relation. We did not use the SED-inferred $E(B-V)$ because it is correlated with the stellar mass as both quantities are determined through SED fitting. The luminosities were converted to SFRs using the Kennicutt (1998) relation, adjusted for a Chabrier IMF.

3.2.5 Stacking Procedure

To further investigate the SFR-M_* relation and the role of the Hβ-undetected objects, we employed spectral stacks constructed in the following manner. Individual spectra were converted from flux density to luminosity density, normalized by the Hα luminosity, and interpolated to a rest-frame grid with wavelength spacing of 0.5 Å. The composite spectrum was then created by taking the average of the individual spectra, weighted by inverse variance of the error spectra. The composite error spectrum was estimated as the square root of the variance of the weighted mean.

The composite Hα and Hβ lines were fit with a Gaussian profile. The errors on the line fluxes are derived using the standard deviation of the distribution of line fluxes by perturbing the stacked spectrum according to the composite error spectrum and recalculating the line fluxes 1000 times. The composite line fluxes were corrected for Balmer absorption using the mean absorption, inversely weighted by flux error of the individual galaxies contributing to the bin (the individual Balmer absorptions were inferred from the best-fit stellar models). The normalized composite spectrum was used to derive the Hα/Hβ ratio. To assess the total flux of the lines, we stacked the individual spectra without normalizing them by the individual Hα luminosities.

3.3 The Main Sequence Analysis

The correlation between stellar mass and SFR has been studied intensively since Brinchmann et al. (2004). As a first step in studying this correlation in our Hα- and Hβ-detected sample, we calculated the Spearmans rank correlation coefficient (ρ) between the SFR(Hα) and stellar mass. We obtained $\rho = 0.57$ at 8σ, indicating a significant positive correlation between the two quantities.

The SFRs versus stellar masses of individual galaxies are plotted in Figure 3.2. The stacked SFRs in five stellar mass bins (the first bin is $\log(M_*/M_\odot) < 9.5$ and the rest are divided by 0.5 dex widths, Section 3.2.5) are also plotted on top of the individual points. In this section, we describe our low-mass completeness, the fitting methodology, and discuss the effect of Hβ nondetections and AGN on the SFR-M_* relation.

3.3.1 Mass Completeness

As it is evident from Figure 3.2, the stacked SFR of the first mass bin is elevated compared to the best-fit line. In this section, we discuss the completeness of our sample and address the possible causes of incompleteness at low stellar masses.

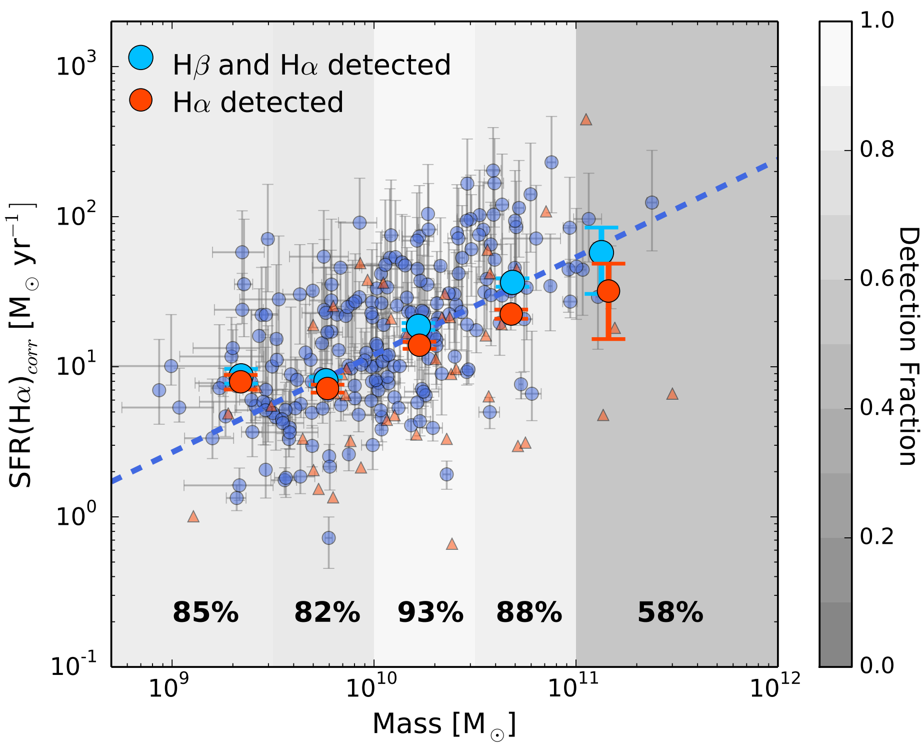

Figure 3.2 SFR(Hα) as a function of stellar mass for star-forming galaxies at $z = 1.37 - 2.61$, known as the star-forming main sequence. The individual points show galaxies with detected Hα and Hβ and the triangles are those with undetected Hβ, for which 3σ lower limits of the dust corrected SFRs are plotted. The dashed line is the best linear fit to the individual detected galaxies with $\log(M_*/M_\odot) > 9.5$. The larger circles are stacks in five mass bins, taking into account only the detected galaxies (the light blue circles) and including the Hβ non-detections (the red circles). The shaded regions and numbers on the bottom represent the fraction of galaxies with robust redshifts and Hα detection with respect to the targeted objects in each mass bin.

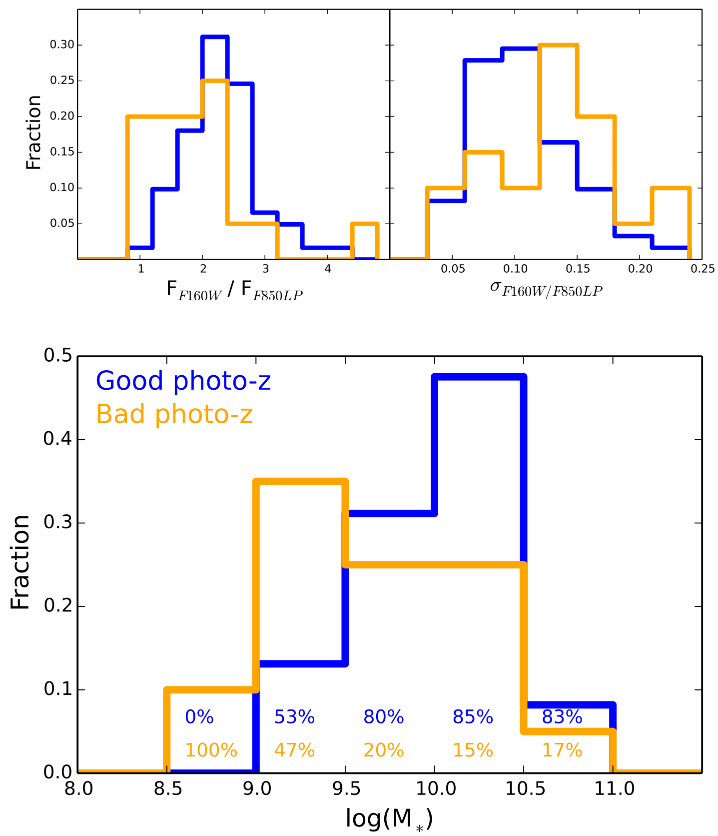

Figure 3.3 *Top:* Distribution of *F160W* to *F850LP* flux ratio (left) and the corresponding uncertainty (right) of UV-selected galaxies in the MOSDEF parent sample with spectroscopic redshifts at $z = 2.09 - 2.61$ (Reddy et al. 2006b) in the GOODS-N field. The fluxes and uncertainties are from the 3D-HST photometric catalog (Skelton et al. 2014). The orange histogram denotes galaxies with photometric redshifts that fall outside of the spectroscopic redshift range (bad photo-z). The blue histogram shows galaxies with photometric redshifts in the same range as the spectroscopic redshift (good photo-z). The galaxies with bad photo-z's have on average bluer colors and larger uncertainties, indicative of a weaker Balmer/4000 Å break compared to the good photo-z galaxies. *Bottom:* stellar mass distribution of the same samples described above. The orange/blue numbers indicate fraction of galaxies with bad/good photo-z's in each mass bin relative to the total number of galaxies in the corresponding bin. The histograms in these figures show the fractions, not the actual numbers. Therefore, the relative bin heights do not correspond to the percentage numbers on the bottom and should not be confused with each other.

The redshifts of targets in the MOSDEF parent sample were adopted primarily from the 3D-HST grism measurements or other available spectroscopic campaigns (see, Kriek et al. 2015). When a spectroscopic redshift was not available, which was the case for 67% of the whole sample and 73% of the objects with $M_* < 10^{9.5}\,M_\odot$, redshifts were estimated using the 3D-HST photometry and the EAZY SED-fitting code (Brammer et al. 2008). Objects with secure photometric redshifts may be biased against those objects with weak Balmer/4000 Å breaks (and hence youger ages and lower masses). To assess the magnitude of this bias, we cross correlated our sample with the Reddy et al. (2006b) spectroscopic sample of UV-selected galaxies in the GOODS-N field. Rest-frame UV-selected samples are immune to the bias mentioned above as their selection criteria are not dependent on the strength of the Balmer or 4000 Å break.

There were 81 galaxies at $z_{\rm spec} = 2.09 - 2.61$ that were in common between the MOSDEF and the UV-selected sample. We divided the common galaxies into two sets: those that have photometric redshifts in the same range as their spectroscopic redshifts of $z = 2.09 - 2.61$ (good photo-z, 61 objects), and those with photometric redshifts outside of this range (bad photo-z, 20 objects). The bad photo-z objects are not scatted symmetrically around $z_{\rm spec} = 2.09 - 2.61$; their photometric redshifts are systematically lower than our target redshift range, i.e., $z_{\rm phot} < 2.09$.

The two filters that bracket the Balmer break are *HST* WFC3 *F160W* and *HST* ACS *F850LP*, which were available for all 81 galaxies examined here. As expected, the galaxies with incorrect photometric redshifts had on average bluer *F160W* - *F850LP* colors, with larger uncertainties. The distributions of the flux ratios and the associated uncertainties are plotted in Figure 3.3. Were it not for prior spectroscopic redshifts, those galaxies with bad photo-z's would have been missing from our sample. The conclusion is further supported by the two-sided Kolmogorov-Smirnov test, which indicates a low probability of $P \simeq 0.017$ that the *F160W* - *F850LP* color distribution of the good and bad photo-z sets are drawn from the same parent distribution.

The stellar-mass distributions of the two sets of galaxies are shown in the bottom panel of Figure 3.3, with the fraction of galaxies in each mass bin written on the bottom of the plot. The distributions indicate that the majority of galaxies with stellar masses below $10^{9.5}\,\mathrm{M}_\odot$ would have been missed from the MOSDEF sample if we had relied on their photometric redshifts. Therefore, to avoid any biases we limited our main-sequence analysis to those with $M_* > 10^{9.5}\,\mathrm{M}_\odot$. There are 128 and 185 galaxies above $10^{9.5}\,\mathrm{M}_\odot$ at $z = 2.09 - 2.61$ and $z = 1.37 - 2.61$, respectively. The dashed line in Figure 3.2 is the linear regression fit to the individual galaxies with $M_* > 10^{9.5}\,\mathrm{M}_\odot$. The low mass limit we adopted is also the limit above which the inferred main-sequence slope (see Section 3.3.2) deviates by greater than 1σ from the slope over the full stellar mass range, including the low mass galaxies.

The other possible bias at the low-mass end of our sample is a Malmquist bias, due to the fact that our requirement of an Hα detection may bias against objects with faint Hα emission. To test this possibility, we calculated the fraction of galaxies that were detected in Hα to the number of galaxies targeted for spectroscopy, in bins of stellar mass. The fractions are listed on the bottom of Figure 3.2. The detection fraction of the first bin (the lowest mass bin) is similar to that of the higher mass bins, indicating that by limiting our

Table 3.1. Parameters of the log(SFR) − log(M_*) Linear Fit [a]

Redshift Range	SFR Indicator	Slope	Intercept	Observed Scatter	Intrinsic Scatter
$z = 1.37 - 2.61$	Hα[c]	0.65 ± 0.09	-5.42 ± 0.88	0.40	0.36
(N = 185)[b]	UV_β[d]	0.63 ± 0.08	-5.07 ± 0.83	0.34	0.31
	SED[e]	0.80 ± 0.06	-6.79 ± 0.56	0.28	0.27
	UV_{SED}[f]	0.79 ± 0.07	-6.57 ± 0.68	0.27	0.21
$z = 2.09 - 2.61$	Hα[c]	0.59 ± 0.11	-4.68 ± 1.06	0.36	0.31
(N = 128)[b]	UV_β[d]	0.71 ± 0.10	-5.82 ± 0.96	0.31	0.27
	SED[e]	0.83 ± 0.07	-7.01 ± 0.74	0.29	0.27
	UV_{SED}[f]	0.74 ± 0.10	-6.07 ± 1.00	0.28	0.20

[a]The parameters are calculated for galaxies with $M_* > 10^{9.5}\,M_\odot$, using an OLS linear regression method

[b]Number of objects

[c]The Hα SFR is dust corrected by Balmer decrement, assuming the Cardelli Galactic extinction curve

[d]The UV SFR is dust corrected by the UV slope, assuming the Calzetti attenuation curve

[e]The SFR inferred from the stellar population model, assuming the Calzetti curve for dust attenuation

[f]The UV SFR is dust corrected by the $E(B-V)$ inferred from the SED model, assuming the Calzetti attenuation curve

sample to the Hα-detected objects we did not miss a significantly higher fraction of galaxies at low masses.

The rest-frame optically selected sample of the MOSDEF survey is less prone to missing highly obscured galaxies at high stellar masses, compared to the UV-selected samples. The effect of this potential bias of UV-selected samples versus our sample will be discussed in Section 3.5.2.

3.3.2 Methodology

There are various linear regression methods that can be used to characterize a correlation between two variables. In most studies of the SFR-M_* relation, the correlation between SFR and M_* has been determined using the ordinary least-squares regression (OLS). In the OLS method, one variable (here, the SFR) is assumed as the dependent variable and the regression line is defined to be that which minimizes the sum of the squares of the vertical distances between the data points and the regression line. The OLS method should be used in science cases where there is an independent variable that is estimated confidently and will be used to predict the other variable. As over a galaxy's lifetime the stellar mass is built relatively smoothly as opposed to the SFR, which can be stochastic and vary to a greater extent, we are more interested in determining the scatter and mean of SFR as a function of stellar mass. For this purpose, the OLS method is a valid statistical procedure to be used for characterizing the SFR-M_* relation.

We determined the best estimates for the OLS regression slope and intercept by perturbing the data according to the stellar mass and SFR uncertainties 1000 times and calculating the median of the slope and intercept distributions. The slope and intercept uncertainties were calculated based on the OLS method error estimates in Isobe et al. (1990). Isobe et al. (1990) estimated the errors of regression parameters for linear relations where there is an intrinsic scatter. The average of the uncertainties obtained for the individual realizations was adopted as the uncertainty in the regression coefficients. We found a slope of 0.65 ± 0.09 for SFR(Hα) at 1.37$<z<$2.61, and 0.59 ± 0.11 for the 2.09$<z<$2.61 sample only, with a lower mass limit of $10^{9.5}\,M_\odot$. The relation is presented in Figure 3.2 and Table 3.1. The SFR-M_* relation was not investigated separately for the sample at $1.37 < z < 1.70$ due to the small number of galaxies at this redshift range.

In the OLS method, the scatter is defined as the scatter in SFR at a certain stellar mass. We estimated the total observed scatter by calculating the dispersion in the distribution of vertical distances from the best-fit line. We propagated the mean measurement errors of mass and SFR[2] and subtracted them (in quadrature) from the total observed scatter to obtain the intrinsic scatter. We found an intrinsic scatter of 0.36 dex for SFR(Hα). This intrinsic scatter still includes galaxy-to-galaxy variations in the dust corrections.

An alternative statistical procedure to the OLS method is a regression method that treats the two variables symmetrically, such as the OLS bisector method. The OLS bisector is recommended to be applied in cases where an underlying functional relation between two independent variables is studied (Isobe et al. 1990). The scatter in this method is the scatter about the best-fit line to the relation. For a comparison, we reported the OLS bisector values in Table 3.2. We should emphasize that as we are most interested in determining the scatter and mean of SFR at a given stellar mass, the OLS method is the one on which we based our main conclusions.

3.3.3 Nondetections

It is important to investigate whether excluding the Hβ nondetections from the main analysis causes any biases. In other words, do the Hβ-undetected galaxies represent different physical characteristics or are they undetected due to observational shortcomings? We stacked the spectra of the Hβ-undetected objects as described in Section 3.2.5, and derived the dust-corrected SFR(Hα) using the stacked spectrum. In the composite spectrum,

[2]The uncertainty due to spectroscopic slit losses is included in the SFR error estimates as well (Section 3.2.4).

Table 3.2. Parameters of the log(SFR) − log(M_*) Linear Fit, Using The OLS Bisector Method [a]

Redshift Range	SFR Indicator	Slope	Intercept	Observed Scatter	Intrinsic Scatter
$z = 1.37 - 2.61$	Hα [c]	1.26 ± 0.07	-11.57 ± 0.69	0.33	0.30
(N = 185) [b]	UV$_\beta$ [d]	1.14 ± 0.06	-10.33 ± 0.62	0.29	0.26

[a] The parameters are calculated for galaxies with $M_* > 10^{9.5}\,M_\odot$

[b] Number of objects with $M_* > 10^{9.5}\,M_\odot$

[c] The Hα SFR is dust corrected by Balmer decrement, assuming the Cardelli Galactic extinction curve

[d] The UV SFR is dust corrected by the UV slope, assuming the Calzetti attenuation curve

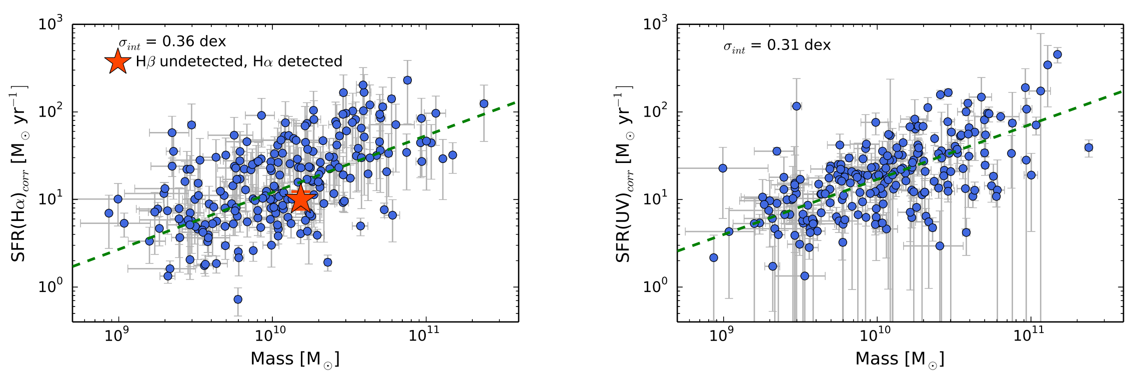

Figure 3.4 SFR as a function of stellar mass for star-forming galaxies at $z = 1.37-2.61$. *Left:* SFR(Hα) – corrected for dust attenuation assuming the Balmer decrement and a Cardelli et al. (1989) extinction curve – versus M_*. The red star shows the weighted-average stack of the Hβ-undetected galaxies, where its mass is the median of the mass of galaxies in the stack. The stacked point is within the SFR(Hα) scatter of 0.36 dex, suggesting that those galaxies undetected in Hβ have on average a similar proportion of SFR given their stellar mass, as those galaxies with both lines detected. *Right:* SFR(UV) versus M_*. The SFR is inferred from the UV luminosity at 1600Å and is dust corrected by the UV slope, both determined from the multi-band photometry at 1268–2580Å (Skelton et al. 2014). The green lines show the regression lines fitted to log(SFR) − log(M_*) relation. The intrinsic scatter in SFR (i.e., the scatter after the subtraction of SFR and mass measurement uncertainties) is provided on the upper left corners of each plot.

the stacked Hβ line is detected at 3.9σ. The stacked SFR and median stellar mass of the undetected-Hβ objects are plotted on top of the SFR-M_* relation in Figure 3.4 as the red star. The star lies below the linear fit by 2.5σ, but is still within the SFR(Hα) scatter of 0.36 dex, implying that these objects are not on average intrinsically different from the detected objects and excluding them should not systematically bias the SFR-M_* relation. As mentioned in Section 3.2.2, this conclusion is further supported by the fact that the spectra of a large fraction of these galaxies are contaminated by skylines.

3.3.4 AGN

As mentioned before in Section 3.2, AGN were identified through X-ray, IR, and optical line observations and removed from the sample. The AGN mostly reside on the high mass end of the main sequence and it is interesting to examine how they would change the slope and scatter of the SFR-M_* relation. Here, we assumed that all of the rest-frame UV continuum emission in AGN host galaxies is coming from the stellar population; we determined the SFRs from the UV luminosity at 1600 Å, dust corrected using the UV slope, and estimated the masses through the SED modeling. Including the AGN does not change the slope significantly (0.66 ± 0.09) but results in a larger scatter (0.41 dex) that is mainly occurring at the massive end, as most of the AGN have larger stellar masses than the typical stellar mass of the star-forming objects. This is a well-understood selection effect for AGN that they are easier to detect in more massive galaxies (Aird et al. 2012).

3.4 The Scatter of The Main Sequence

In this section, we investigate how the main sequence scatter changes as we consider UV- or Hα- based SFRs. The UV luminosity at 1500 to 2800 Å is one of the most commonly used SFR diagnostics at $z \sim 2$, which traces stars with $M_* \gtrsim 5\,\mathrm{M}_\odot$ and ages $\lesssim 100\,\mathrm{Myr}$ (Kennicutt 1998; Kennicutt & Evans 2012). Another common SFR indicator, the Hα luminosity, is sensitive to more massive ($M_* \gtrsim 15\,\mathrm{M}_\odot$) and shorter lived stars (ages $\lesssim 10\,\mathrm{Myr}$) that provides an effectively instantaneous measure of the SFR (Kennicutt & Evans 2012). The intrinsic scatter in SFR(Hα) versus M_* and SFR(UV) versus M_*, calculated as described in Section 3.3.2, are presented in Table 3.1 and Figure 3.4. For a fair comparison, we limited our UV sample to the same sample as the Hα detected galaxies.

The intrinsic scatter in the SFR(Hα)-M_* relation is 0.05 dex larger than that of the SFR(UV)-M_* relation. The smaller SFR(UV) vs. M_* scatter is partly due to the degeneracy between SFR(UV) and M_*, as the SED modeling where the M_* is inferred from relies on the UV color to constrain the dust reddening. The stochasticity in star formation can also cause larger scatter in SFR(Hα) as Hα traces star formation on timescales shorter than those probed by the UV continuum. For instance, it has been suggested in galaxy formation simulations (Domínguez et al. 2015) that star formation proceeds stochastically in low mass galaxies such as dwarfs; but even for a massive galaxy ($z = 0$ halo mass of $10^{12}\,\mathrm{M}_\odot$) with a typical merger history, the dispersion in SFR averaged over timescales of $\sim 10^8$ years could be $\sim 0.03 - 0.1$ dex smaller than the scatter of SFR averaged over shorter timescales of $\sim 10^7$ years (Hopkins et al. 2014; Sparre et al. 2015a; Domínguez et al. 2015).

Prior to the use of multi-wavelength estimates of the SFR (e.g., SFR(IR) + SFR(UV)), it was common to assess the SFR-M_* relation using SED-inferred SFRs (e.g., Magdis et al. 2010; Sawicki 2012). To investigate how SFR(SED) would affect the relation, we also calculated the scatter using SED-inferred SFR and UV SFR, where the latter was corrected by the SED-derived $E(B-V)$ rather than the UV slope. The scatter in SFR is reduced to 0.27 and 0.21 dex for SFR(SED) and SFR(UV), respectively (the last two rows in Table 3.1). These values likely underestimate the true scatter in the SFR-M_* relation, because the SFR(SED) and the SED-inferred $E(B-V)$ are highly correlated with the SED-derived stellar masses.

The scatter reported here is not due to measurement uncertainties but it may be affected by other factors such as galaxy-to-galaxy variations in IMF and dust corrections. Galaxy formation simulations suggest various drivers for the scatter in SFR-M_* relation. Dutton et al. (2010) argued that the source of the small scatter they derived (0.12 dex) is the variance in mass accretion histories for halos of a given virial mass, but Davé et al. (2012) suggested that the more complex relation between the gas inflow rate and the dilution time, which shows how quickly galaxies can return to equilibrium after being perturbed away from the main sequence also influences the scatter. Our larger intrinsic scatter of 0.36 dex may indicate that the gas accretion and star-formation histories are not as smooth as predicted by the simulations.

3.5 The Slope of The Main Sequence

In this section, we focus on the slope of the main-sequence relation for the SFR(Hα) sample. The inferred slope (see Section 3.3.2 for the methodology) is 0.59 ± 0.11 for the $z \sim 2.3$ sample and when we include the $z \sim 1.5$ sample the slope is 0.65 ± 0.09, at $M_* > 10^{9.5}\,\mathrm{M}_\odot$ (refer to Section 3.3.1 for the discussion on the low-mass limit). The slope of the full sample (i.e., $M_* > 10^{9.0}\,\mathrm{M}_\odot$) is 0.56 ± 0.09.

There are many studies in the literature that parameterize the SFR-M_* relation and their reported slopes span in a wide range of $\sim 0.3 - 1.0$ (e.g., Daddi et al. 2007a; Dunne et al. 2009; Pannella et al. 2009; Santini et al. 2009; Rodighiero et al. 2011; Karim et al. 2011; Zahid et al. 2012; Reddy et al. 2012b; Whitaker et al. 2012b; Sobral et al. 2014; Atek et al. 2014). Various effects could lead to discrepancies in the slope estimates. In this section, we try to address three of the most significant effects by investigating them in our sample.

3.5.1 Dust Correction

The method used for dust correction affects the derived slope of the SFR-M_* relation. In high-redshift studies, a commonly used dust correction method for the nebular lines is to multiply the $E(B-V)$ derived for the stellar continuum by 2.27 factor and assume the Calzetti et al. (2000) attenuation curve. It has been shown in some previous studies that this recipe overestimates the corrected Hα SFRs for UV-selected galaxies (e.g., Reddy et al. 2010; Steidel et al. 2014; Shivaei et al. 2015a). In the top panel of Figure 3.5 we compared the Hα SFRs corrected by $E(B-V)_{\mathrm{nebular}}$, computed from the Balmer decrement, with

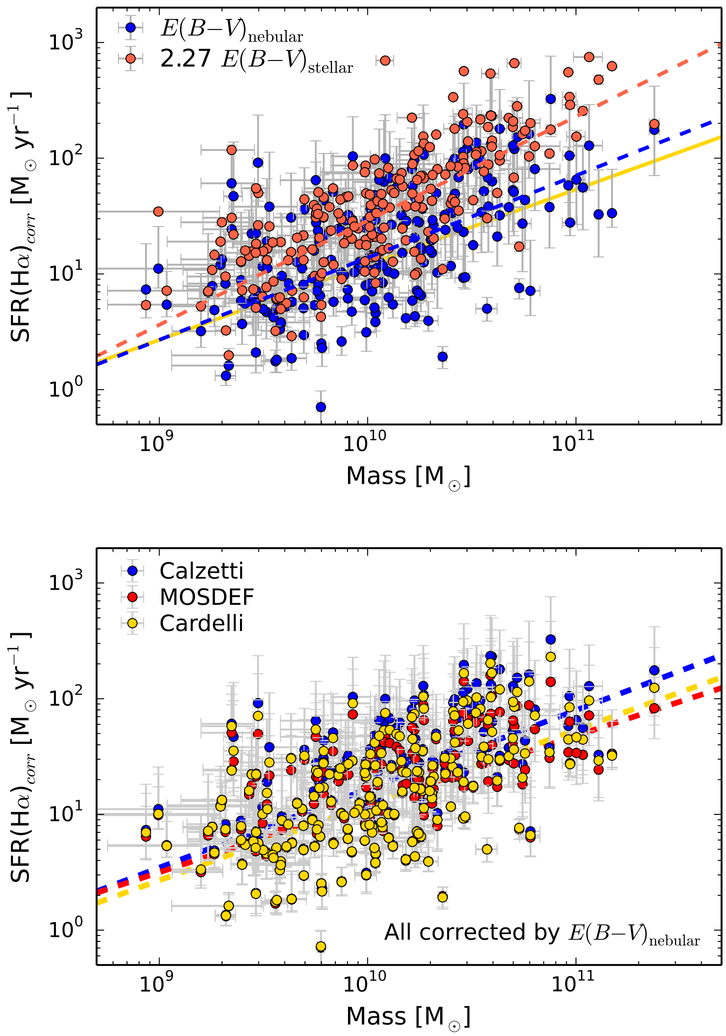

Figure 3.5 The SFR(Hα)-M_* relation, where the SFR is corrected for dust attenuation by different methods and attenuation curves. *Top:* The blue dots show SFR(Hα) dust corrected by the nebular $E(B-V)$ (derived from the observed Balmer decrement) and assuming a Calzetti curve. The red dots represent the SFR(Hα) corrected by the SED inferred $E(B-V)$ multiplied by 2.27, again assuming a Calzetti curve. The latter is a method that is commonly used in high-redshift studies to correct the Hα luminosities without having access to the Balmer decrement. This method overestimates the corrected SFRs and results in a steeper slope (0.90 ± 0.07) compared to the nebular corrected SFRs (slope $= 0.71 \pm 0.09$). The dashed lines show the linear fits to galaxies with $\log(M_*/M_\odot) > 9.5$. The yellow line is the linear fit to galaxies corrected by nebular $E(B-V)$ but assuming a Cardelli Galactic extinction curve, which we used as a default in this study. *Bottom:* The SFR-M_* relation for the same set of galaxies, corrected with the nebular $E(B-V)$ assuming three different dust curves: the Calzetti curve, the MOSDEF curve, and the Cardelli curve. The best-fit lines are shown with the relevant colors. All three slopes are consistent with each other within their uncertainties.

those corrected by $2.27 \times E(B-V)_{\rm SED}$. We emphasize that this practice was done solely for the purpose of demonstrating how the commonly used dust correction recipes could potentially affect the parameterization of the SFR-M_* relation in the absence of Balmer decrement measurements. The SFRs corrected with $2.27 \times E(B-V)_{\rm SED}$ assuming the Calzetti curve yield a main sequence slope of 0.90 ± 0.05, while the slope of those corrected by the $E(B-V)_{\rm nebular}$ with the Calzetti curve is 0.71 ± 0.09. The steeper slope is expected as the color-excess ($E(B-V)$) increases with stellar mass (e.g., Garn & Best 2010) and multiplying $E(B-V)$ by a factor (here, 2.27) causes a more significant difference at higher masses.

We also investigated the potential effect of the assumed attenuation curve on the best-fit slope of the SFR-M_* relation. We corrected the observed Hα SFRs assuming different attenuation curves: the Calzetti curve (Calzetti et al. 1994), the attenuation curve derived from galaxies in the MOSDEF sample (Reddy et al. 2015), and the CCM curve (Cardelli et al. 1989). The first two are stellar attenuation curves while the latter is a line of sight extinction curve that we used to correct the Hα luminosities throughout this paper. The results are presented in the bottom panel of Figure 3.5. The nebular color excess (i.e., $E(B-V)_{\rm nebular}$) does not change significantly between the three curves, the reason being that the shapes of these three curves in the rest-frame optical are very similar. The main difference arises from normalization of the curves, affecting the total attenuation correction. Reddy et al. (2015) showed that assuming the Calzetti curve for the nebular lines as opposed to the CCM curve results in higher SFRs, where the difference increases with increasing SFR (see Figure 21 in Reddy et al. 2015). We see the same trend here in Figure 3.5, namely that the discrepancy between corrected SFRs is larger at higher SFRs. Despite the change in SFR, the three main sequence slope estimates are consistent with each other within their uncertainties.

3.5.2 Sample Selection

Selection effects can have a major effect on the derived main-sequence slope. The samples that are selected based on rest-frame UV colors (such as Lyman-break selection, Steidel et al. 2003, 2004) are biased towards less dusty galaxies. Adding the redder and more dust-attenuated *star-forming* galaxies to these samples results in shallower slopes (Whitaker et al. 2012b; Speagle et al. 2014). To test this effect on our sample, we divided the star-forming galaxies into a blue bin and red bin, based on their UV and VJ colors. Previously, we used the UVJ diagram to remove the quiescent galaxies from our sample (Section 3.2.2), and now we set another criterion on the star-forming part of the diagram to separate the blue and red star-forming galaxies. The selection regions are shown in Figure 3.6. After the removal 21 galaxies that were classified as red star-forming, the slope of the relation increases to 0.75 ± 0.11. These galaxies are both more dust-attenuated and older compared to the rest of the sample. A steeper slope is expected as the red star-forming galaxies dominate the lower right corner of the main sequence (those with lower specific SFRs). In conclusion, the red star-forming galaxies should be included in a complete sample, otherwise the slope of the SFR-M_* relation may be overestimated.

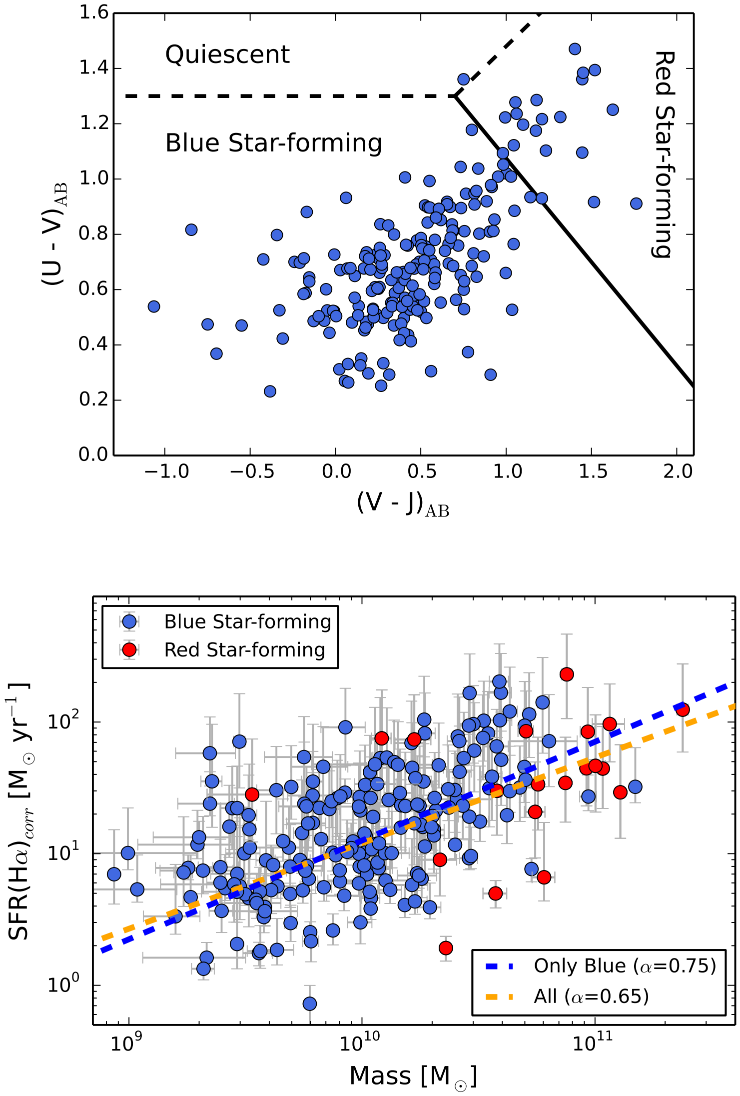

Figure 3.6 *Top:* distribution of our Hα and Hβ detected sample at $z = 1.4 - 2.6$ in the rest-frame UVJ diagram. The solid line separates blue and red star-forming galaxies. *Bottom:* SFR(Hα) versus M_* for the blue and red star-forming galaxies. The SFR-M_* slope of the blue star-forming sample is steeper than the slope of the whole sample, including the red star-forming galaxies.

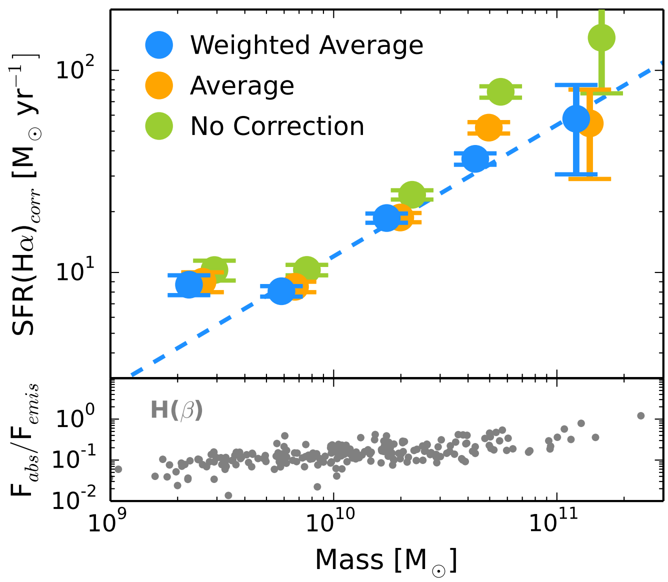

Figure 3.7 *Top:* the SFR-M_* relation for stacks of galaxies in five bins of stellar mass, the difference being in how the stacked Hα and Hβ luminosities are corrected for the underlying Balmer absorption. For illustrative purposes each set of colored points is slightly shifted in mass direction. *Blue symbols:* the Balmer absorption in each bin is estimated as the weighted average of the individual absorption fluxes. *Orange symbols:* the same as the blue points, but the average is used instead of the weighted average. *Green symbols:* No absorption correction is applied. *Bottom:* ratio of the Hβ absorption flux to the emission flux as a function of stellar mass. The absorption flux becomes stronger with stellar mass, which results in a more significant correction for galaxies with higher stellar masses.

Considering that the MOSDEF sample is a near-IR selected sample and because the Hα luminosity is less affected by dust attenuation than the shorter-wavelength UV luminosity, this study is less prone to the bias associated with UV selection.

3.5.3 Balmer Absorption Correction

Another factor that affects the main sequence parameterization in studies that use the hydrogen Balmer lines is the Balmer absorption correction. For the star-forming galaxies considered in this study, the difference between the absorption corrected SFRs and those that are not corrected becomes larger at higher masses because the absorption flux, which is produced in the atmosphere of primarily A-type stars, increases as a function of stellar mass (see the bottom panel in Figure 3.7). The galaxies with higher stellar masses have more mature stellar populations and hence higher Balmer absorption equivalent widths.

In Figure 3.7, we show the stacks of SFR(Hα) in bins of stellar mass, corrected for the Balmer absorption in two different ways as well as the stacks without any corrections. The absorption correction affects both the value of the observed SFR(Hα) and the dust correction (i.e., the ratio of Hα to Hβ). We used the following correction method in this study. In each stellar mass bin, the Balmer absorption of individual galaxies inferred from the stellar population models were averaged, weighted by the inverse variance calculated from the errors in the individual Balmer emission line luminosities, and added to the stacked emission line luminosities. These are blue symbols in Figure 3.7.

On the other hand, as presented in Figure 3.7, not correcting for the Balmer absorption (green symbols) results in values that are inconsistent with the blue linear fit by as large as 9σ at $\log(M_*) \sim 10.6$. The absorption corrections reduce the inferred dust-corrected SFRs by values that are typically larger at larger masses. (Here, by factors of 1.3, 2.1, and 2.5 at the stellar masses of $\sim 10^{10.2}$, $10^{10.6}$, $10^{11.1}\,\mathrm{M}_\odot$.) As a result, the SFRs at higher masses are lower once the Balmer absorption correction is applied. In other words, not correcting for the underlying Balmer absorption results in higher SFRs at high masses and hence, a steeper slope.

In conclusion, we emphasize the importance of accounting for the Balmer absorption when using the Balmer emission lines to quantify the SFR-M_* relation. Using the

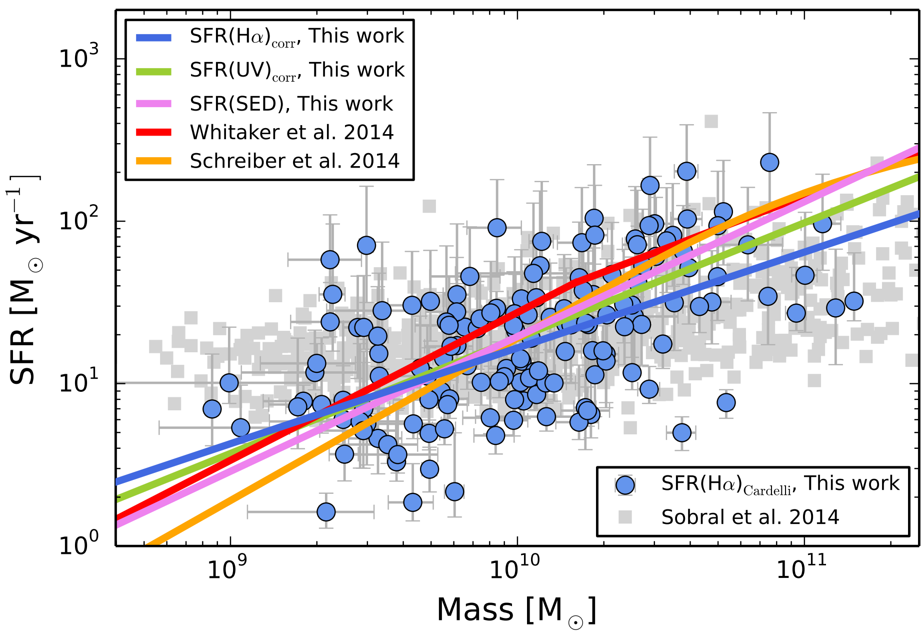

Figure 3.8 The comparison of SFR-M_* relation for various studies. The blue points and the blue line are our $z = 2.09 - 2.61$ results, using SFR(Hα) corrected for dust according to the Balmer decrement. The gray squares are from Sobral et al. (2014) narrow-band selected star-forming sample, where they used SFR(Hα) dust corrected based on the local mass-dependent correction relation of Garn & Best (2010). The Whitaker et al. (2014b) and Schreiber et al. (2015) relations are based on SFR(UV)+SFR(IR). We also plotted our results based on the SFR(UV) and SFR(SED) values. The relations from the literature are converted to a Chabrier IMF, when necessary.

Balmer lines that are not corrected for the underlying absorption results in higher SFR values, especially at the large masses where the Balmer absorption is stronger, and affects the parameterization of the SFR-M_* relation. The stacked points in bins of stellar mass, for which the weighted averaged Balmer absorption corrections are applied, are in the best agreement (within $\sim 1 - 2\sigma$) with the $\log(\text{SFR}) - \log(M_*)$ linear regression fitted to the individual galaxies (the blue line in Figure 3.7).

3.6 Comparison to Other Studies

The SFR-M_* relation has been studied extensively. The parameterization of the SFR-M_* relation depends on the SFR indicator and the typical timescale over which it traces star formation. First we consider studies that also use Hα to quantify SFRs and therefore provide the most direct comparison. Koyama et al. (2013), Sobral et al. (2014), and Darvish et al. (2014) used Hα narrow-band selected samples at $z \sim 2$. Such studies, however, tend to be biased towards galaxies with larger Hα equivalent widths. These three studies also did not measure Hβ, and relied on a mass-dependent dust correction from Garn & Best (2010). The Garn & Best (2010) relation was derived based on a local sample of galaxies but its validity has not been verified for $z \sim 2$ galaxies. The gray symbols in Figure 3.8 are the data points from Sobral et al. (2014). At the low mass end, $M_* \lesssim 10^{10}\,\mathrm{M}_\odot$, the high equivalent width bias mentioned above and the effect of the improper dust correction are evident. When we applied an average mass-dependent dust correction based on our Balmer decrement measurements to the Sobral et al. (2014) observed SFRs, we see a better agreement with our results at low masses. The Sobral et al. (2014) main sequence is tighter compared to ours, mainly because the scatter in the dust extinction–M_* relation is not taken into account.

Atek et al. (2014) is another Hα study, where they used *HST*/WFC3 near-IR grism spectroscopy for a sample of emission line galaxies at $0.3 \lesssim z \lesssim 2.5$. They used the H$\alpha$, H$\beta$, [OII]$\lambda$3727, and [OIII]$\lambda$5008 nebular emission lines as the SFR indicators, dust corrected in bins of stellar mass. The SFR-M_* slope they found was ~ 0.4 at $z \sim 2.3$, though they also identified a Malmquist bias as being a potential issue in their analysis.

We also considered main sequence studies where the total SFR was estimated as the sum of UV and IR-based SFRs, plotting the SFR-M_* relations of Whitaker et al. (2014b) and Schreiber et al. (2015) on top of our points in Figure 3.8. The SFR-M_* slopes of these studies are generally steeper than our slope. As we used the Balmer decrement to correct the observed SFR(Hα) for dust extinction, as opposed to using the IR data, it is probable that we missed optically thick star-forming regions, particularly in massive galaxies with high specific SFRs. This bias may be the reason of our shallower slope compared to the studies with the IR data. There are several important differences between the Whitaker et al. (2014b) and Schreiber et al. (2015) studies and ours, such as the samples, the SFR diagnostics, and the statistical methods used for the fit. At this point, it is not trivial to reconcile these discrepancies and discuss the agreement or disagreement between these studies and ours. A more informative comparison will become possible once we incorporate IR data into our analysis.

A few studies found indications of a non-linear SFR-M_* relation (e.g., Schreiber et al. 2015; Whitaker et al. 2014b; Lee et al. 2015). They suggested that the SFR-M_* slope flattens at high masses so that a single power law cannot explain the SFR-M_* relation. According to these studies, at higher redshifts the high-mass flattening becomes less prominent and at $z \sim 2$ the turning point shifts to $M_* \sim 10^{10.5}$. A turning point in the SFR-M_* relation is not obvious from the individual detections in our sample, nor from the stacks (Figure 3.2). However, because of the large uncertainty in the most massive stacked bin of our galaxies (see the blue and orange points in Figure 3.7), we can not confidently rule out the flattening at the high-mass end.

3.7 Conclusions and Discussion

As part of the MOSDEF survey, we used a sample of 185 star-forming galaxies with Hα and Hβ spectroscopy at $M_* > 10^{9.5}\,M_\odot$ to study the star-forming main sequence relation at $z \sim 2$. The parent catalog is H-band (i.e., rest-frame optically) selected and is accompanied by ancillary multi-band photometry (Skelton et al. 2014), from which the UV-based SFRs were measured. The stellar masses were derived by comparing the emission-line corrected photometric SEDs with stellar population models.

We found an intrinsic scatter of 0.36 dex in the SFR of the SFR(Hα)-M_* relation, which is larger than what we found based on the UV SFRs (see, Table 3.1). The larger scatter is expected as the Hα emission line, originating from ionized regions of the ISM, traces star formation activity on shorter timescales compared to the UV luminosity. As the Hα luminosity is a more instantaneous tracer of SFR, it provides a more accurate estimate of the scatter in SFR at a given stellar mass. Part of the difference between the SFR(Hα)-M_* scatter and that of the SFR(UV)-M_* may be related to the fact that the SFR(UV) and M_* are somewhat correlated; although our SFR(UV) values were calculated and dust corrected using the medium- and broad-band photometry directly, the UV slope still regulates the color-excess in the SED fitting from which the stellar masses were derived. The correlation between the estimates of SFR and stellar mass is even more significant when the SFR(UV) is corrected for extinction by $E(B-V)$ derived from the SED models, or when the SED-inferred SFRs are used.

The intrinsic scatter in the main-sequence relation measured here may be due to variables such as geometry, size, SFR surface density, metallicity, and age (e.g., Wuyts et al.

2013; Hemmati et al. 2014). The significance of the effect of these variables on the scatter will be investigated in future studies. Although in agreement with some simulations (Torrey et al. 2014; Sparre et al. 2015a), the scatter we found is larger than some of the other works (e.g., Dutton et al. 2010; Domínguez et al. 2015). The discrepancy may indicate that the galaxy accretion and feedback processes are not as smooth as predicted by the simulations. Our larger scatter can also be affected by galaxy-to-galaxy variations in the IMF and the dust corrections.

We found a constant slope of 0.59 ± 0.11 for the $z = 2.1 - 2.6$ sample and 0.65 ± 0.09 when we used the whole sample at $z = 1.4 - 2.6$, for $M_* \geq 10^{9.5}\,\mathrm{M}_\odot$. Galaxy evolution simulations generally find a close-to-unity slope for the SFR-M_* relation (e.g., Dutton et al. 2010; Torrey et al. 2014; Sparre et al. 2015a), which translates to a stellar mass-independent specific SFR (i.e., SFR/M_*). Our shallower slope indicates higher (lower) SFR at low (high) stellar masses. As the slope of the main sequence represents the star-formation efficiency, one explanation for close-to-unity slope in the galaxy simulations is that star formation is too inefficient at the low stellar-mass end due to feedback processes. The steep slope in the simulations may also be caused by a lack of quenching feedback that causes a dearth of red star-forming galaxies at the high-mass end of the SFR-M_* relation.

The slope of the main sequence is influenced by various observational and measurement effects that could explain discrepancies in the slopes reported in different observational studies. We demonstrated three of the main effects here: dust correction, sample biases, and stellar absorption correction (the last one is specific to the emission line studies). Correcting the Hα emission line with the SED inferred $E(B-V)_{\mathrm{SED}} \times 2.27$, with the assumption of the

Calzetti curve, leads to a SFR-M_* slope of close to unity. A bias against dusty galaxies with low specific SFRs, as might be the case for UV-selected samples, may also result in steeper slopes of the SFR-M_* relation. Finally, we showed that the Balmer absorption correction has a significant effect on the dust-corrected SFRs and not applying the correction to the Balmer emission lines could lead to an overestimation of the main-sequence slope.

The evolution of the slope, normalization, and the scatter of the SFR-M_* relation is essential to our understanding of the processes that govern galaxy growth during cosmic time. Once the whole MOSDEF sample becomes available, we have access to a large sample of rest-frame optical spectra for galaxies at $1.4 \lesssim z \lesssim 3.8$, which makes it possible to study the main-sequence evolution in redshift, using instantaneous and accurately-measured SFRs in a representative sample. Furthermore, incorporating IR data into our analysis will allow us for a more detailed comparison with the existing studies.

Funding for the MOSDEF survey is provided by NSF AAG grants AST-1312780, 1312547, 1312764, and 1313171 and grant AR-13907, provided by NASA through a grant from the Space Telescope Science Institute. The authors thank the MOSFIRE instrument team for building this powerful instrument, and for taking data for us during their commissioning runs. We are grateful to Marc Kassis at the Keck Observatory for his many valuable contributions to the execution of this survey. We also acknowledge the 3D-HST collaboration, who provided us with spectroscopic and photometric catalogs used to select MOSDEF targets and derive stellar population parameters. IS thanks Shoubaneh Hemmati for feedback on the manuscript. We thank James Aird for his help in matching AGN selection catalogs, and David Sobral for providing the HiZELS Hα catalog that was used as a comparison to our results. Support for IS is provided through the National Science Foundation Graduate Research Fellowship DGE-1326120. NAR is supported by an Alfred P. Sloan Research Fellowship. MK acknowledges support from the Hellman Fellows fund. ALC acknowledges funding from NSF CAREER grant AST-1055081. We wish to extend special thanks to those of Hawaiian ancestry on whose sacred mountain we are privileged to be guests. Without their generous hospitality, most of the observations presented herein would not have been possible. This work is also based on observations made with the NASA/ESA Hubble Space Telescope (programs 12177, 12328, 12060–12064, 12440–12445, 13056), which is operated by the Association of the Universities for Research in Astronomy, Inc., under NASA contract NAS 5-26555.

Chapter 4

The MOSDEF Survey: The strong agreement between Hα and panchromatic SED-based star formation rates*

Abstract We study the combined stellar and dust spectral energy distributions (SEDs) of 15 star-forming galaxies at $z \sim 2$ selected from the MOSFIRE Deep Evolution Field (MOSDEF) survey. All galaxies have 3σ detections for Hα and at least two IR bands (*Spitzer*/MIPS 24 μm and *Herschel*/PACS 100 and 160 μm, and in some cases *Herschel*/

*A version of this chapter was published in: Shivaei, I., Kriek, M., Reddy, N., Shapley, A., Barro, G., Conroy, C., Coil, A., Freeman, W., Mobasher, B., Siana, B., Sanders, R., Price, S., Azadi, M., Pasha, I., & Inami, H., *The Astrophysical Journal* 820, L23 (2016)

SPIRE 250, 350, and 500 μm). The galaxies have total IR ($8-1000\,\mu$m) luminosities of $\sim 10^{11.4}-10^{12.3}\,L_\odot$ and star-formation rates (SFRs) of $\sim 30-210\,M_\odot\,yr^{-1}$. We fit the panchromatic SEDs with the flexible stellar population synthesis (FSPS) models - which include both stellar and dust emission - and compare the inferred SFRs with the SFR(Hα) values corrected for dust attenuation using Balmer decrements. The two SFRs strongly agree with a scatter of 0.22 dex. Our results imply that the Balmer decrement accurately predicts the obscuration of the nebular lines and can be used to robustly calculate SFRs for star-forming galaxies at $z \sim 2$ with SFRs up to $\sim 200\,M_\odot\,yr^{-1}$. We also use our data to assess bolometric SFR indicators based on modeling the UV-to-mid-IR stellar and dust SEDs or by adding SFR(UV) and SFR(IR), for which the latter is based on the mid-IR only or on the full IR SED. All these SFRs show a poorer agreement with SFR(Hα) and in some cases large systematic biases are observed. Finally, we find that the SFR and dust attenuation derived from the UV-to-near-IR SED alone is unbiased when assuming a delayed exponentially declining star-formation history.

4.1 Introduction

The star-formation rate (SFR) and stellar mass (M_*) relation for star-forming galaxies (e.g., Noeske et al. 2007a; Rodighiero et al. 2014; Ilbert et al. 2015; Shivaei et al. 2015b) is important for understanding the physics of galaxy formation, as it provides direct constraints on star-formation efficiency and feedback processes (e.g., Torrey et al. 2014; Mitra et al. 2015). The shape and evolution of the SFR-M_* relation implies that more massive galaxies have higher SFRs (but lower specific SFRs) than less massive galaxies, and that at a fixed mass SFRs were higher at earlier times. However, the exact parameterization of the SFR-M_* relation (i.e., the slope, intercept, and scatter) depends significantly on our interpretation of the observations.

The stellar mass, commonly estimated from spectral energy distribution (SED) modeling (Conroy 2013; Mobasher et al. 2015), is built monotonically over a galaxys lifetime, and thus is a robust measurement. In contrast, SFR can be stochastic and its indicators are sensitive to different timescales as well as differing degrees of dust extinction (with the UV and optical light being most affected by dust). These factors make the derived SFR sensitive to the used diagnostic (Hayward et al. 2014; Domínguez et al. 2015; Shivaei et al. 2015a; Sparre et al. 2015b).

One of the commonly used diagnostics is the UV+IR SFR. Given the spatial resolution and sensitivity of current IR instruments, large samples of individual far-IR measurements at $z \sim 2$ are not feasible. Thus, instead, studies use empirical templates to convert mid-IR to total IR luminosity. However, recent results have shown that this method systematically overpredicts SFRs (e.g., Elbaz et al. 2011; Reddy et al. 2012a; Utomo et al. 2014).

The advent of multi-object near-IR spectrographs such as MOSFIRE (McLean et al. 2012) on Keck I and KMOS (Sharples et al. 2004) on the Very Large Telescope provides rest-frame optical spectra of large samples of high-redshift galaxies, and thus access to one of the most robust measures of the SFR: the Hα and Hβ emission lines. In Shivaei et al. (2015b) we showed that SFR(Hα) results in a shallower slope of the SFR-M_* relation compared to the slopes based on UV+IR SFRs (e.g., Whitaker et al. 2014b; Schreiber et al.

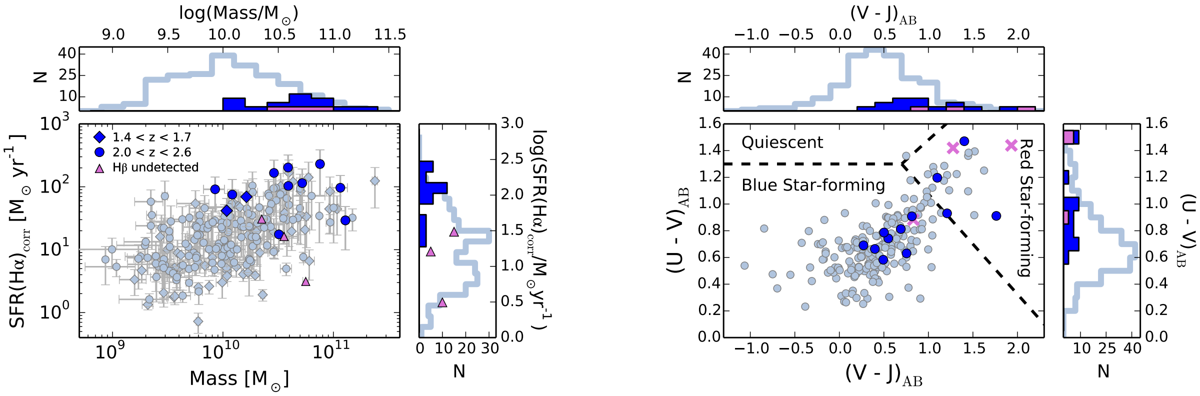

Figure 4.1 Dust-corrected SFR(Hα) vs. M_* (top) and rest-frame UVJ diagram (bottom) for the MOSDEF spectroscopic sample (light blue) and the 12 candidates in this study (dark blue). The three undetected-Hβ galaxies are the purple symbols with a 3σ lower-limit on their dust-corrected SFRs. For displaying purposes the number counts of the dark blue histograms are multiplied by 3.

2015). However, given that Balmer emission lines trace the instantaneous SFR and have been argued to miss optically thick star-forming regions (e.g., Rodighiero et al. 2014) it is essential to investigate how reliably Hα and Hβ trace total SFRs at high redshifts, and how the resulting SFRs compare to the previously discussed UV+IR SFRs.

Motivated by the concerns discussed above, we selected a sample of galaxies at $z \sim 2$ from the MOSFIRE Deep Evolution Field (MOSDEF) survey (Kriek et al. 2015) with detected Hα emission lines and *Spitzer* and *Herschel* IR photometry. We compared the UV-to-far-IR photometry of these galaxies with the state-of-the-art Flexible Stellar Population Synthesis (FSPS) models (Conroy et al. 2009), which use energy balance to fit the stellar and dust emission simultaneously. We investigated how well SFR(Hα) compares with the full SED-inferred SFR as well as SFR(UV) and SFR(IR). Throughout this paper, we assumed a Chabrier (2003) initial mass function (IMF) and a ΛCDM cosmology with $H_0 = 70\,\mathrm{km\,s^{-1}\,Mpc^{-1}}, \Omega_\Lambda = 0.7, \Omega_m = 0.3$.

4.2 Sample and Measurements

The MOSDEF survey is a multi-year project that uses the MOSFIRE near-IR spectrometer on the Keck I telescope to study the stellar and gaseous content of ~ 1500 galaxies and AGNs at $1.37 \leq z \leq 3.80$. The survey covers the CANDELS fields, for which extensive deep multi-wavelength data are available (Grogin et al. 2011; Koekemoer et al. 2011; Momcheva et al. 2016). For details of the survey strategy, observations, data reduction, and sample characteristics see Kriek et al. (2015). The current study is based on data from the first two years of the MOSDEF survey.

In this study we selected a sample of MOSDEF galaxies based on Balmer emission lines and IR measurements. The Hα and Hβ luminosities were estimated by fitting Gaussian functions to the line profiles. Line flux uncertainties were derived using Monte Carlo simulations. Hα and Hβ fluxes were corrected for underlying Balmer absorption as determined from UV-to-near-IR SED models (for details see Reddy et al. 2015). The Hα luminosity was converted to SFR using the Kennicutt (1998) relation and was corrected for dust attenuation using the Balmer decrement (Hα/Hβ), assuming the Cardelli et al. (1989) Galactic extinction curve.

For the IR measurements we used available data from *Spitzer*/MIPS and *Herschel*/PACS and SPIRE in the COSMOS, GOODS-N, and GOODS-S fields (Oliver et al. 2010; Elbaz et al. 2011; Lutz et al. 2011; Magnelli et al. 2013). As described below, we measured IR fluxes simultaneously using scaled point-spread functions (PSFs) (Reddy et al. 2010; Shivaei et al. 2015a) to recover fluxes of confused objects. For each image, we used a prior list of objects from higher resolution images to determine the location of all sources in the field. For the MIPS images we used IRAC sources detected at 3σ; for the PACS images we used the MIPS sources detected at 3σ; and for the SPIRE images we used the PACS sources detected at 3σ (for the 250 and 350 μm bands) and 5σ (for the 500 μm band). In order to perform the photometry, a subimage centered on each target was constructed and the PSF was fitted simultaneously to all the objects in the subimage (including the target) and one random background position, which was chosen to be at least 1 FWHM away from the sources. We repeated this procedure for 20 random background positions. The standard deviation of the background fluxes was adopted as the flux uncertainty.

The accuracy of our photometry was tested by simulating 500 sources with a large range of fluxes that were added to the original images. The simulated fluxes were recovered successfully with a given scatter that, as expected, decreased with increasing flux. On average, the ratio of the scatter to the flux error (estimated based on the background fluxes) was constant with flux. We multiplied the background-estimated flux errors of the individual targets by the average scatter-to-flux error ratios ($\sim 1.3 - 2.0$ depending on the filter and the field) to estimate the total uncertainty in the measured fluxes.

In order to obtain reliable SFR(Hα) and sample the dust emission properly, we selected galaxies that are not significantly affected by nearby sources and have signal-to-noise ratio (S/N) $> 3\sigma$ for the Hα, MIPS 24 μm, and at least one PACS filter (100 or 160 μm). The final sample consists of 12 galaxies with both Hα and Hβ detected and 3 Hβ-undetected galaxies. Only one galaxy has a robust detection in the SPIRE filters and for some of our galaxies even the PACS fluxes are marginally detected. We did not include objects that were classified as AGNs based on their X-ray emission, IRAC colors, or optical

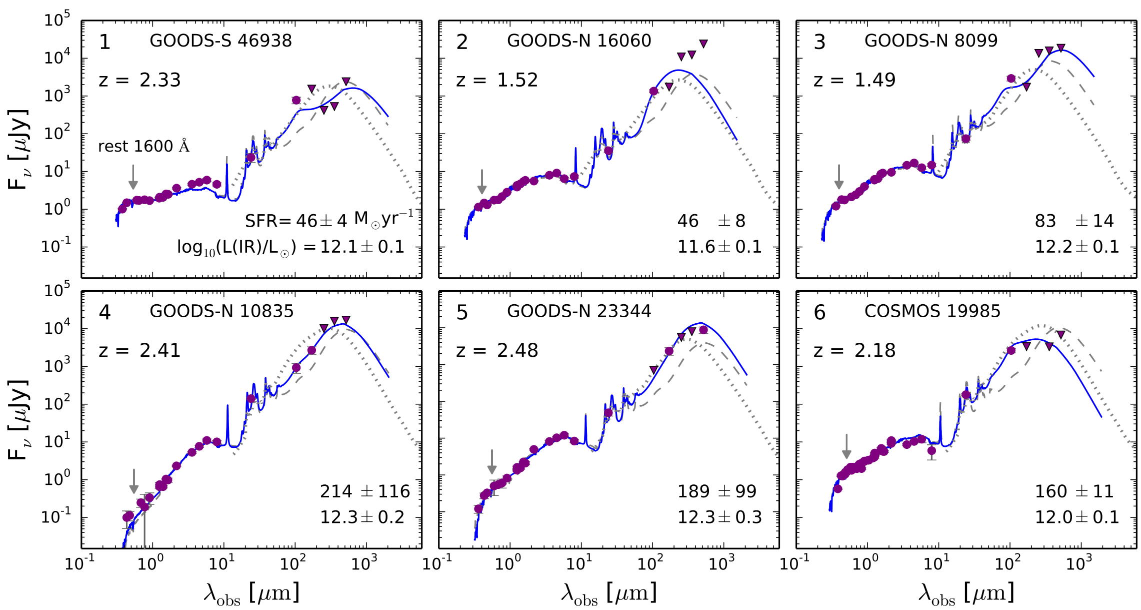

Figure 4.2 The best-fit panchromatic FSPS SED models (solid curves) to the observed photometry (purple symbols) of 6 of our Hα+Hβ-detected galaxies. The rest-frame optical emission lines are excluded from both the photometry and the models. The triangles show 3σ upper limits on the fluxes; in the fitting process, the actual photometry with the corresponding errors were used. The dashed and dotted lines represent the FSPS SED fits up to 24 μm and the Chary & Elbaz (2001) best-fit templates to the 24, 100, and 160 μm data, respectively. The ID numbers are from the 3DHST v4.1 photometric catalog. The galaxies are shown in order of increasing mass (continued in Figure 4.3).

emission lines (with the criterion of [NII]/Hα> 0.5, Coil et al. 2015). As seen in Figure 4.1, most candidates lie above the median SFR-M_* relation as modeled in Shivaei et al. (2015b) with $M_* \sim 10^{10} - 10^{11}\,\mathrm{M}_\odot$.

4.3 Panchromatic SED Modeling

In this section we derive bolometric SFRs by comparing the panchromatic SEDs - composed of the UV-to-IRAC photometry from 3D-HST (Skelton et al. 2014; Momcheva et al. 2016) combined with IR photometry (previous section) - with stellar population models. We generated composite stellar populations using the FSPS code (Conroy et al. 2009; Conroy & Gunn 2010, v2.5), assuming a Chabrier IMF and solar metallicity. For the star-formation history (SFH) we assumed a delayed-tau model of the form SFR(t) $\propto te^{-t/\tau}$, in which t is the age of the galaxy and τ is the e-folding time. τ was allowed to vary from $10^2 - 10^4$ Myr in steps of 0.2 dex. We set a 50 Myr lower limit on age corresponding to the typical dynamical timescale at $z \sim 2$ (Reddy et al. 2015). We adopted a Calzetti et al. (2000) attenuation curve, in which the dust optical depth at 5500 Å was allowed to vary from 0.0 to 4.0 in steps of 0.1. The dust emission in the FSPS code follows the Draine & Li (2007, DL07) models. In these dust models, the distribution of starlight intensities, U, is described by a delta function at U_{min} (the radiation intensity to which the dust in the diffuse ISM is exposed) and a power-law component for dust heated by more intense starlight. The parameter γ represents the fraction of dust heated by more intense starlight than in the diffuse ISM. As was suggested in DL07, we allowed U_{min} to vary between 0.1 to

25.0 in 10 logarithmic steps, the γ grid was set to $[0.0, 0.01, 0.02, 0.04, 0.06, 0.10, 0.15]$, and we explored PAH fractions of $0, 1, 2, 3, 5, 7, 10\%$.

We shifted the models to the spectroscopic redshift of each galaxy, applied the Madau (1995) prescription to correct the SEDs for the intergalactic medium absorption, and then, using a χ^2 minimization fitting procedure, fit the models to the UV-to-far-IR photometry. The optical photometry was corrected for contamination by bright emission lines (Hα, [O III], [O II], etc.) as measured from the MOSDEF spectra (Reddy et al. 2015). We perturbed the photometry according to the measurement uncertainties for 100 realizations and the dispersion in each best-fit parameter was adopted as the associated uncertainty.

The best-fit models of the 12 Hα+Hβ-detected candidates are displayed in Figures 4.2 and 4.3. We would have found similar SFRs if instead we modeled the IR emission by a single blackbody SED. In order to make sure that our best-fit models are not skewed by the smaller relative errors of the 24 μm data compared to the PACS errors, we tested the SED fitting with equal weighting for the 24, 100, and 160 μm fluxes. For all but two galaxies (galaxies 1 and 12), the corresponding SFRs and IR luminosities were within 1σ uncertainty of the original SFR and L(IR) values.

4.4 SFR Comparison

In this section we investigate how the SFRs derived using different indicators compare with each other. Fitting the stellar and dust SEDs simultaneously using energy balance techniques is thought to give a robust estimate of the total SFR. Figure 4.4(a)

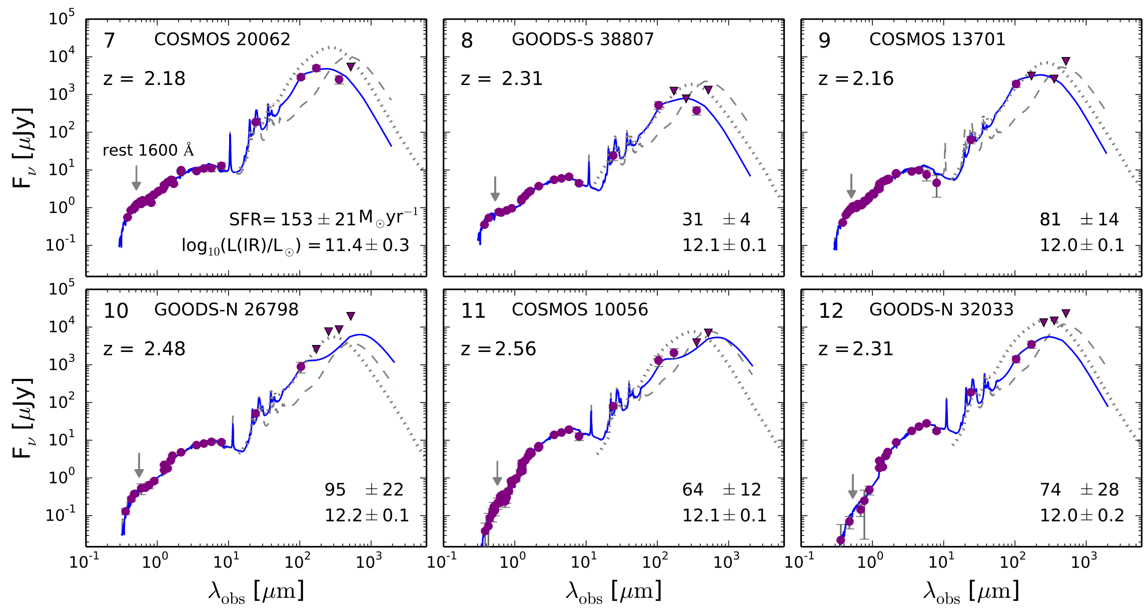

Figure 4.3 The best-fit SED models of the rest of our Hα-Hβ-detected sample. See the caption of Figure 4.2.

shows that dust-corrected SFRs(Hα) are in good agreement with the full SED-inferred SFRs ($\mathrm{SFR_{full\,SED}}$). The tight correlation (0.22 dex scatter, Spearman $\rho_{\rm s} = 0.69$ with 2.3σ away from a null correlation) with an average SFR(Hα)-to-$\mathrm{SFR_{full\,SED}}$ ratio of 1.04 and absence of any systematic correlation as a function of M_* (see the inset plot 4.4(a)), implies that the dust-corrected Hα luminosity is an unbiased tracer of the bolometric SFR for star-forming galaxies with SFRs $\sim 100\, M_{\odot}\,\mathrm{yr}^{-1}$.

There is a systematic uncertainty associated to our choice of the attenuation curve. Assuming the Calzetti curve instead of the Cardelli curve to correct the observed Hα predicts higher SFRs by an average factor of 1.2 (as high as 1.4 for the galaxy with the highest SFR). The larger dust correction is expected as the Calzetti curve has a higher normalization at 6563 Å. We adopted the Cardelli curve as it was derived based on the line-of-sight mea-

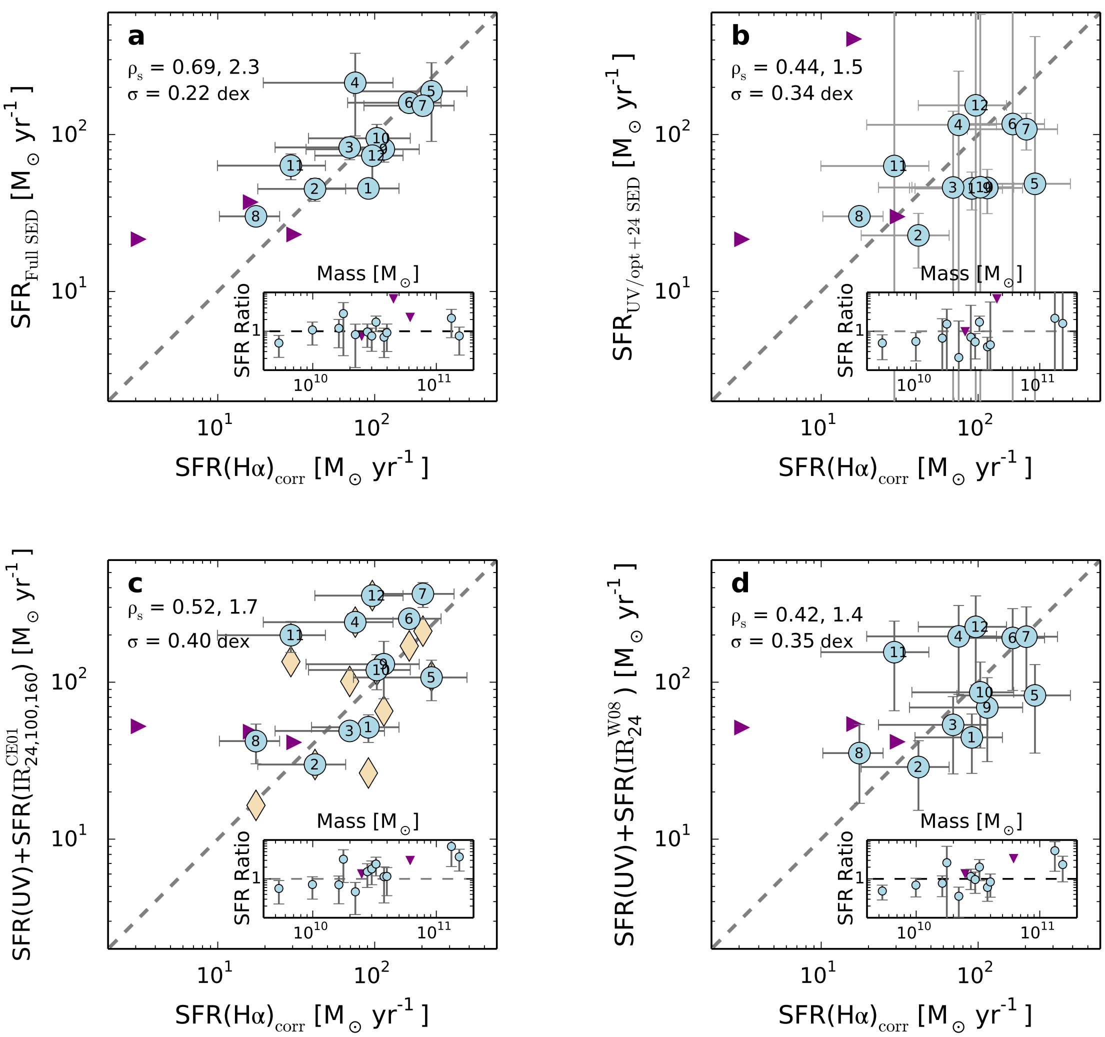

Figure 4.4 SFR comparisons for the 12 galaxies with both Hα and Hβ detections (circles) and the 3 Hβ-undetected galaxies (triangles). In all plots, the horizontal axis is the dust-corrected SFR(Hα) and the dashed lines denote one-to-one relationships. The vertical axis is the SFR derived from modeling the UV-to-far-IR photometry (a), the UV-to-mid-IR photometry (b), and SFR(UV)+SFR(IR), in which SFR(IR) is derived from the $24-160\,\mu$m (c, circles) and $24-500\,\mu$m (c, diamonds) or $24\,\mu$m only photometry (d), using the CE01 and W08 templates, respectively. Each subplot shows the ratio of the SFR(Hα) to the SFR in the main plot's vertical axis as a function of M_*. The masses are inferred from the best-fit SEDs. The Spearman coefficient (ρ_s), its significance, and scatter about unity line (σ) are listed in the plots. The galaxies' numbers correspond to the SEDs in Figures 4.2,4.3.

surements of molecular clouds and HII regions, and therefore preferable for the extinction correction of nebular lines.

Given that the majority of the MOSDEF galaxies are not detected with *Herschel*, it is important to know how well we can recover the total SFR with only 24 μm data. We fit the FSPS models to the UV-to-24 μm data and set the dust emission parameters to the default values (PAH fraction = 3.5%, $\gamma = 0.01$, and $U_{\rm min} = 1.0$). The result is shown in Figure 4.4(b). The $\rm SFR_{UV-24}$ and SFR(Hα) show no systematic offset, but exhibit a larger scatter of 0.34 dex.

In panels c and d of Figure 4.4 we estimated the bolometric SFR by adding unobscured SFR(UV) to obscured SFR(IR). The SFR(UV) is derived from the 1600 Å luminosity by fitting a power-law function of the form $f_\lambda \propto \lambda^\beta$ to the photometry at rest wavelengths 1268 − 2580 Å, and using the Kennicutt (1998) conversion between L(UV) and SFR. In order to estimate the total L(IR), we fit the locally calibrated Chary & Elbaz (2001) templates (hereafter, CE01) to the 24, 100, and 160 μm fluxes in Figure 4.4(c), and in Figure 4.4(d) we converted the 24 μm to total L(IR) using the luminosity-independent conversions of Wuyts et al. (2008) (hereafter, W08).

The relation between SFR(Hα) and CE01 SFR is tighter than that of SFR(Hα) vs. W08 SFR, but the CE01 SFR is significantly larger than SFR(Hα) for several galaxies. Even when incorporating the SPIRE photometry and fitting the CE01 templates to all the available IR photometry, the SFR(Hα) and SFR(UV)+SFR(IR) correlation is weak ($\rho_{\rm s} = 0.38$ with 1.3σ), although the offset disappears (diamonds in Figure 4.4(c)). Whether the discrepancy is due to the limited parameter space of the CE01 templates or because of ignoring energy balance is an open question that cannot be addressed with the limited data used in this study.

Moreover, we tested the Kennicutt et al. (2009) empirically-derived coefficients to infer total SFRs by combining observed Hα and IR luminosities. The combined SFRs were systematically lower than our dust-corrected SFR(Hα) and $\mathrm{SFR_{full-SED}}$ by ~ 0.1 dex, which might be because of the lower L(IR) and SFRs of the Kennicutt et al. (2009) nearby sample compared to our $z \sim 2$ sample.

Our sample contained 3 galaxies without Hβ detections, for which we determined 3σ lower limits on the SFR(Hα). The low $\mathrm{SFR_{full\,SED}}$ of the Hβ-undetected galaxies compared to the rest of the sample indicates that we are not biased against galaxies in which Hβ is suppressed by dust attenuation. The Hβ line in all three galaxies happened to fall close to a bright skyline, which likely explains their low S/N in Hβ.

4.5 IR Luminosity Comparison

One concern regarding the use of energy-balance SED modeling is that for a galaxy with two distinct stellar populations, with one enshrouded by dust, and hence, bright in IR, and the other population less dusty and brighter in UV, the IR and UV-to-near-IR parts of the spectrum will be decoupled. For such cases, an energy-balance method would underestimate the true SFR and L(IR). To address this issue, we calculated L(IR) based on the dust obscuration parameter derived from the UV-to-near-IR SED and compared it to the observed $0.3 - 8\mu$m photometry (using the same stellar population models and fitting assumptions as for the full modeling, see Section 4.3). We used the estimated total

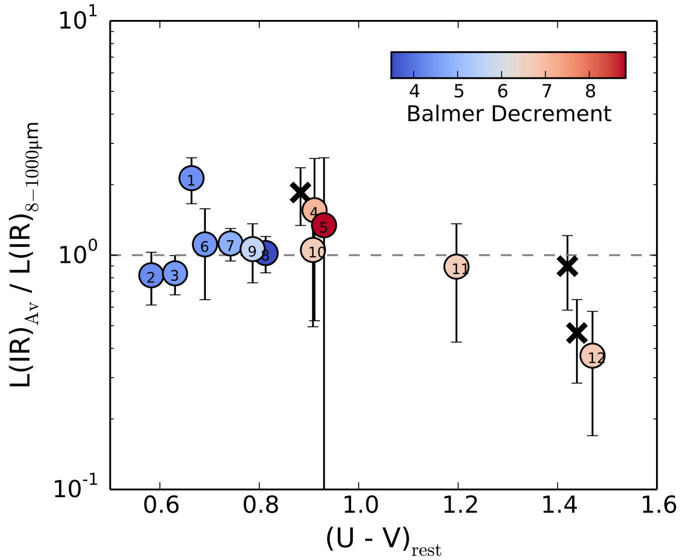

Figure 4.5 Ratio of the predicted ($L(IR)_{Av}$, based on UV-to-near-IR SED) to the measured ($L(IR)_{8-1000\mu m}$) IR luminosities as a function of rest-frame $U-V$ color. The good agreement between the two estimated IR luminosities suggests that there is not a dominant obscured stellar population that is missing from the UV-to-near-IR SED. Galaxies with undetected Hβ are shown with crosses. Numbers correspond to the SEDs in Figures 4.2,4.3.

extinction value at 1600 Å (A_{1600}) and unobscured SFR(UV) measured from the luminosity at 1600 Å, to calculate the *obscured* SFR:

$$\mathrm{SFR_{obscured}} = \mathrm{SFR(UV)}\ (10^{0.4A_{1600}} - 1.0). \tag{4.1}$$

Using the Kennicutt (1998) relation, we converted the obscured SFR to total L(IR) at 8−1000 μm and compared it to the L(IR) based on our best-fit full SED model, integrated from 8 to 1000 μm. The results are shown in Figure 4.5. For all galaxies in our sample, the UV-to-near-IR SED-derived L(IR) is within a factor of ~ 2 of the integrated full SED L(IR), suggesting that there is not a dominant stellar population that is completely obscured and thus missed from the UV-to-near-IR SED.

The results of the UV-to-near-IR SED-inferred IR luminosities are sensitive to the assumed SFH and the SED-predicted ages. If instead of a delayed-tau SFHs we use a rising SFH of the form $\mathrm{SFR}(t) \propto e^{t/\tau}$, the best-fit SED model predicts a high amount of dust obscuration for our two most massive galaxies (objects 11 and 12). Because of the high dust obscuration inferred from the stellar SED, L(IR) and SFR are overpredicted by a factor of $\gtrsim 2$. Additionally, as found in previous studies (e.g., Wuyts et al. 2011a), without a minimum age of 50 Myr the best-fit UV-to-near-IR SEDs result in unrealistically young ages and high dust values for a subset of our galaxies.

With a physically reasonable age range and the delayed-tau SFHs, the UV-to-near-IR SED and full SED SFRs are in good agreement ($\rho_\mathrm{s} = 0.90$, 3.0σ away from a zero correlation). This test illustrates that the SFR derived from the stellar emission alone is not biased compared to the panchromatic SED-based SFR for $z \sim 2$ galaxies with $\mathrm{M}_* \sim 10^{10} - 10^{11}\,\mathrm{M}_\odot$ and $\mathrm{SFR} \sim 30 - 210\,\mathrm{M}_\odot\,\mathrm{yr}^{-1}$.

4.6 Discussion and Implications

UV-inferred SFRs are susceptible to missing or underestimating the SFR of galaxies for which the bulk of the star formation is obscured and the UV slope is decoupled from the total obscuration. Although Hα is less affected by dust extinction than the UV, given its longer wavelength, it is still a valid concern that Hα studies may also underestimate the SFR in dusty star-forming galaxies. We show in this paper that for Hα-based studies with SFRs $\sim 30 - 210\,\mathrm{M}_\odot\,\mathrm{yr}^{-1}$ the Hα luminosity does not underestimate the SFR, once Hα is properly corrected for dust attenuation using the Balmer decrement. This conclusion does not necessarily hold at higher SFRs (i.e., submillimeter galaxies) owing to highly obscured nebular regions. Such IR-luminous galaxies are likely missed in our study due to their low number density or highly obscured emission lines. To test the latter, we checked the MOSDEF target sample for galaxies with IR detections and undetected Hα lines, and found two. Due to uncertain redshifts and noisy spectra we did not include them in this study. However, deeper and/or wider wavelength range spectra are needed to confirm these systems.

There are additional caveats to our analysis which need to be explored in more detail in future studies. First, both the SFR(Hα) and the $\mathrm{SFR}_{\mathrm{full-SED}}$ suffer from systematic uncertainties in the assumed IMF, metallicity, and SFH. Second, the SFR(Hα) is affected by the choice of the assumed dust attenuation curve (Section 4.4), and the $\mathrm{SFR}_{\mathrm{full\,SED}}$ by the assumed dust emission models. Using stacking techniques for the IR data and incorporating the full MOSDEF sample, once available, we will build upon the results of this study. Furthermore, given the large discrepancies among different dust models at wavelengths $> 1\,\mathrm{mm}$ (as demonstrated in Figures 4.2 and 4.3), mapping the Rayleigh-Jeans tail of the cold dust emission with new facilities like the Atacama Large Millimeter/submillimeter Array (ALMA) will significantly improve our understanding of the dust properties at high redshift.

I.S. thanks Mostafa Khezri and Ali Khostovan for useful discussions and feedback on the manuscript. I.S. and N.A.R are supported by a National Science Foundation Graduate Research Fellowship DGE-1326120 and an Alfred P. Sloan Research Fellowship, respectively.

The MOSDEF survey is funded by NSF AAG collaborative grants AST-1312780, 1312547, 1312764, and 1313171 and archival grant AR-13907, provided by NASA through a grant from the Space Telescope Science Institute. This work is based on observations made with the W.M. Keck Observatory, which is operated as a scientific partnership among the California Institute of Technology, the University of California, and the National Aeronautics and Space Administration.

Chapter 5

The MOSDEF Survey: Metallicity Dependence of PAH Emission at High Redshift and Implications for 24μm-inferred IR Luminosities and Star Formation Rates at $z \sim 2$*

Abstract We present results on the variation of 7.7 μm Polycyclic Aromatic Hydrocarbon (PAH) emission in galaxies spanning a wide range in metallicity at $z \sim 2$. For this analysis,

*A version of this chapter was published in: Shivaei, I., Reddy, N., Shapley, A., Siana, B., Kriek, M., Mobasher, B., Coil, A., Freeman, W., Sanders, R., Price, S., Azadi, M., Zick, T., *The Astrophysical Journal* 837, 157 (2017)

we use rest-frame optical spectra of 476 galaxies at $1.37 \leq z \leq 2.61$ from the MOSFIRE Deep Evolution Field (MOSDEF) survey to infer metallicities and ionization states. *Spitzer*/MIPS 24μm and *Herschel*/PACS 100 and 160 μm observations are used to derive rest-frame 7.7 μm luminosities ($L_{7.7}$) and total IR luminosities ($L_{\rm IR}$), respectively. We find significant trends between the ratio of $L_{7.7}$ to $L_{\rm IR}$ (and to dust-corrected SFR) and both metallicity and [OIII]/[OII] (O_{32}) emission-line ratio. The latter is an empirical proxy for the ionization parameter. These trends indicate a paucity of PAH emission in low metallicity environments with harder and more intense radiation fields. Additionally, $L_{7.7}/L_{\rm IR}$ is significantly lower in the youngest quartile of our sample (ages of $\lesssim 500\,$Myr) compared to older galaxies, which may be a result of the delayed production of PAHs by AGB stars. The relative strength of $L_{7.7}$ to $L_{\rm IR}$ is also lower by a factor of ~ 2 for galaxies with masses $M_* < 10^{10}\,{\rm M}_\odot$, compared to the more massive ones. We demonstrate that commonly-used conversions of $L_{7.7}$ (or 24 μm flux density; f_{24}) to $L_{\rm IR}$ underestimate the IR luminosity by more than a factor of 2 at $M_* \sim 10^{9.6-10.0}\,{\rm M}_\odot$. We adopt a mass-dependent conversion of $L_{7.7}$ to $L_{\rm IR}$ with $L_{7.7}/L_{\rm IR}$= 0.09 and 0.22 for $M_* \leq 10^{10}$ and $> 10^{10}\,{\rm M}_\odot$, respectively. Based on the new scaling, the SFR-M_* relation has a shallower slope than previously derived. Our results also suggest a higher IR luminosity density at $z \sim 2$ than previously measured, corresponding to a $\sim 30\%$ increase in the SFR density.

5.1 Introduction

Emission from single-photon, stochastically-heated Polycyclic Aromatic Hydrocarbon (PAH) molecules dominates the mid-infrared (mid-IR) spectra of star-forming galaxies.

The origin and properties of these molecules have been the subject of many studies in the literature, most of which have focused on local galaxies (Tielens 2008, and references therin).

It is crucial to fully understand how PAH emission depends on the physical conditions of the interstellar media (ISM) as the PAH emission contribution to total IR emission of galaxy may vary significantly from ~ 1 to 20% in different environments (Smith et al. 2007; Dale et al. 2009, among many others). There is evidence that PAHs are less abundant in metal-poor environments in the local universe (e.g., Normand et al. 1995; Calzetti et al. 2007; Draine et al. 2007b; Smith et al. 2007; Engelbracht et al. 2005; Hunt et al. 2010; Cook et al. 2014). The physical explanation of this observation is a subject of much debate – whether the decrease in the PAH emission at low metallicity is directly driven by metallicity or some other property of such environments is still unknown. The most favored explanation is destruction of PAH molecules by hard UV radiation in low-metallicity environments due to reduced shielding by dust grains (e.g., Voit 1992; Madden et al. 2006; Hunt et al. 2010; Sales et al. 2010; **?**; Magdis et al. 2013). Other possibilities have also been discussed in the literature: that small PAH carriers are destroyed in low-metallicity environments through sputtering (Hunt et al. 2011, and references therein), that PAH formation and destruction mechanisms depend on dust masses, which in turn correlate with metallicity (Seok et al. 2014); and that the PAH-metallicity trend is a consequence of the PAH-age correlation (Galliano et al. 2008). The latter scenario is offered based on the assumption that the contribution of AGB stars – as the purported primary origin of PAH molecules – to ISM chemical enrichment increases with age.

The PAH emission features span from 3 μm to 17 μm, with the one at 7.7μm being the strongest (contributing $\sim$ 40–50% of the total PAH luminosity; Tielens 2008; Hunt et al. 2010). At $z \sim 2$, the 24 μm filter of the *Spitzer*/MIPS instrument traces this feature. Due to the high sensitivity of MIPS, many high-redshift studies adopt the 24 μm flux as an indicator of total IR luminosity ($L(8-1000\mu\text{m}) \equiv L_{\text{IR}}$) and star-formation rate (SFRs; e.g., Chary & Elbaz 2001; Reddy et al. 2006a; Daddi et al. 2007a; Wuyts et al. 2008; Reddy et al. 2010; Shivaei et al. 2015a). However, the metallicity and ionization state dependence of the PAH-to-L_{IR} ratio of distant galaxies have not been studied in detail. In high-redshift studies, a single conversion from 24 μm flux (or rest-8 μm luminosity) to L_{IR} is typically assumed for galaxies with a range of different metallicities and stellar masses (e.g., Wuyts et al. 2008, 2011a; Elbaz et al. 2011; Reddy et al. 2012b; Whitaker et al. 2014b). Possible variations of the relative strength of PAH emission to L_{IR} with metallicity (and as a consequence with stellar mass) can potentially alter the results of studies that rely on 24 μm flux to infer L_{IR} or SFR – for example, those that investigate dust attenuation parameterized by $L_{\text{IR}}/L_{\text{UV}}$ (e.g., Reddy et al. 2012b; Whitaker et al. 2014b), or those that utilize bolometric SFRs (i.e., $\text{SFR}_{\text{IR}}+\text{SFR}_{\text{UV}}$) to explore relations such as the SFR-M_* relation (e.g., Daddi et al. 2007a; Wuyts et al. 2011b; Fumagalli et al. 2014; Tomczak et al. 2016).

With the large and representative dataset of the MOSFIRE Deep Evolution Field (MOSDEF) survey (Kriek et al. 2015), we are in a unique position to investigate, for the first time, the dependence of PAH intensity (defined as the ratio of 7.7 μm luminosity to SFR or L_{IR}) on the ISM properties of high-redshift galaxies. The MOSDEF survey provides us with near-IR spectra of galaxies at $1.37 \leq z \leq 2.61$, from which we calculate spectroscopic redshifts and estimate gas-phase metallicities and ionization states. We use mid- and far-IR photometric data from *Spitzer*/MIPS 24 μm and *Herschel*/PACS 100 and 160 μm to measure PAH emission and total IR luminosities, respectively.

Our study includes galaxies over a broad range of stellar masses ($M_* \sim 10^9 - 10^{11.5}\,\mathrm{M}_\odot$), SFRs ($\sim 1 - 200\,M_\odot\,\mathrm{yr}^{-1}$), and metallicities ($\sim 0.2 - 1\,Z_\odot$). Ultimately, we quantify how the conversions between rest-frame 7.7 μm and both SFR and L_{IR} depend on metallicity and stellar mass. These scaling relations are important for deriving unbiased estimates of total IR luminosities and obscured SFRs based on observations of the PAH emission in distant galaxies – such observations will be possible for larger numbers of high-redshift galaxies with *JWST*/MIRI (Shipley et al. 2016).

The outline of this paper is as follows. In Section 5.2, we introduce the MOSDEF survey and describe our measurements including line fluxes, stellar masses, SFRs, IR photometry, and the IR stacking method. In Section 5.3, we constrain the dependence of $L_{7.7}$/SFR and $L_{7.7}/L_{\mathrm{IR}}$ on metallicity and ionization state. The PAH intensity as a function of age is explored in Section 5.4. Implications of our results for the studies of the SFR-M_* relation and the IR luminosity density at $z \sim 2$ are discussed in Section 5.5. In Section 5.6, we briefly discuss the possible physical mechanisms driving the PAH-metallicity correlation. Finally, the results are summarized in Section 5.7. Throughout this paper, line wavelengths are in vacuum and we assume a Chabrier (2003) initial mass function (IMF). A cosmology with $H_0 = 70\,\mathrm{km\,s^{-1}\,Mpc^{-1}}, \Omega_\Lambda = 0.7, \Omega_\mathrm{m} = 0.3$ is adopted.

5.2 Data

5.2.1 The MOSDEF Survey

During the MOSDEF survey, we obtained rest-frame optical spectra of ~ 1500 galaxies with the MOSFIRE spectrograph on the Keck I telescope (McLean et al. 2012). The parent sample was selected based on H-band magnitude in three redshift ranges: $z = 1.37 - 1.70$, $2.09 - 2.61$, and $2.95 - 3.80$, down to $H = 24.0$, 24.5, and 25.0 mag, respectively. These redshift ranges were adopted to ensure coverage of the strong optical emission lines ([OII], [OIII], Hβ, Hα) in the JHK bands. The MOSDEF survey was conducted in the five CANDELS fields: AEGIS, COSMOS, GOODS-N, GOODS-S, and UDS (Grogin et al. 2011; Koekemoer et al. 2011). These fields are also covered by the HST/WFC3 grism observations of the 3D-HST survey (Skelton et al. 2014; Momcheva et al. 2016). The details of the MOSDEF survey, observing strategy, and data reduction are reported in Kriek et al. (2015).

We limit our study to the first two redshift bins ($1.37 \leq z \leq 1.70$ and $2.09 \leq z \leq 2.61$), where the MIPS 24 μm filter covers the rest-frame 7.7 μm PAH feature (Figure 5.1). Objects with active galactic nucleus (AGN) contamination are removed from our study, based on their X-ray emission, IRAC colors (using the Donley et al. 2012 criteria), and/or [NII]/Hα line ratios ([NII]/H$\alpha > 0.5$; Coil et al. 2015; Azadi et al. 2017).

5.2.2 Emission Line Measurements

Emission line fluxes were estimated by fitting Gaussian functions to the line profiles. Uncertainties in the line fluxes were derived by perturbing the spectrum of each object

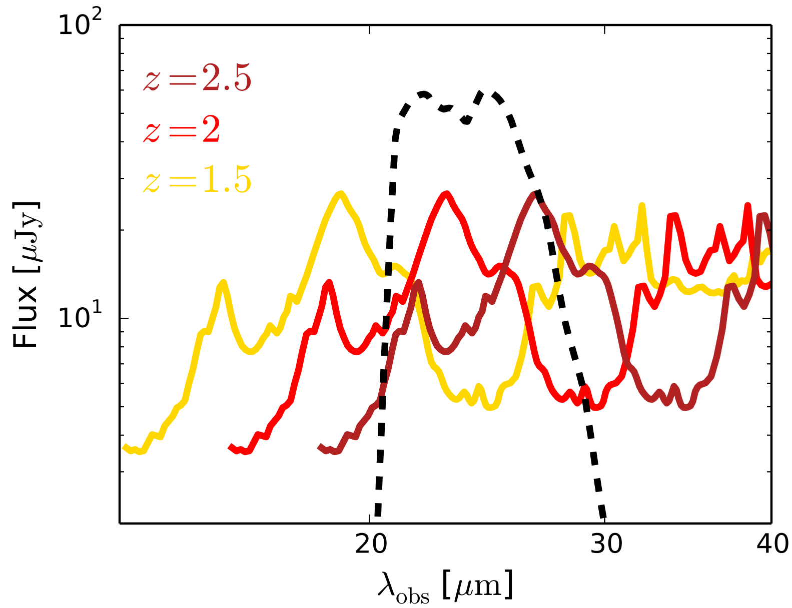

Figure 5.1 The *Spitzer*/MIPS 24μm filter (black dashed line) superimposed on the observed mid-IR spectrum of a galaxy at $z = 1.5$ (yellow), $z = 2$ (light red), and $z = 2.5$ (dark red). The mid-IR spectrum is adopted from Rieke et al. (2009) for a galaxy with $L_{\rm IR} = 10^{11}{\rm L}_{\odot}$.

according to its error spectrum and measuring the line fluxes in these perturbed spectra (see Kriek et al. 2015; Reddy et al. 2015). The Hα line and [NII] doublet were fit with three Gaussian functions and the [OII] doublet was fit with two Gaussians. To account for the loss of flux outside of the spectroscopic slits, corrections were applied by normalizing the spectrum of a slit star in each observing mask to match the 3D-HST total photometric flux (Skelton et al. 2014). Additionally, we used the *HST* images of our resolved galaxy targets to estimate and correct for differential flux loss relative to that of the slit star (Kriek et al. 2015). Hα and Hβ fluxes were further corrected for underlying Balmer absorption as determined from the best-fit stellar population models to the broadband photometry (Section 5.2.3).

We use the [NII]λ6585/Hα (N2) and ([OIII]λ5008/Hβ)/([NII]λ6585/Hα) (O3N2) indicators to derive gas-phase oxygen abundances (metallicities) based on the empirical calibrations of Pettini & Pagel (2004) (see Sanders et al. 2015; Shapley et al. 2015). As both N2 and O3N2 indicators include ratios of emission lines that are close in wavelength space, no dust correction is applied. Although there are concerns regarding biases in the metallicity indicators that use nitrogen (Shapley et al. 2015; Sanders et al. 2016a), the N2 and O3N2 indicators still distinguish the lower- and higher-metallicity galaxies, which is sufficient for the purpose of this study. Furthermore, we use the [OIII]$\lambda\lambda$4960, 5008/[OII]$\lambda\lambda$3727, 3730 ratio (O_{32}) as a proxy for ionization parameter. As [OIII]λ5008 has a higher signal-to-noise (S/N) than [OIII]λ4960, we assume a fixed [OIII]λ5008/[OIII]λ4960 line ratio of 2.98 (Storey & Zeippen 2000) to calculate the sum of [OIII]λ5008 and [OIII]λ4960. We correct [OIII] and [OII] lines for dust extinction by using the Balmer decrement (Hα/Hβ) and assuming the Cardelli et al. (1989) extinction curve (Reddy et al. 2015; Shivaei et al. 2016). Where necessary, we calculate O_{32} gas-phase metallicity based on the calibrations of Jones et al. 2015.

5.2.3 Stellar Masses, Ages, and SFRs

Stellar masses and ages are derived by fitting rest-UV to near-IR photometry from 3D-HST (Skelton et al. 2014; Momcheva et al. 2016) with Bruzual & Charlot (2003) models through a minimum χ^2 method. The photometry is corrected for emission line contamination according to the MOSDEF spectra. For the SED fitting we assume a solar metallicity, a Chabrier (2003) IMF, and an exponentially rising star-formation history (Reddy et al. 2015). The latter is assumed because it has been shown that rising star formation histories

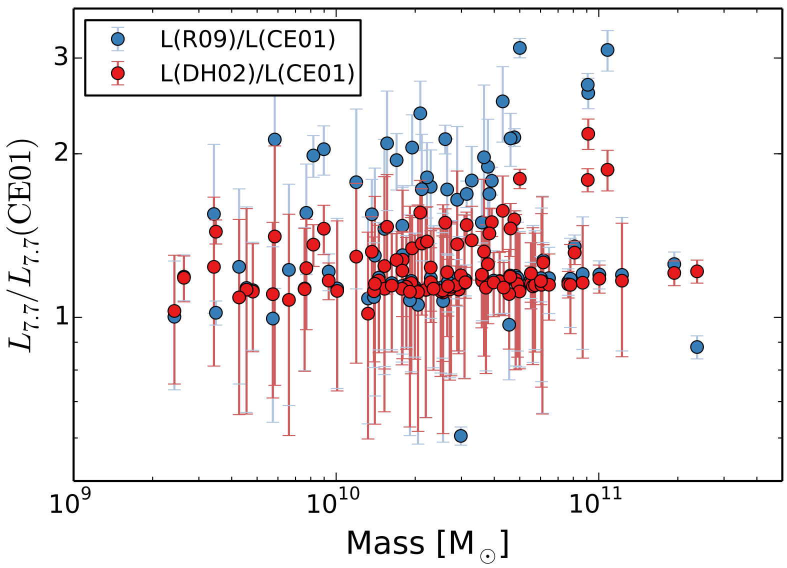

Figure 5.2 Ratio of the rest-frame 7.7 μm luminosities inferred from the IR templates of Dale & Helou (2002, red) and Rieke et al. (2009, blue) to those inferred from the Chary & Elbaz (2001) templates for 299 galaxies with robust redshifts. The 7.7 μm luminosities are derived by fitting 24 μm flux densities to the IR templates. For a majority of galaxies, the systematic bias caused by using different templates is not significant compared to the measurement uncertainties.

best reproduce the observed SFRs at $z \sim 2$ (e.g., Wuyts et al. 2011a; Reddy et al. 2012b). As described in Reddy et al. (2012b), ages that are inferred from exponentially rising star formation histories are ambiguous and often larger than those derived from constant star formation histories. However, a majority (86%) of our galaxies have very large characteristic timescales ($\tau = 5000$ Myr), which makes their star formation histories very similar to a constant one, along with well-defined ages.

We convert Hα luminosities to SFRs by adopting the Kennicutt (1998) relation, modified for the Chabrier 2003 IMF. The line luminosities are corrected for dust attenuation using the Balmer decrement and assuming the Cardelli et al. (1989) curve (Shivaei et al. 2016). Hereafter, we refer to the dust-corrected Hα SFR as $\mathrm{SFR}_{\mathrm{H}\alpha,\mathrm{H}\beta}$.

5.2.4 Mid- and Far-IR fluxes

We perform scaled point-spread function (PSF) photometry on the *Spitzer*/MIPS and *Herschel*/PACS images in COSMOS, GOODS-N, GOODS-S, and AEGIS fields from multiple observing programs (PI: M. Dickinson; Dickinson & FIDEL Team 2007; Elbaz et al. 2011; Magnelli et al. 2013). The accuracy of the measured fluxes is determined by adding simulated sources to the science images and recovering their fluxes in the same way as for real sources. Details of the photometry and simulations are described in Shivaei et al. (2016). In brief, we use the IRAC and MIPS priors down to a 3σ limit for MIPS and PACS images, respectively. A 40 by 40 pixel subimage is made around each target. In each subimage, the PSFs are scaled to match the prior objects and the target simultaneously. In this process, a covariance matrix is defined to determine the robustness of the fit, which is affected by confusion with nearby sources as described in Reddy et al. (2010). Based on the total covariance value of the MIPS $24\,\mu$m fits, we remove objects that have nearby companions from our analysis. To determine the noise and background level in each subimage, we fit PSFs to 20 random positions, ensuring that these positions are more than 1 FWHM away from any real sources. The average and standard deviation of the background fluxes are adopted as the background level and noise in the image, respectively. The typical measurement uncertainty for $24\,\mu$m-detected objects is $\sigma_{24} \sim 15\%$. The majority ($\sim 80\%$) of these $24\,\mu$m-detected objects are not detected in 100 and $160\,\mu$m images. Out of 406 non-AGN objects without any nearby sources (see above), 128 of them (32%) are detected at $24\,\mu$m with $S/N > 3$, and only 13 (3%) are detected with $S/N > 3$ at both 24 and $100\,\mu$m.

5.2.5 IR Stacks

Due to the relatively shallow depth of the available far-IR data, we stack the PACS images to obtain a sufficiently high S/N, so that we can measure average IR luminosities. We also stack the *Spitzer*/MIPS 24 μm images because of the high fraction of 24 μm-undetected objects ($S/N < 3$). In this analysis, all the stacks include both the detected and undetected objects. The stacking technique is described below.

We extract 40×40 pixel subimages centered on each target, and subtract all prior sources brighter than the detection limit of $S/N = 3$, using the scaled PSF method described in Section 5.2.4. We then combine these residual images by making an inverse-SFR-weighted average stack as follows. We normalize each 24 μm image by its $\mathrm{SFR}_{\mathrm{H}\alpha,\mathrm{H}\beta}$ and divide the sum of the normalized images by the sum of the weights (i.e., 1/SFR). We adopt inverse-SFR-weighted average stacks because ultimately we are interested in investigating the average of f_{24}/SFR and $L_{7.7}$/SFR ratios (Section 5.3.1). As we do not have direct far-IR detections for a majority of our galaxies, we can not construct inverse-L_{IR}-weighted average stacks. As a result, we use a 3σ-clipped mean or a median stack of 24, 100, and 160 μm images for the f_{24}/L_{IR} and $L_{7.7}/L_{\mathrm{IR}}$ analyses (Section 5.3.2). A comparison of these different stacking methods is presented in Appendix 5.8.

We calculate the stacked flux by performing aperture photometry on the stacked image. Based on the measured S/N of various aperture sizes, we adopt a 4-pixel radius aperture. The amount of light falling outside of the 4-pixel aperture is calculated using the PSF, and the fluxes are corrected accordingly. Similar to the PSF fitting technique, we measure background fluxes in 20 random positions to determine the noise (i.e., the uncertainty in the stacked 24 μm flux). There is little variation in the aperture corrections from field-to-field ($\lesssim 5\%$), which is negligible compared to the measurement errors.

5.2.6 νL_ν(7.7μm) and $L_{\rm IR}$

The k-correction required for converting 24 μm flux densities to rest-frame 7.7 μm luminosities is computed using the Chary & Elbaz (2001, hereafter, CE01) templates. First, we shift the templates to the redshift of each object (or median/weighted-average redshift of the stack), and then convolve the models with the 24 μm filter transmission curve. The best-fit model is determined through a least-χ^2 method and $\nu L_\nu(7.7\mu{\rm m})$ ($L_{7.7}$, in units of $L_\odot$) is extracted from the best-fit model.

To quantify the systematic biases from using different IR templates, we measure $L_{7.7}$ from the best-fit Dale & Helou (2002) and Rieke et al. (2009) models and compare them with those of CE01 (Figure 5.2). Adopting the Dale & Helou (2002) and Rieke et al. (2009) models would systematically increase the calculated $L_{7.7}$ by ~ 0.06 and ~ 0.10 dex, respectively. For a small fraction (4%) of galaxies, the Rieke et al. (2009) $L_{7.7}$ is larger than the CE01 $L_{7.7}$ by > 0.3 dex. However, these galaxies do not have systematically different masses or metallicities compared to that of the rest of the sample. Therefore, their $L_{7.7}$ offsets do not affect the mass and metallicity trends in this study.

Total IR luminosities ($L_{\rm IR}$, integrated from 8 to 1000 μm) are measured from the best-fit CE01 models to PACS 100 and 160μm stacks. We measure $L_{\rm IR}$ errors by perturbing the 100 and 160μm flux densities of each stack by their measurement uncertainties 10,000 times and calculating the 68% confidence intervals from these realizations. Furthermore, we verify that the best-fit models of Dale & Helou (2002) alter the inferred IR luminosities by only $\sim 5\%$, which is negligible compared to the typical $L_{\rm IR}$ measurement uncertainties of $\sim 10-20\%$.

5.3 PAH and ISM properties

In this section, we explore variations of the 7.7 μm PAH intensity in different ISM conditions, specifically with different gas-phase metallicities and ionization parameters. As a consequence of the correlation between metallicity and dust, we expect $L_{\rm IR}$ and SFR to correlate with metallicity such that metal-rich galaxies have higher SFRs and $L_{\rm IR}$. We quantify the PAH emission intensity by normalizing $L_{7.7}$ to either $\rm SFR_{H\alpha,H\beta}$ (Section 5.3.1) or $L_{\rm IR}$ (Section 5.3.2).

The fractional contribution of the stellar and dust continuum from very small grains (VSGs) to the 7.7 μm PAH emission varies in star-forming galaxies. Using a sample of local starburst galaxies, Engelbracht et al. (2008) showed that the stellar fractional contribution in the IRAC 8 μm band is 30 to 4% for $12 + \log({\rm O/H}) \sim 7.4$ to 8.7, respectively. Galaxies in our sample have $12 + \log({\rm O/H}) > 8$, suggesting a stellar fraction of $< 10\%$. Moreover, following the redshift evolution of SFR-M_* relation from $z \sim 0$ to 2 (e.g., Whitaker et al. 2014b), our galaxies have typically higher specific SFRs, and hence we expect lower stellar contamination in their mid-IR bands relative to local galaxies of the same stellar mass. Additionally, spectra of lensed high-redshift galaxies indicate a weak presence of mid-IR continuum (Rigby et al. 2008; Siana et al. 2009; Fadely et al. 2010) and high PAH emission contribution to the broadband 24 μm filter at $z \sim 2$ (Smith et al. 2007). Therefore, we conclude that the continuum contribution to our $L_{7.7}$ measurements

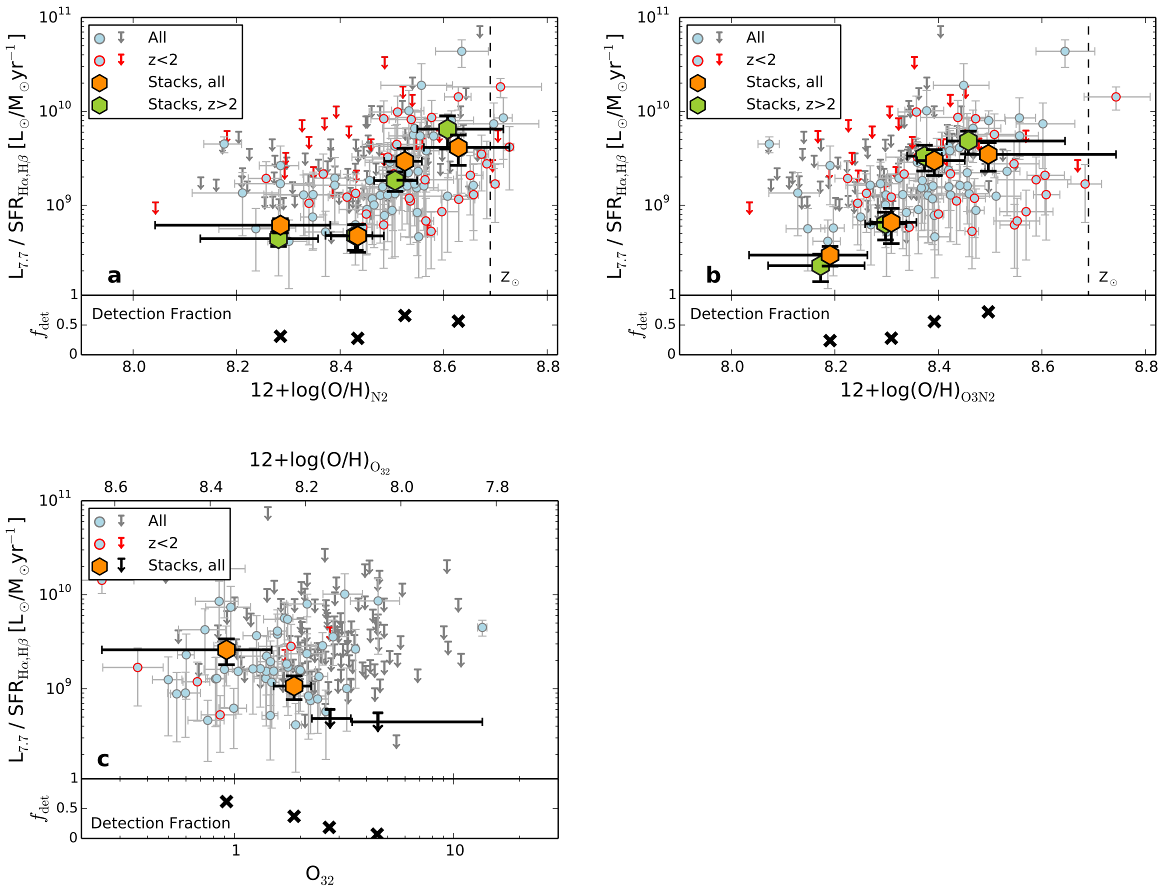

Figure 5.3 Ratio of 7.7 μm luminosity to dust-corrected $\mathrm{SFR}_{\mathrm{H}\alpha,\mathrm{H}\beta}$ as a function of (a) N2 metallicity, (b) O3N2 metallicity, and (c) O_{32} ratio. The O_{32} gas-phase metallicity (based on calibrations of Jones et al. 2015) is also displayed in panel (c). The plots show galaxies that have detections ($S/N > 3$) in all of the diagnostic emission lines used in each plot: panel (a) has objects detected in Hα, Hβ, and [NII] (total of 187 objects), panel (b) has objects detected in Hα, Hβ, [NII], and [OIII] (172 objects), and objects in panel (c) are detected in Hα, Hβ, [OIII], and [OII] (171 objects). AGNs and objects with 24 μm nearby neighbors are removed. Small circles and arrows indicate individual detections and 3 σ upper limits for non-detections at 24 μm, respectively. The 24 μm detection fraction in each bin is shown in the bottom panels. Red symbols show galaxies at $1.37 \leq z \leq 2.0$. The $L_{7.7}/\mathrm{SFR}_{\mathrm{H}\alpha,\mathrm{H}\beta}$ stacks are performed in bins of the quantity on the horizontal axis and include all the 24 μm detected and undetected galaxies in each bin. The horizontal error bars show the width of the bins. In panel (c), there are only 8 objects at $z < 2$, because [OII] is not covered by the MOSFIRE Y filter at $z \leq 1.6$. In panels (a) and (b), solar metallicity (12+log(O/H) = 8.69, Asplund et al. 2009) is indicated with a dashed line. Stack values are listed in Table 5.1.

is negligible. Future observations with *JWST*/MIRI will help to clarify the stellar and dust continuum contribution to the aromatic bands in the spectra of high-redshift galaxies. Compared to star-forming galaxies, AGNs typically have fainter PAH emission and a higher (non-negligible) fractional contribution of thermal and stellar continuum to the mid-IR emission (Smith et al. 2007). We removed the known AGNs from our sample (Section 5.2.1).

5.3.1 $L_{7.7}$/SFR and ISM properties

Due to the relatively shallow depth and poor spatial resolution of the far-IR data, obtaining robust individual far-IR measurements for a representative number of galaxies in our sample is not possible. Instead, we rely on our individual measurements of $\mathrm{SFR}_{\mathrm{H}\alpha,\mathrm{H}\beta}$ (Section 5.2.3). It was shown in Shivaei et al. (2016) that $\mathrm{SFR}_{\mathrm{H}\alpha,\mathrm{H}\beta}$ accurately traces SFRs up to $\sim 300\,M_{\odot}\,\mathrm{yr}^{-1}$, when compared with those from the IR.

We calculate inverse-$\mathrm{SFR}_{\mathrm{H}\alpha,\mathrm{H}\beta}$-weighted average stacks of $24\,\mu$m images (see Section 5.2.5) in four bins of metallicity with a roughly equal number of galaxies in each bin. The stacked $24\,\mu$m flux density is converted to $L_{7.7}$ using the CE01 IR templates (Section 5.2.6), and then divided by the weighted-average $\mathrm{SFR}_{\mathrm{H}\alpha,\mathrm{H}\beta}$. Dividing the inverse-$\mathrm{SFR}_{\mathrm{H}\alpha,\mathrm{H}\beta}$-weighted average $L_{7.7}$ to weighted average $\mathrm{SFR}_{\mathrm{H}\alpha,\mathrm{H}\beta}$ is mathematically equivalent to calculating an average of the $L_{7.7}/\mathrm{SFR}_{\mathrm{H}\alpha,\mathrm{H}\beta}$ ratios in each bin (Appendix 5.8). Properties of the stacks are listed in Table 5.1. Figure 5.3(a,b) shows $L_{7.7}$ to $\mathrm{SFR}_{\mathrm{H}\alpha,\mathrm{H}\beta}$ ratio as a function of N2 and O3N2 metallicities [1] (Section 5.2.2). The uncertainties in $L_{7.7}$/SFR

[1] Based on a small sample of three galaxies at $z \sim 2$, one lensed galaxy at $z = 1.4$, and nine $z \simeq 0.2$ green pea galaxies, Steidel et al. (2014) showed that the O3N2 index indicates a slightly better agreement with the direct T_e measurements of $12 + \log(O/H)$, relative to those computed using the N2 index.

ratios are calculated by adding the $L_{7.7}$ and SFR fractional uncertainties in quadrature. There is a clear increase of $L_{7.7}$/SFR with increasing metallicity. Considering the small fraction of 24 μm-detected objects in the two lowest metallicity bins, it is expected that the average $L_{7.7}/\mathrm{SFR}_{\mathrm{H}\alpha,\mathrm{H}\beta}$ ratios, which include all the detected and undetected 24 μm objects in the corresponding bins, will lie below the few individually 24 μm-detected sources. We consider separately the trends for the full redshift range, and for $z > 2$ alone. The $L_{7.7}$/SFR ratio increases by a factor of ~ 10 (~ 15) from the lowest to the highest metallicity bin in stacks of galaxies at $1.37 \leq z \leq 2.61$ ($2.0 \leq z \leq 2.61$).

We investigate the potential incompleteness of our samples due to the requirement of detecting the [NII] and [OIII] lines for N2 and O3N2 metallicties. The fractions of galaxies detected in [NII] ([OIII]) for the four bins of stellar mass indicated in Table 2 are 0.28, 0.56, 0.72, and 0.93 (0.28, 0.55, 0.68, and 0.83) proceeding from low to high stellar masses. As expected, more galaxies with undetected emission lines are missed from the N2 and O3N2 samples as we go to lower masses. However, in each mass bin, the distributions of the 24 μm S/N and f_{24} of the detected-line subsamples are very similar to that of the full sample (including detected and undetected [NII] and [OIII] lines). Additionally, in Section 5.5.1 we show the $L_{7.7}$ and L_{IR} stacks in bins of stellar mass regardless of the emission line detection. Both the $L_{7.7}$/SFR and $L_{7.7}/L_{\mathrm{IR}}$ ratios are suppressed at low masses, which correspond to low metallicities according to the mass-metallicity relation (Tremonti et al. 2004). We conclude that the sample incompleteness at low N2 and O3N2 metallicities is unlikely to be the dominant factor in driving the $L_{7.7}$/SFR and $L_{7.7}/L_{\mathrm{IR}}$ trends with metallicity.

Another important trend is the anti-correlation between the PAH intensity and O_{32} ratio. O_{32} is used as an empirical proxy for ionization parameter, which is in turn anti-correlated with metallicity (e.g., Pérez-Montero 2014, see also Figure 12 in Sanders et al. 2016a for the relation of O_{32} with O3N2 and N2 in MOSDEF). The weighted-average stacks of 24 μm images in the two highest O_{32} bins yield non-detections. In addition, objects with detected and undetected 24 μm emission are distinctly separated towards lower and higher O_{32}, respectively. The fraction of 24 μm-undetected objects increases significantly from 38% in the lowest O_{32} bin (median $O_{32} = 0.9$) to 91% in the highest bin (median $O_{32} = 4.5$), while the 24 μm non-detection fraction changes from $\sim 30\%$ at $12+\log(\mathrm{O/H}) \sim 8.6$ (8.5) to $\sim 60-70\%$ at $12+\log(\mathrm{O/H}) \sim 8.3$ (8.2) for N2 (O3N2) metallicities (refer to the bottom panels in Figure 5.3). These trends suggest that the PAH intensity is strongly affected by the ionization parameter. We will return to this point in Section 5.6.

Excluding the 24 μm-undetected objects from the analysis leads to a significantly biased sample. However, to explore the variations of 24 μm-bright sources with O_{32}, we stack only the 24 μm-detected objects in the same four bins of O_{32} as before. The results indicate that the $L_{7.7}$/SFR ratios of 24 μm-bright sources are almost independent of O_{32} within the uncertainties ($L_{7.7}/\mathrm{SFR} \sim 2.5 \times 10^9\,\mathrm{L}_\odot/M_\odot\mathrm{yr}^{-1}$ in all O_{32} bins.)

The PAH-metallicity correlation found at $z \sim 2$ is consistent with the trend observed at $z \sim 0$ (Engelbracht et al. 2005; Draine et al. 2007b; Galliano et al. 2008; Hunt et al. 2010, among others). In local galaxies, there is a paucity of PAH emission at $12+\log(\mathrm{O/H}) \lesssim 8.1-8.2$ (Engelbracht et al. 2005; Wu et al. 2006; Draine et al. 2007b). In Figure 5.3(c) we see the same threshold in the O_{32} plot at $z \sim 2$: there is a sharp difference in the $L_{7.7}/\mathrm{SFR}_{\mathrm{H}\alpha,\mathrm{H}\beta}$ ratio below and above $\mathrm{O}_{32} \sim 2$, which corresponds to $12 + \log(\mathrm{O/H})_{\mathrm{O}_{32}} \sim 8.2$ based on the metallicity calibrations of Jones et al. (2015). The threshold is at $12 + \log(\mathrm{O/H})_{\mathrm{N2}} \sim 8.5$ for the N2 metallicity calibration. We will discuss this observed threshold in more detail in Section 5.6.

Additionally, we examine possible variations of $L_{7.7}$ to $\mathrm{SFR}_{\mathrm{H}\alpha,\mathrm{H}\beta}$ (and to L_{IR}) ratio in the BPT diagram ([OIII]/Hβ vs. [NII]/Hα; Baldwin et al. 1981), as the position of galaxies below and above the BPT locus is known to be sensitive to the hardness of ionizing radiation (Kewley et al. 2013). We use the locus of $z \sim 2$ star-forming galaxies in the BPT diagram from Shapley et al. (2015) and stack 24 μm images of galaxies below and above the locus. Surprisingly, we do not find any evidence for variation of $L_{7.7}$ intensity in this parameter space, as galaxies at $z \geq 2$ below and above the BPT locus have the same $L_{7.7}/L_{\mathrm{IR}}$ ratio of 0.20 ± 0.03. *It is not clear why we do not see a significant change of the PAH intensity across the BPT diagram; it may be due to the small sample size.*

Our results directly show the correlation between the PAH emission and intensity of the radiation field as was speculated by Elbaz et al. (2011, hereafter, E11). In Elbaz et al. (2011), the reduced L_8/L_{IR} ratio was attributed to star formation "compactness" and "starburstiness" characterized by the SFR surface density and specific SFR, respectively. These authors concluded that the weak PAH emission in compact starbursts compared to their typical star-forming counterparts is a consequence of an increased radiation field intensity in these galaxies, which is directly shown by our results of decreasing PAH intensity with O_{32}. In other words, based on the assumption of a constant electron density (as electron density appears to be almost independent from other galaxy properties in MOSDEF, Sanders et al.

2016a), and the same ionizing spectrum, there is a tight correspondence between O_{32} and ionization parameter, such that increasing O_{32} reflects a more intense radiation field. This conclusion still holds even if we assume a different (harder) ionizing spectrum for the higher O_{32} bins, which would lower the inferred ionization parameter for a given O_{32} value (see Figure 10 in Sanders et al. 2016a).

5.3.2 $L_{7.7}/L_{\rm IR}$ and ISM properties

Estimating the total IR luminosity independent of f_{24} requires access to longer wavelength IR data. As mentioned before, in our sample, only very dusty star-forming galaxies with bright dust continua are detected in *Herschel*/PACS at 100 and 160 μm bands. Therefore, we rely on stacks of images to obtain a sufficiently high S/N to calculate robust IR luminosities.

Figure 5.4 shows $L_{7.7}/L_{\rm IR}$ stacks in bins of metallicity and O_{32}. We combine the two lowest metallicity bins and the two highest O_{32} bins in Figure 5.3 and Table 5.1 to gain higher S/N in the PACS stacks. The N2 stacks are adopted only for galaxies at $z > 2$, because otherwise the highest N2 metallicity bin is dominated by lower redshift ($z \sim 1.5$) galaxies. In O3N2 and O_{32} plots, the median redshifts of all bins are similar and all above $z = 2$. We note that there are only 8 galaxies at $z < 2$ in the O_{32} sample, as [OII] is not covered by the MOSFIRE Y filter at $z < 1.6$ (see Figure 5.3c). Properties of $L_{7.7}/L_{\rm IR}$ stacks are listed in Table 5.2.

To place our analysis in the context of other studies, we compare our results with E11, Reddy et al. (2012a, R12), and Wuyts et al. (2008, W08). E11 found that

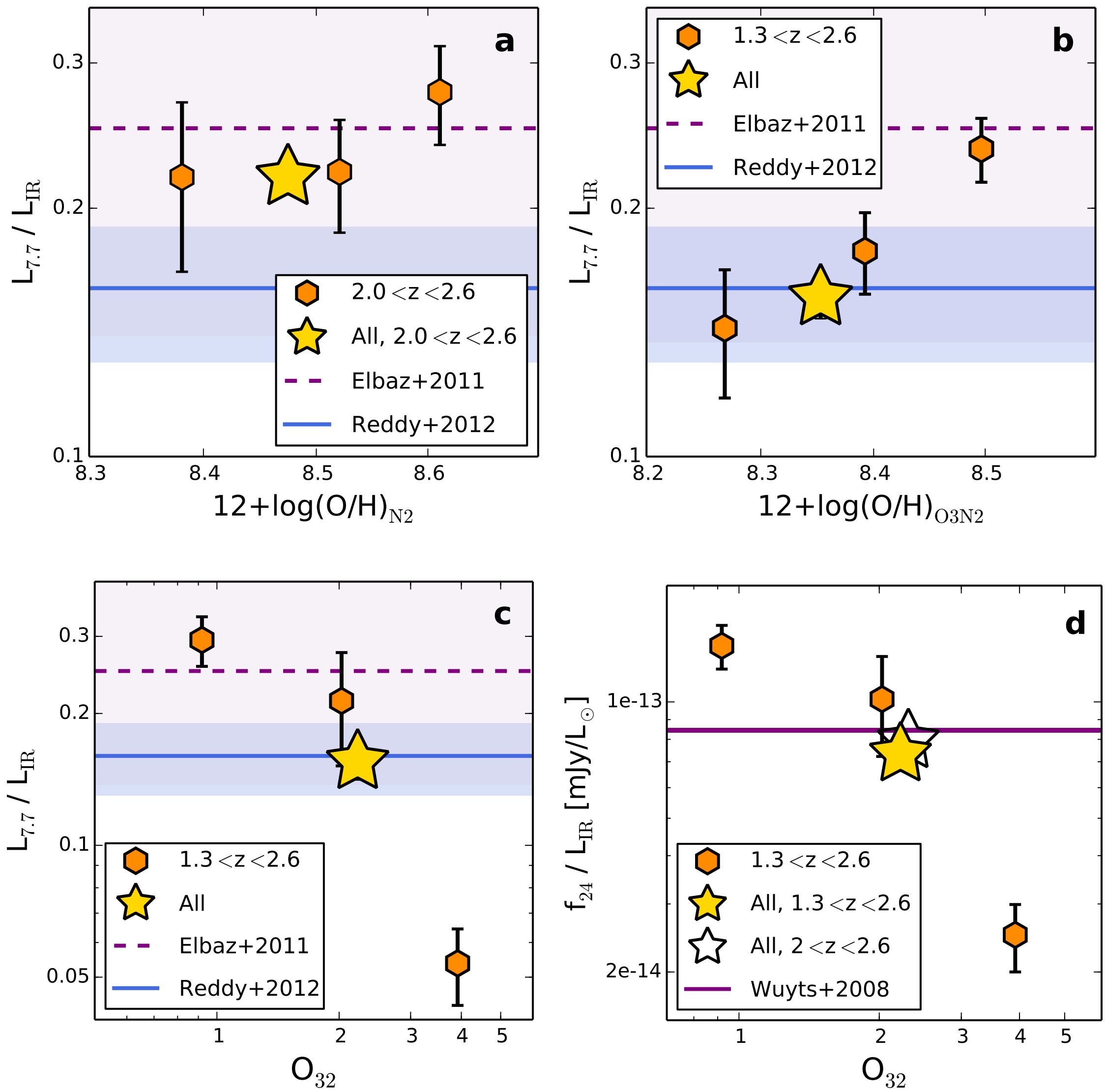

Figure 5.4 Relative strength of 7.7 μm luminosity to total IR luminosity as a function of N2 metallicity (a), O3N2 metallicity (b), O_{32} ratio (c), and ratio of 24 μm flux density to total IR luminosity versus O_{32} (d). In order to gain sufficient S/N in PACS bands, the lowest metallicity bins and the highest O_{32} bin have twice the number of galaxies in other bins. Yellow stars show stacks of all galaxies. For comparison, we show the $L_{7.7}/L_{\rm IR}$ conversions of E11 and R12 and the associated uncertainties with solid lines shaded regions, respectively. The $f_{24}/L_{\rm IR}$ ratio of W08 is plotted in panel d. The W08 ratio is redshift-dependent and the width of the purple line in plot (d) shows the range of values for the three bins. The N2 stacks are only performed for galaxies at $z > 2$, because otherwise the last bin would be biased towards galaxies at $z < 2.0$. Stacked values are listed in Table 5.2.

typical main-sequence galaxies between $z = 0-2.5$ follow a Gaussian distribution of $L_{\rm IR}/L_8$ ($\nu L_\nu(8\mu{\rm m}) \equiv L_8$) centered at $L_{\rm IR}/L_8 = 4$ ($\sigma = 1.6$) with a tail of starburst galaxies with larger $L_{\rm IR}/L_8$ ratios. The median $L_{\rm IR}/L_8$ ratio of all galaxies in their sample was $4.9^{+2.9}_{-2.2}$. Furthermore, the R12 study found $L_{\rm IR}/L_8 = 7.7 \pm 1.6$ for a sample of UV-selected galaxies at $1.5 \leq z < 2.6$ (with mean redshift of 2.08). R12 attributed their higher $L_{\rm IR}/L_8$ to redshift evolution and larger IR luminosity surface densities compared to those of the local galaxies. For a consistent comparison of these ratios with our results, we converted $L_8/L_{\rm IR}$ ratios of R12 and E11 to $L_{7.7}/L_{\rm IR}$ ratios. The E11 and R12 samples have $L_{\rm IR} = 5\times10^9 - 3\times10^{12}\,{\rm L}_\odot$ and $10^{10} - 5\times10^{12}\,{\rm L}_\odot$, respectively. According to the CE01 templates, νL_ν at $7.7\,\mu$m is higher than νL_ν at $8\,\mu$m by 29% for a template with $L_{\rm IR} = 5\times10^9\,{\rm L}_\odot$ and 12% for $L_{\rm IR}$ $= 5\times10^{12}\,{\rm L}_\odot$. The average $L_{\rm IR}$ in the R12 and E11 high-z samples is $\sim 2\times10^{11}\,{\rm L}_\odot$, which corresponds to a $L_{7.7}/L_8$ ratio of 1.25. Therefore, we adopt a correction factor of 1.25 to convert the E11 and R12 $L_8/L_{\rm IR}$ ratios to $L_{7.7}/L_{\rm IR}$ ratios. The variations of the $L_{7.7}/L_{\rm IR}$ ratios resulted from adopting other conversion factors (from 1.12 to 1.29) are well within the reported $1\,\sigma$ measurement uncertainty of $L_{7.7}/L_{\rm IR}$. After the conversion, we obtain $L_{7.7}/L_{\rm IR} = 0.25^{+0.15}_{-0.11}$ and 0.16 ± 0.03 for the E11 and R12 studies, respectively. These ratios and their confidence intervals are shown with lines and shaded regions in Figure 5.4. The $L_{7.7}/L_{\rm IR}$ of E11 is consistent with our highest metallicity and lowest O_{32} stacks. This is expected as at the same stellar mass, low-redshift galaxies have typically higher metallicities and less intense ionizing radiation fields. The $L_{7.7}/L_{\rm IR}$ of R12 is in agreement with our lower metallicity stacks and the middle O_{32} stack, as well as with the stacks of the full sample (yellow stars).

We also compare our results with those of Wuyts et al. (2008, 2011a). In these studies, the authors derived an empirical IR template and luminosity-independent monochromatic conversions from 24 μm flux density to $L_{\rm IR}$ as a function of redshift. We used the median redshifts of our three O_{32} stacks (from the lowest to the highest bin: $z = 2.29$, 2.27, and 2.29, Table 5.2) to adopt appropriate f_{24}-to-$L_{\rm IR}$ conversions and compare them with our results in Figure 5.4(d). The width of the purple line indicates the range of the W08 $f_{24}/L_{\rm IR}$ ratios for different redshifts of our three stacks. As expected, $f_{24}/L_{\rm IR}$ of W08 is consistent with our middle O_{32} bin as well as the stack of all objects, but there is discrepancy with the low and high O_{32} stacks. The same conclusion holds for the metallicity stacks. In Section 5.5, we will discuss the implications of the inconsistency between the $L_{7.7}$-to-$L_{\rm IR}$ conversions of W08, E11, and R12 with our observed values at low stellar masses.

5.4 PAH and Age

PAH molecules are thought to form in the outflows of carbon-rich AGB stars (e.g., Latter 1991; Tielens 2008). These evolved stars begin enriching the ISM after their death (at an age of ~ 400 Myr, Galliano 2011), as opposed to core-collapse supernovae explosions, which enrich the ISM with dust on short timescales following the onset of star formation ($\lesssim 10$ Myr). As a result, some studies suggest that the correlation between the PAH intensity and metallicity arises because of the delayed formation of the PAH molecules in chemically young systems (Dwek 2005; Galliano et al. 2008). Galliano et al. (2008) modeled the dust production associated with massive and AGB stars and showed that

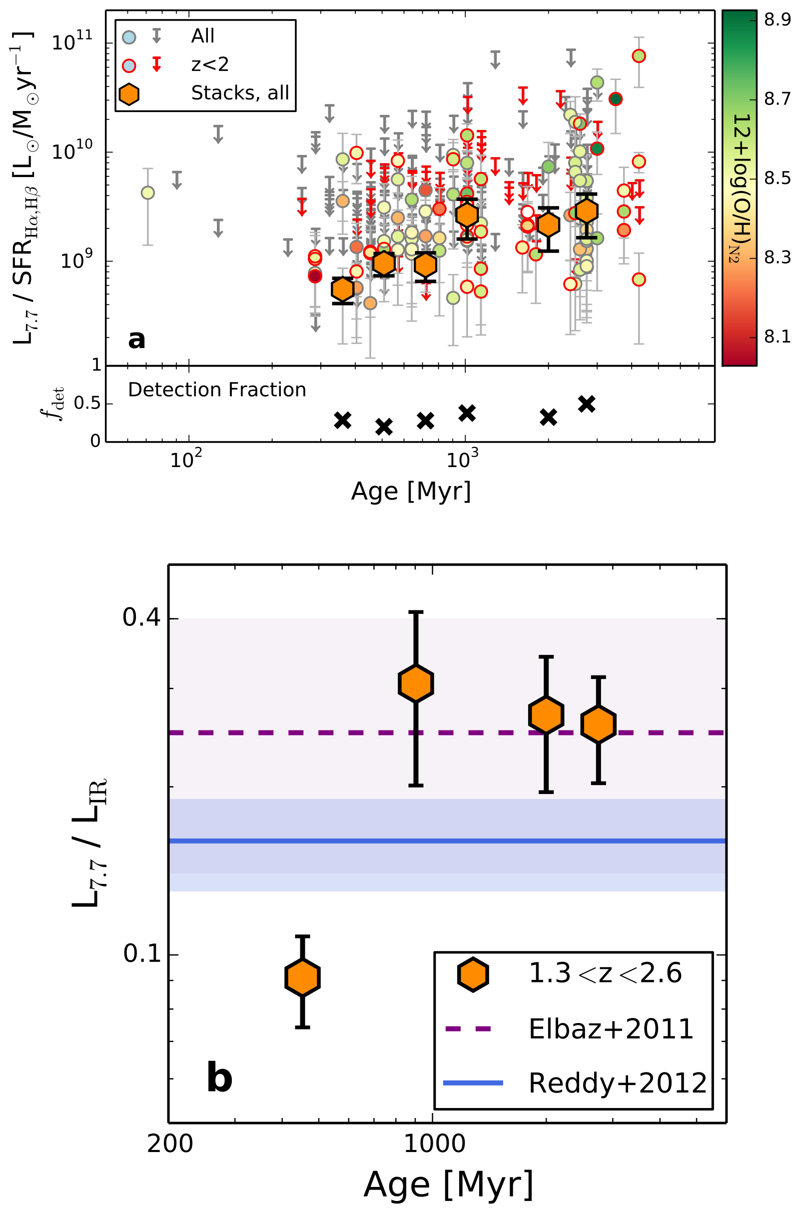

Figure 5.5 (a): ratio of $L_{7.7}$ to $\mathrm{SFR}_{\mathrm{H}\alpha,\mathrm{H}\beta}$ as a function of age. Symbols are the same as Figure 5.3. Individual galaxies are color coded based on their N2 metallicity. (b): ratio of 7.7 μm luminosity to L_{IR} as a function of age. Symbols are the same as Figure 5.4. Ages are derived from the best-fit SEDs. Stacked values are listed in Tables 5.1 and 5.2.

PAHs are less abundant in young metal-poor systems. To test this scenario, we investigate the PAH intensity as a function of age in our sample.

In Figure 5.5, we show the trend of $L_{7.7}$/SFR and $L_{7.7}/L_{\rm IR}$ as a function of age. Ages are derived from the best-fit SED models (Section 5.2.3). The PAH intensity is essentially constant within the errors at ages $\gtrsim 900$ Myr, but both the $L_{7.7}$/SFR and $L_{7.7}/L_{\rm IR}$ ratios drop significantly by a factor of ~ 3 for young galaxies with ages $\sim 300 - 800$ Myr. Galaxies with ages $\lesssim 500$ Myr (the first bin in Figure 5.5a) have a wide range of metallicities ($12 + \log({\rm O/H})_{\rm O3N2} \sim 8 - 8.6$), although the metallicities are systematically lower (median of 8.2) compared to that of the whole sample (median of 8.3). To demonstrate that metallicity can not completely account for the variation of $L_{7.7}/{\rm SFR}_{{\rm H}\alpha,{\rm H}\beta}$ with age, we randomly draw galaxies from the old population (with ages > 500 Myr), such that the subsample has the same metallicity distribution as that of the young population (with ages ≤ 500 Myr). We stack the 24 μm images, and find that the average $L_{7.7}$/SFR of the old population subsample is a factor 3 larger than the average $L_{7.7}$/SFR of the young population, although they have the same metallicity distribution. This indicates that the observed deficit of PAH emission in young galaxies cannot be *fully explained* by low metallicity and high ionization parameter.

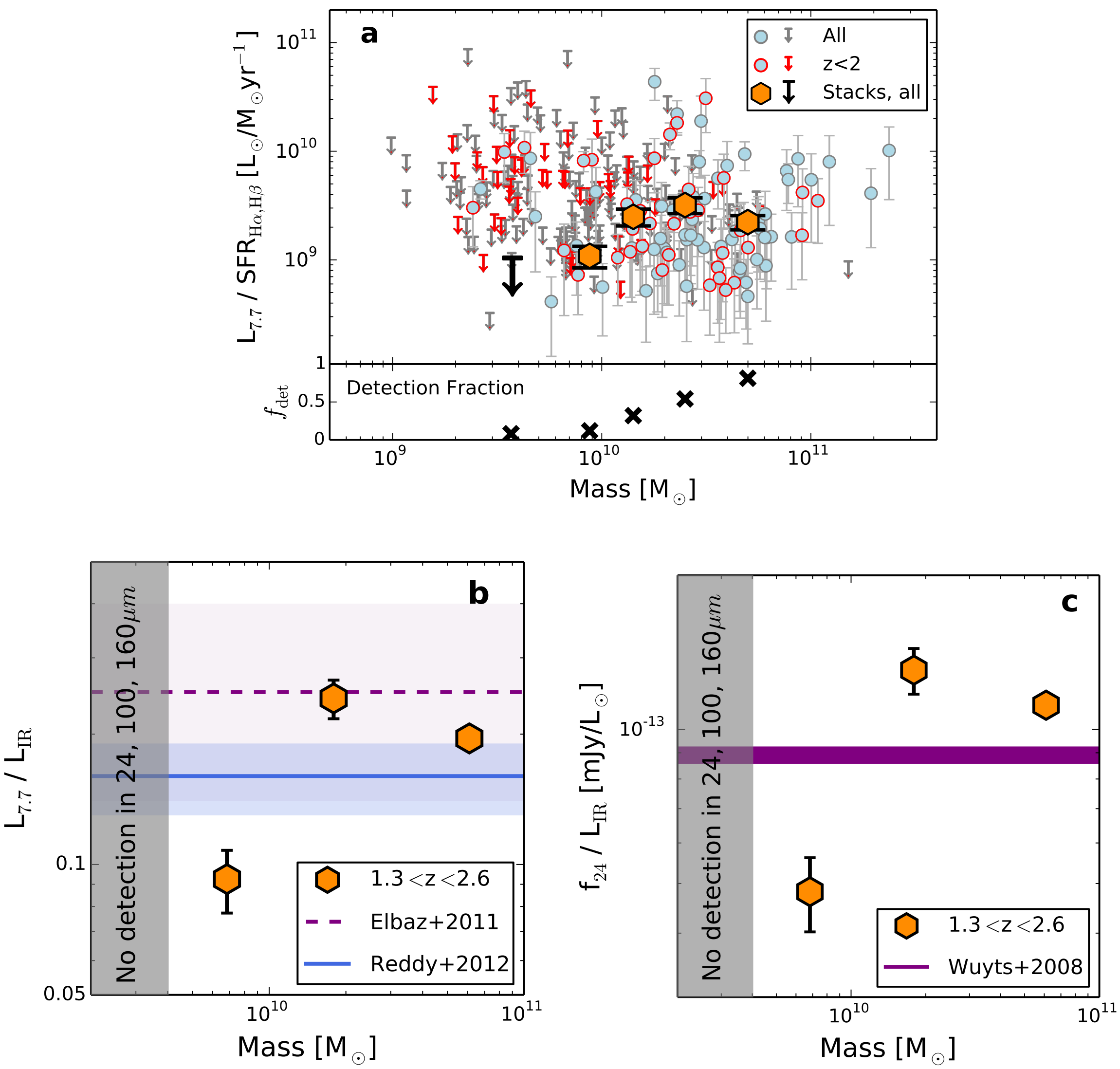

Figure 5.6 (a): ratio of $L_{7.7}$ to $\mathrm{SFR}_{\mathrm{H}\alpha,\mathrm{H}\beta}$ as a function of stellar mass. Symbols are the same as Figure 5.3. (b) and (c): ratio of 7.7 μm luminosity and 24 μm flux density to L_{IR} as a function of M_*, respectively. Symbols are the same as Figure 5.4. In the lowest mass bin ($M_* \leq 10^{9.6}\,\mathrm{M}_\odot$) none of the 24 μm, 100 μm, and 160 μm fluxes are detected at 2.5σ. Stacked values are listed in Tables 5.1 and 5.2.

5.5 $L_{7.7}$ as a tracer of Total IR Luminosity: Implications for High-z studies

As shown in Figures 5.3 and 5.4 and discussed in Section 5.3, the ratio of rest-frame $L_{7.7}$ to SFR or $L_{\rm IR}$ strongly depends on metallicity and O_{32}. Figure 5.6 shows the correlation between $L_{7.7}/L_{\rm IR}$ and M_*, which likely arises from the correlation between M_* and metallicity (Tremonti et al. 2004) and the anti-correlation between M_* and O_{32} (e.g., Sanders et al. 2016a).

Similar to the 24 μm-to-IR conversions of W08, E11, and R12, luminosity-dependent conversions of Caputi et al. (2007), Bavouzet et al. (2008), Rigby et al. (2008), and Reddy et al. (2010) are also only consistent with massive galaxies with $M_* \gtrsim 10^{10}\,{\rm M}_\odot$ and $L_{\rm IR} \gtrsim 10^{11-11.5}\,{\rm L}_\odot$. In the next two sections we will discuss the implications of this result for high-redshift studies.

5.5.1 The SFR-M_* relation

In Shivaei et al. (2016) we discussed how SFR-M_* studies at $z \sim 2$ that rely on Hα SFRs predict shallower log(SFR)-log(M_*) slopes ($\sim 0.5 - 0.7$, Erb et al. 2006c; Zahid et al. 2012; Koyama et al. 2013; Atek et al. 2014; Darvish et al. 2014; Shivaei et al. 2016), compared to those that utilize IR SFRs (slope of ~ 1, Daddi et al. 2007a; Santini et al. 2009; Wuyts et al. 2011b; Reddy et al. 2012b; Whitaker et al. 2014b). In order to understand the cause of this discrepancy, in Shivaei et al. (2016) we compared ${\rm SFR}_{{\rm H}\alpha,{\rm H}\beta}$ with SFRs inferred from panchromatic SED models that were fit to rest-frame UV to far-IR photometry. The

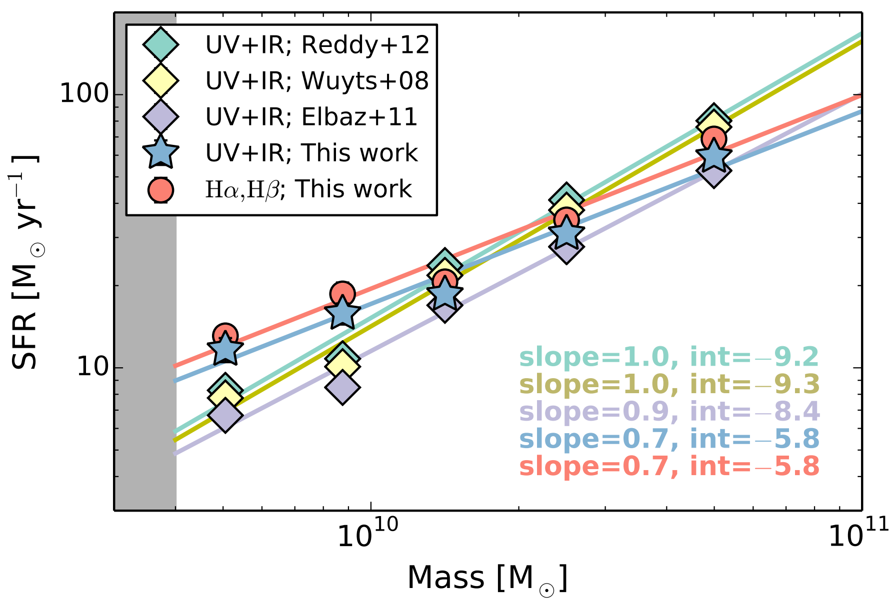

Figure 5.7 SFR in bins of stellar mass. Orange circles are 3σ-clipped means of dust-corrected $SFR_{H\alpha,H\beta}$ in each bin. Other symbols show the sum of SFR_{UV} at 1600Å and SFR_{IR} derived from 24 μm stacks using different conversions. Blue stars adopt the conversion derived in this study (Figure 5.6b): $L_{7.7}/L_{IR}$= 0.09 and 0.22 for M_* below and above 10^{10} $M_\odot$, respectively. Cyan, yellow, and purple diamonds are from single-value conversions of R12, W08, and E11, respectively. We use the median redshift in each bin to adopt the corresponding W08 conversion. The SFR_{IR} and $SFR_{H\alpha,H\beta}$ errorbars are the same size as the symbols. The best-fit lines, slopes, and intercepts estimated from a simple linear least-squares regression to log(SFR) vs. log(M_*) are shown on the plot with respective colors. The grey region shows $M* \leq 10^{9.6}$ $M_\odot$, where the 24 μm stack is not detected.

comparison indicated that $\mathrm{SFR}_{\mathrm{H}\alpha,\mathrm{H}\beta}$ does not underpredict total SFR even for the most star-forming and dusty galaxies in our sample (up to $\sim 300\,M_\odot\,\mathrm{yr}^{-1}$). In this section, we examine whether the discrepancy in the slope of the SFR-M_* relation arises from the 24 μm-inferred IR SFRs that are not corrected for the PAH-metallicity effect.

Figure 5.7 shows SFR in bins of stellar mass for galaxies with $M_* \geq 10^{9.6}\,\mathrm{M}_\odot$. In Figure 5.7, orange circles denote mean $\mathrm{SFR}_{\mathrm{H}\alpha,\mathrm{H}\beta}$ and other symbols are mean $\mathrm{SFR}_{\mathrm{UV}}$ added to mean $\mathrm{SFR}_{\mathrm{IR}}$, where the latter is derived from various conversions of f_{24} to L_{IR} adopted from the literature (diamonds) and from this analysis (blue stars), which is described as follows. We derive a mass-dependent conversion of $L_{7.7}$ to L_{IR} based on our stacks presented in Figure 5.6(b,c) and Table 5.2. The $L_{7.7}/L_{\mathrm{IR}}$ ratio is 0.09, 0.24, and 0.20 for $\log(M_*/\mathrm{M}_\odot) = 9.6-10.0, 10.0-10.6$, and $10.6-11.6$, respectively. We adopt $L_{7.7}/L_{\mathrm{IR}} = 0.09$ for $M_* < 10^{10}\,\mathrm{M}_\odot$ and an average of the two highest mass bins, 0.22, for $M_* \geq 10^{10}\,\mathrm{M}_\odot$[2]. The result is shown with blue stars in Figure 5.7. The diamonds in Figure 5.7 reflect results of the mass-independent 24 μm-to-IR conversions of R12, W08, and E11. The 24 μm stack below $10^{9.6}\,\mathrm{M}_\odot$ (shaded grey region in Figure 5.7) is not robustly detected, owing to the reduced dust emission at low masses and low SFRs.

The $\mathrm{SFR}_{\mathrm{UV}} + \mathrm{SFR}_{\mathrm{IR}}$ derived from the mass-dependent 24 μm-to-IR conversion presented in this study is in a very good agreement with $\mathrm{SFR}_{\mathrm{H}\alpha,\mathrm{H}\beta}$, particularly considering that these two SFRs are derived completely independently from each other. As expected, the other IR SFRs that are inferred from a single 24 μm-to-IR conversion are underestimated for low mass ($M_* < 10^{10}\,\mathrm{M}_\odot$) galaxies. Figure 5.7 clearly demonstrates how using a single

[2]We express our results in terms of mass dependence so as to avoid biases that may be introduced by excluding objects without detections of some of the strong lines required to calculate metallicities. The metallicity dependence of the $L_{7.7}/L_{\mathrm{IR}}$ ratios are reported in Table 5.2.

24 μm-to-IR conversion can underestimate SFRs at lower masses and lead to a steeper log(SFR)-log(M_*) slope compared to that derived in this study. A simple linear least-squares regression calculation gives a slope of 1.0 ± 0.1 for the stacks of $\mathrm{SFR_{UV}} + \mathrm{SFR_{IR}}$ that assume the W08, E11, and R12 conversions and a slope of 0.7 ± 0.1 for the $\mathrm{SFR_{H\alpha,H\beta}}$ and the $\mathrm{SFR_{UV}} + \mathrm{SFR_{IR}}$ stacks that adopt our mass-dependent conversion.

The slope of 0.7 found in this study is consistent with observations at lower redshifts (slope ~ 0.7 at $z \sim 0.1$ and 1, Salim et al. 2007 and Noeske et al. 2007a, respectively), suggesting no evolution in the slope of the SFR-M_* relation from $z \sim 0$ to 2. Moreover, the increased $\mathrm{SFR_{UV}} + \mathrm{SFR_{IR}}$ of the low-mass galaxies estimated from our mass-dependent 24 μm-to-IR conversion, removes evidence for a "flattening" at the high-mass end of the SFR-M_* relation, as suggested in some previous studies (e.g., Whitaker et al. 2014b; Schreiber et al. 2015). However, it is plausible that the slope of the relation steepens at masses lower than those accessible in this study – a mass-independent shallow slope of 0.7 would lead to a too rapid evolution in the stellar mass function at low masses (Weinmann et al. 2012; Leja et al. 2015).

Our results indicate that specific SFR (sSFR $\equiv \mathrm{SFR}/M_*$) is a decreasing function of M_*. If we assume that the gas and stars occupy the same regions in the galaxies, then the Schmidt relation (Kennicutt 1998) implies that $\mathrm{SFR} \propto M_{\mathrm{gas}}^{1.4}$. Consequently, sSFR is related to the cold gas fraction defined as $M_{\mathrm{gas}}/(M_* + M_{\mathrm{gas}})$ (Reddy et al. 2006b). The negative slope of the log(sSFR)-log(M_*) relation indicates that, as expected, there is a correspondence between the cold gas fraction and stellar mass.

There is tension between our results and those from simulations. According to simulations, the slope of the SFR-M_* relation is close to unity and the sSFR is almost a constant function of mass (Dutton et al. 2010; Davé et al. 2011a; Torrey et al. 2014; Kannan et al. 2014; Sparre et al. 2015a, among many others). Furthermore, our analysis shows an increased sSFR at $M_* = 5\times10^9$ at $z\sim2$ by a factor of 1.8 (log(sSFR/Gyr) = 0.4), compared to the previous sSFR measurements that used mass-independent 24μm-to-IR conversions. The increased sSFR found here also aggravates the inconsistency between observations and models, where the models predict lower sSFRs at $z\sim2$ than those reported in previous studies (Furlong et al. 2015; Sparre et al. 2015a; Davé et al. 2016). From the observational viewpoint, we showed in Shivaei et al. (2015a) that our MOSDEF Hα-detected sample is complete down to $M_* = 10^{9.5}\,M_\odot$. Therefore, the shallow slope of 0.7 in this study is immune from the common sample selection biases at low masses. On the other hand, Davé (2008) and Torrey et al. (2014) demonstrated that changing feedback models in simulations does not affect the slope of the relation, as it moves galaxies along the SFR-M_* relation. More investigations are needed to resolve these issues and improve the agreement between simulations and observations.

5.5.2 Bolometric luminosity density at $z\sim2$

Luminous infrared galaxies (LIRGs) with $L_{\rm IR} = 10^{11} - 10^{12}\,L_\odot$, are known to contribute significantly to the total IR luminosity density at $z\sim2$ (Reddy et al. 2008; Rodighiero et al. 2010; Magnelli et al. 2011). Current measurements of the IR luminosity density (and the obscured SFR density) at $z\sim2$ are either based solely on ultra luminous infrared galaxies (ULIRGs) with $L_{\rm IR} > 10^{12}\,L_\odot$ (e.g., Gruppioni et al. 2013) or have included lower IR luminosities by relying on different methods of converting 24 μm flux density to $L_{\rm IR}$ (e.g., Pérez-González et al. 2005; Caputi et al. 2007; Reddy et al. 2008, 2010; Rodighiero et al. 2010; Riguccini et al. 2011). The most common method uses empirical IR templates that are calibrated with local galaxies (e.g., CE01, Dale & Helou 2002, Rieke et al. 2009). These IR templates are shown to overestimate $L_{\rm IR}$ for ULIRGs at $z \sim 2$ (Nordon et al. 2010; Elbaz et al. 2011; Reddy et al. 2012a). To overcome this so-called "mid-IR excess," other 24 μm-to-IR conversions that were calibrated with samples of high-redshift galaxies were introduced (Bavouzet et al. 2008; Elbaz et al. 2011, among many others). However, the dependence of $L_{7.7}/L_{\rm IR}$ on metallicity and stellar mass was neglected in these calibrations. As we showed in previous sections, these conversions underpredict $L_{\rm IR}$ at low and moderate masses ($M_* \lesssim 10^{10}\,{\rm M_\odot}$) and IR luminosities ($L_{\rm IR} \lesssim 10^{11}\,{\rm L_\odot}$).

The increased $L_{\rm IR}$ of the low and moderately IR luminous galaxies leads to a higher IR luminosity density at $z \sim 2$. To quantify this effect, we simulate 1000 galaxies drawn from the double power law luminosity function of Magnelli et al. (2011), increase the IR luminosities of galaxies below $L_{\rm IR} = 10^{11}\,{\rm L_\odot}$ in accordance with the relations found in this study (as discussed below), bin the galaxies (we used bins with 0.3 dex width, similar to Magnelli et al. 2011), and re-fit the bins with the double power law function. We use two alternative methods to include the increased $L_{\rm IR}$ of low-luminosity galaxies. In the first method, we increase $L_{\rm IR}$ by a factor of 2 for all simulated galaxies with $L_{\rm IR} \leq 10^{11}\,{\rm L_\odot}$. This assumption is motivated by our finding for the low-mass galaxies in the previous section (Section 5.5.1). However, from our data it is not clear whether $L_{\rm IR}$ of faint IR galaxies should be increased by a greater factor or an equal factor compared to that of the moderately IR luminous galaxies. Therefore, as a sanity check we adopt a second approach, where $L_{\rm IR}$ is increased by a factor of 2 for galaxies with $L_{\rm IR} \leq 10^{10}\,{\rm L}_{\odot}$, and by a factor of 1.5 for those with $10^{10} < L_{\rm IR} \leq 10^{11}\,{\rm L}_{\odot}$. In both cases, the number density of IR bins below $10^{11}\,{\rm L}_{\odot}$ increases by $\gtrsim 0.3$ dex, and the faint-end slope steepens from -0.6 to ~ -0.7. The increase in the slope is within its 1σ error of 0.1 (Sanders et al. 2003; Magnelli et al. 2011). A stronger variation in $L_{\rm IR}$ would cause a steeper faint-end slope, resulting in a higher fractional contribution of galaxies with $L_{\rm IR} \lesssim 10^{11}{\rm L}_{\odot}$ to the total IR budget and obscured SFR density at $z \sim 2$ than predicted before (Caputi et al. 2007; Reddy et al. 2010).

If we assume the same fractional contribution of the faint and moderately luminous IR galaxies to the bolometric (i.e., IR+UV) luminosity density at $z \sim 2$, as derived in previous studies ($\sim 50 - 80\%$, Caputi et al. 2007; Reddy et al. 2008; Rodighiero et al. 2010), our estimate of a factor of ~ 2 increase in the IR luminosity of galaxies with $L_{\rm IR} \lesssim 10^{11}{\rm L}_{\odot}$ would increase the IR luminosity density by 30%. Applying the 30% increase to the IR luminosity density measurement of Reddy et al. (2008) at $z \sim 2$, and converting it to IR SFR density using the Kennicutt (1998) relation, modified for a Chabrier (2003) IMF[3], yields an IR SFR density of $0.15\,{\rm M}_{\odot}\,{\rm yr}^{-1}\,{\rm Mpc}^{-3}$. Adding this value to the UV SFR density measured in the same study (Reddy et al. 2008) results in a total SFR density of $0.18\,{\rm M}_{\odot}\,{\rm yr}^{-1}\,{\rm Mpc}^{-3}$ (assuming a Chabrier (2003) IMF), which is $\sim 30\%$ higher than the initial value calculated from the unchanged IR luminosity density. This finding exacerbates the discrepancy between the stellar mass density at $z \sim 2$ measured from observations and that obtained by integrating the SFR density over time (Hopkins & Beacom 2006; Madau & Dickinson 2014).

[3]Assuming a Salpeter (1955) IMF increases the SFR density values by a factor of ~ 1.8.

5.6 Why is PAH intensity correlated with metallicity?

The correlation between PAH intensity and metallicity has been observed and studied extensively in the local universe (Engelbracht et al. 2005 and Madden et al. 2006 were among the first). Several scenarios have been proposed to explain the observed trend, which involve the production mechanisms of PAH molecules or various ways of destroying them.

The origin of PAHs in galaxies is not completely understood, but evolved carbon stars are undoubtedly one of the main sources (Latter 1991; Tielens 2008). The presence of PAHs in the outflows of carbon-rich AGB stars is confirmed both in theoretical (Frenklach & Feigelson 1989; Cau 2002; Cherchneff 2006) and observational (Beintema et al. 1996; Boersma et al. 2006) studies. As a consequence, it is expected that chemically young systems should have reduced PAH abundances (Dwek 2005; Galliano et al. 2008). Also, PAH molecules are not as efficiently produced in low metallicity environments because fewer carbon atoms are available in the ISM. On the other hand, PAHs can be destroyed in hostile environments such as supernovae shocks (O'Halloran et al. 2006). PAHs can also be effectively destroyed in low-metallicity environments with hard ionization fields, due to reduced shielding by dust grains (Madden et al. 2006; Smith et al. 2007; Hunt et al. 2010). Some authors have explored the size distribution of PAHs and suggested that there is a deficit of *small* PAH molecules at low metallicites (Hunt et al. 2010; Sandstrom et al. 2010).

The nature of the PAH-metallicity correlation is likely a combination of the production and destruction scenarios mentioned above. In our sample of galaxies at $z \sim 2$, we find strong trends between the PAH intensity and metallicity, O_{32}, and age, in agreement with both the formation and destruction scenarios. However, the significant increase in the fraction of undetected 24 μm sources with increasing O_{32} (from 38% to 91%, Figure 5.3c) suggests that the destruction of PAHs in intense radiation fields may be the dominant physical mechanism. The low PAH emission could also be caused by the absorption of stellar UV photos by dust in the HII region before reaching the PAHs in the photodissociation region (PDR, Peeters et al. 2004). In this case, PAHs exist, but they are not exposed to the UV photons, and hence, do not emit in the mid-IR. However, in the case of a substantially dusty HII region, the recombination lines would also be systematically suppressed, thus resulting in systematic discrepancies between the UV- and Hα-inferred SFRs. Such discrepancies are not observed in our sample (see Reddy et al. 2015; Shivaei et al. 2016). Nevertheless, it is not trivial to completely differentiate between the various scenarios with our current data set.

A potentially important trend observed in Figure 5.6 is that above $M_{*} \sim 10^{10}$ the $L_{7.7}/L_{\rm IR}$ (or $L_{7.7}$/SFR) reaches an almost constant value. This "flattening" is also seen in $L_{7.7}/L_{\rm IR}$ below $O_{32} \sim 2.2$ (above $12 + \log({\rm O/H})_{\rm O_{32}} \sim 8.2$, Figure 5.3c) and above the age of ~ 900 Myr. We speculate that the observed metallicity (and mass) threshold reflects the point above which enough dust particles are produced to shield the ionizing photons and prevent the PAH destruction. This suggests that the constant value of $L_{7.7}/L_{\rm IR}$ at high metallicities is the "equilibrium" $L_{7.7}/L_{\rm IR}$ ratio. The suppressed $L_{7.7}/L_{\rm IR}$ at lower metallicities is indicative of preferential destruction of PAHs in environments with lower dust opacity, and hence, with harder and more intense radiation fields. The paucity of PAH emission in young galaxies can also be attributed to the delayed production of PAHs by

AGB stars and/or to the higher intensity of the radiation field in these young systems with high sSFR. The threshold at $12 + \log(\mathrm{O/H})_{\mathrm{O32}} \sim 8.2$ is the same as the value found by Engelbracht et al. (2005) and close to the value 8.1 found by Draine et al. (2007b) at $z \sim 0$.

5.7 Summary

We present the first results of investigating variations of the brightest PAH emission at 7.7μm with metallicity and ionizing radiation intensity at high redshift. For this study, we use the MOSDEF sample of star-forming galaxies at $1.37 \leq z \leq 2.61$ that covers a broad range of metallicities ($\sim 0.2 - 1\,\mathrm{Z}_\odot$), stellar masses ($M_* \sim 10^9 - 10^{11.5}\,\mathrm{M}_\odot$), and SFRs ($\sim 1 - 200\,M_\odot \mathrm{yr}^{-1}$). We adopt the N2 and O3N2 diagnostics of metallicity, and use O_{32} as a proxy for ionization parameter. We quantify the PAH strength as the ratio of rest-frame 7.7μm luminosity ($\nu L_\nu(7.7\mu\mathrm{m})$), traced by *Spitzer*/MIPS 24μm, to dust-corrected $\mathrm{SFR}_{\mathrm{H}\alpha,\mathrm{H}\beta}$ and total IR luminosity. The main conclusions are as follows:

- We find that, in agreement with studies of local galaxies, the PAH intensity depends strongly on gas-phase metallicity. The relative strength of $L_{7.7}$ to SFR decreases by a factor of ~ 10 from median metallicities of $\mathrm{Z} \sim 0.6$ to $0.3\,\mathrm{Z}_\odot$.
- There is a significant anti-correlation between the PAH intensity and O_{32}. This trend is stronger than the correlation of PAH with N2 and O3N2, as the majority of 24μm undetected galaxies have systematically high O_{32} ratios. The $L_{7.7}/L_{\mathrm{IR}}$ ratio changes from 29% at $\mathrm{O}_{32} \sim 0.9$ to 5% at $\mathrm{O}_{32} \sim 4$. The trends of the PAH strength with O_{32}, O3N2, and N2 suggest preferential destruction of PAH molecules in low metallicity environments, characterized with harder and more intense radiation fields. Addi-

tionally, there is a sharp difference in the PAH intensity above and below $O_{32} \sim 2$ $(12+\log(O/H)_{O_{32}} \sim 8.2)$. This threshold is also observed at $z \sim 0$. We speculate that above this metallicity threshold dust opacity is high enough that PAHs are no longer preferentially destroyed by ionizing photons, and hence, the $L_{7.7}/L_{\rm IR}$ ratio reaches a constant value.

- For galaxies older than $\sim$1 Gyr, we do not find a correlation between age and the PAH intensity. However, the $L_{7.7}/L_{\rm IR}$ ratios of the youngest quartile of galaxies in our sample (with ages $\sim 50-600$ Myr) are significantly lower (by a factor of ~ 3) than those of galaxies with ages $\gtrsim 900$ Myr. The low PAH intensity in young systems may be an indication of the delayed injection of PAH molecules to the ISM by carbon-rich AGB stars.

- As a consequence of the mass-metallicity relation, we see a strong correlation between the PAH intensity and stellar mass. We show that commonly-used conversions of L_8 (or f_{24}) to $L_{\rm IR}$ at $z \sim 2$ are only valid for massive and metal-rich galaxies. For galaxies with $M_* \lesssim 10^{10}\,M_\odot$, these conversions should be applied with caution as they underestimate the $L_{\rm IR}$ and SFR by a factor of ~ 2.

- The results of this analysis affect high-redshift studies that adopt mass (and metallicity) independent conversions of 24 μm flux density to $L_{\rm IR}$ and SFR over a large range of masses and metallicities. We show that by using our mass-dependent conversion of $L_{7.7}$ to $L_{\rm IR}$ ($L_{7.7}/L_{\rm IR}$=0.09 and 0.22 for M_* below and above $10^{10}\,M_\odot$, respectively), the slope of the $\mathrm{SFR_{UV+IR}}$-M_* relation decreases from unity to 0.7. The shallower slope of 0.7 is in agreement with the independently-derived slope of the $\mathrm{SFR_{H\alpha,H\beta}}$-

M_* relation. Our results imply a higher sSFR (by a factor of 1.8) at $M_* \lesssim 10^{10}\,\mathrm{M}_\odot$ compared to the previous IR+UV measurements. Based on this analysis, sSFR is a decreasing function of M_*, indicating a mass-dependent cold gas fraction in galaxies at $z \sim 2$. Our results are inconsistent with the unity slope of the SFR-M_* relation derived from simulations, and add to the longstanding problem of models underestimating the sSFR at $z \sim 2$.

- Our analysis suggests a higher bolometric luminosity density and SFR density by $\sim 30\%$ at $z \sim 2$, due to a factor of ~ 2 increase in the IR luminosity of low and moderately luminous IR galaxies ($L_{\mathrm{IR}} \lesssim 10^{11}\mathrm{L}_\odot$). This result reinstates the tension between the measured stellar mass density and the integral of SFR density at $z \sim 2$.

We provide ratios of $L_{7.7}$-to-SFR and $L_{7.7}$-to-L_{IR} as a function of metallicity, O_{32}, stellar mass, and age in Tables 5.1 and 5.2 as a reference to be used for future studies of galaxies at $z \sim 2$.

In the future, with a larger sample of galaxies at $1.37 \leq z \leq 2.0$, we will study the PAH intensity at different redshifts from $z \sim 1.5$ to 2.5, as well as incorporating $z \sim 0$ studies to construct a comprehensive picture of the evolution of PAHs over cosmic time. Moreover, future generations of ground- (e.g., TMT and E-ELT) and space-based (e.g., *JWST*) telescopes will significantly improve our knowledge about PAH molecules in the distant universe by extending the redshift range over which we can observe PAH emission and enabling us to probe a larger dynamic range of metallicity, O_{32}, age, and stellar mass.

The authors thank the referee for thoughtful suggestions. We thank Mark Dickinson and Hanae Inami for providing part of the IR data, and Romeel Davé, Lee Armus, George Rieke, David Cook, Marjin Franx, Joel Leja, and Louis Abramson for useful discussion. Support for IS is provided through the National Science Foundation Graduate Research Fellowship DGE-1326120. NAR is supported by an Alfred P. Sloan Research Fellowship. Funding for the MOSDEF survey is provided by NSF AAG grants AST-1312780, 1312547, 1312764, and 1313171 and archival grant AR-13907, provided by NASA through a grant from the Space Telescope Science Institute. The data presented herein were obtained at the W.M. Keck Observatory, which is operated as a scientific partnership among the California Institute of Technology, the University of California and the National Aeronautics and Space Administration. The Observatory was made possible by the generous financial support of the W.M. Keck Foundation. The authors wish to recognize and acknowledge the very significant cultural role and reverence that the summit of Mauna Kea has always had within the indigenous Hawaiian community. We are most fortunate to have the opportunity to conduct observations from this mountain.

5.8 Appendix: Ratio of Averages versus Average of Ratios

Throughout the paper, we stack 24 μm images and calculate average $\mathrm{SFR}_{\mathrm{H}\alpha,\mathrm{H}\beta}$ in bins of metallicity, O_{32}, mass, and age. It is important to note that an average of ratios, i.e. $\langle \frac{L_{7.7}}{\mathrm{SFR}_{\mathrm{H}\alpha,\mathrm{H}\beta}} \rangle$, and a ratio of averages, i.e. $\frac{\langle L_{7.7} \rangle}{\langle \mathrm{SFR}_{\mathrm{H}\alpha,\mathrm{H}\beta} \rangle}$, are not necessarily equal (e.g., Brown 2011). Our method to compute the average of ratios is as follows.

First, we construct an inverse-$\mathrm{SFR}_{\mathrm{H}\alpha,\mathrm{H}\beta}$-weighted average of 24$\mu$m images:

$$\langle f_{24}\rangle_{\mathrm{w}} = \frac{\sum_i \frac{f_{24,i}}{\psi_i}}{\sum_i \frac{1}{\psi_i}} \ , \tag{5.1}$$

where ψ is $\mathrm{SFR}_{\mathrm{H}\alpha,\mathrm{H}\beta}$. We need to measure $\langle f_{24}\rangle_{\mathrm{w}}$ so that we can fit 24 μm flux densities to the CE01 IR templates and extract $\langle L_{7.7}\rangle_{\mathrm{w}}$, as follows. We calculate an inverse-$\mathrm{SFR}_{\mathrm{H}\alpha,\mathrm{H}\beta}$-weighted average of redshifts (i.e., $\frac{\sum_i z_i/\psi_i}{\sum_i 1/\psi_i}$), shift the IR templates to the weighted-average redshift, and find the best-fit template through a least-χ^2 method. $\langle L_{7.7}\rangle_{\mathrm{w}}$ is extracted from the best-fit model (see Section 5.2.6). Next, we calculate the weighted average of $\mathrm{SFR}_{\mathrm{H}\alpha,\mathrm{H}\beta}$:

$$\langle \psi\rangle_{\mathrm{w}} = \frac{\sum_i \frac{\psi_i}{\psi_i}}{\sum_i \frac{1}{\psi_i}} = \frac{N}{\sum_i \frac{1}{\psi_i}} \ , \tag{5.2}$$

where N is the total number of galaxies contributing to the stack. The ratio of $\langle L_{7.7}\rangle_{\mathrm{w}}$ to $\langle \psi\rangle_{\mathrm{w}}$ is mathematically equivalent to calculating the average of $L_{7.7}/\psi$ ratios ($\langle L_{7.7}/\psi\rangle$):

$$\frac{\langle L_{7.7}\rangle_{\mathrm{w}}}{\langle \psi\rangle_{\mathrm{w}}} = \frac{\sum_i \frac{L_{7.7,i}}{\psi_i}}{\sum_i \frac{1}{\psi_i}} \times \frac{\sum_i \frac{1}{\psi_i}}{N} = \frac{\sum_i \frac{L_{7.7,i}}{\psi_i}}{N} = \left\langle \frac{L_{7.7}}{\psi} \right\rangle \ . \tag{5.3}$$

The $L_{7.7}/\mathrm{SFR}_{\mathrm{H}\alpha,\mathrm{H}\beta}$ plots throughout the paper (e.g., Figure 5.3) and the corresponding values in Table 5.1 are derived according to Equation 5.3. In Figure 5.8, we repeat the analyses using the ratios of averages, $\langle L_{7.7}\rangle/\langle \mathrm{SFR}_{\mathrm{H}\alpha,\mathrm{H}\beta}\rangle$, by simply dividing the $L_{7.7}$ average stacks by the 3σ-clipped averages of $\mathrm{SFR}_{\mathrm{H}\alpha,\mathrm{H}\beta}$. For our sample, the ratio of averages and the average of ratios yield very similar results. The trends between the PAH intensity with metallicity, O_{32}, mass, and age are present regardless of the method adopted. Values of the $L_{7.7}$ stacks and the $\mathrm{SFR}_{\mathrm{H}\alpha,\mathrm{H}\beta}$ 3σ-clipped averages are also reported in Table 5.1.

As we do not have individual detections of objects in the PACS images, we cannot directly measure individual IR luminosities. As a result, we adopt a ratio of averages, i.e. $\langle L_{7.7}\rangle/\langle L_{\rm IR}\rangle$. As we demonstrated above with $\mathrm{SFR}_{\mathrm{H}\alpha,\mathrm{H}\beta}$, adopting this method is likely to yield similar results to computing the average of ratios. If anything, we speculate that $\langle L_{7.7}/L_{\rm IR}\rangle$ would result in a more significant trend between the PAH intensity and metallicity, compared to that of the $\langle L_{7.7}\rangle/\langle L_{\rm IR}\rangle$. This speculation is based on the fact that in the weighted average method, the low (or undetected) 24 μm images are up-weighted, as they tend to have low $\mathrm{SFR}_{\mathrm{H}\alpha,\mathrm{H}\beta}$ (high $1/\psi$), and hence, in low metallicity bins the average of $L_{7.7}/L_{\rm IR}$ ratios would be even lower than the ratio of averages.

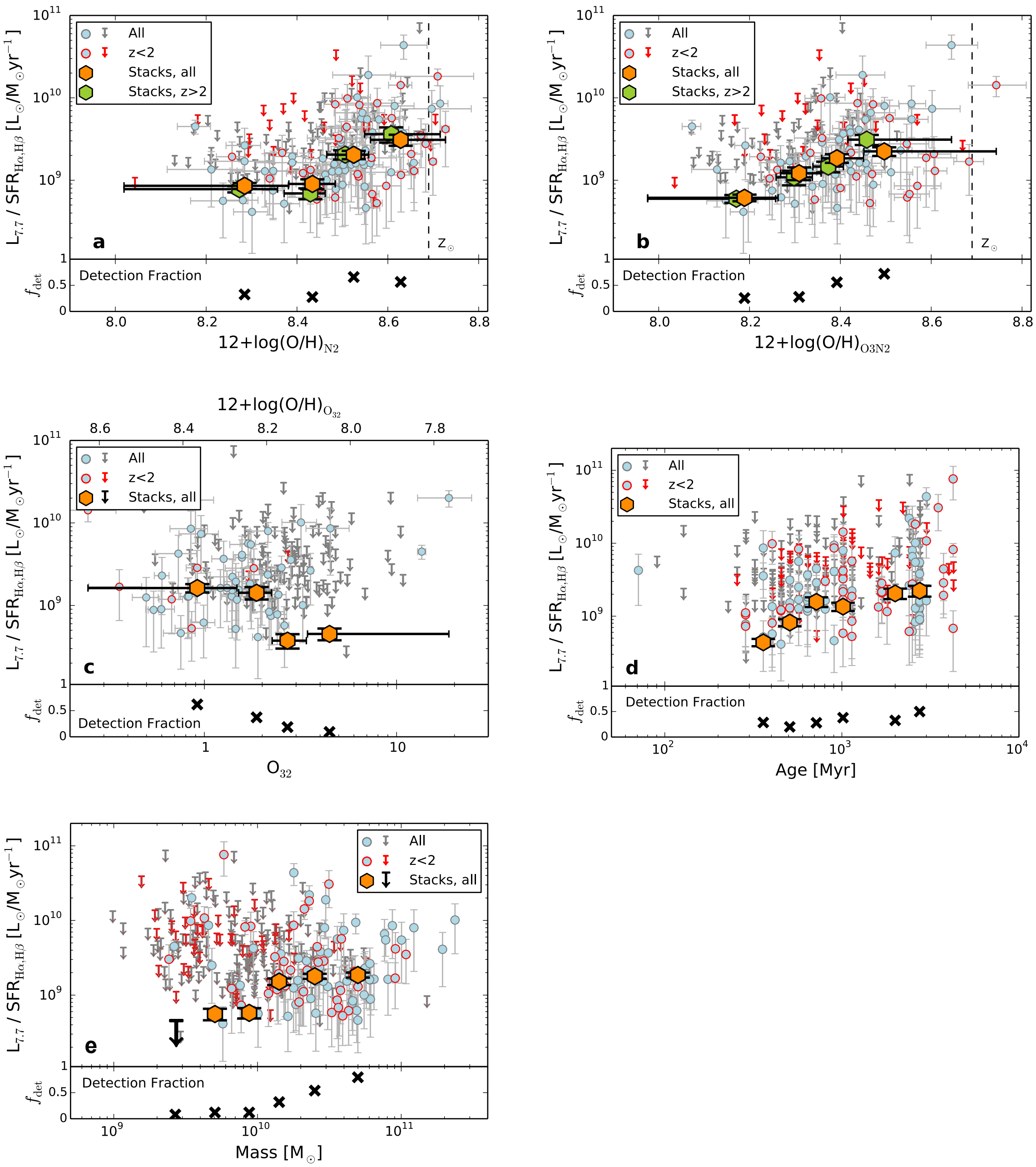

Figure 5.8 Ratio of $L_{7.7}$ to $\mathrm{SFR}_{\mathrm{H}\alpha,\mathrm{H}\beta}$ for individual galaxies (small circles and arrows) and for average stacks of $L_{7.7}$ to 3σ-clipped averages of $\mathrm{SFR}_{\mathrm{H}\alpha,\mathrm{H}\beta}$ (hexagons and arrows) as a function of (a) N2 metallicity, (b) O3N2 metallicity, (c) O_{32}, (d) age, and (e) mass. Note that in these plots the orange symbols are ratios of average quantities (refer to Appendix 5.8). The stacks and averages are in bins of the quantity on the horizontal axis.

Table 5.1 Properties of $L_{7.7}/\mathrm{SFR}_{\mathrm{H}\alpha,\mathrm{H}\beta}$ stacks

Parameter	Parameter Range	N	$\tilde{z}$	$\langle f_{24}\rangle$ [μJy]	$\langle L_{7.7}\rangle$ [10^9 L$_\odot$]	$\langle\mathrm{SFR}_{\mathrm{H}\alpha,\mathrm{H}\beta}\rangle$ [M$_\odot$ yr^{-1}]	$\langle L_{7.7}/\mathrm{SFR}_{\mathrm{H}\alpha,\mathrm{H}\beta}\rangle$ [10^8 L$_\odot/M_\odot$ yr^{-1}]
$12+\log(\mathrm{O/H})_{\mathrm{N2}}$	$8.04-8.37$	45	2.22	16.4 ± 0.8	31.9 ± 1.5	37 ± 3	6 ± 1
($N_{\mathrm{tot}}=185$)	$8.38-8.48$	47	2.23	13.8 ± 0.8	27.2 ± 1.5	30 ± 4	5 ± 2
	$8.48-8.56$	47	2.21	39.9 ± 0.9	74.6 ± 1.6	37 ± 4	29 ± 11
	$8.56-8.73$	46	2.17	52.0 ± 0.9	90.2 ± 1.5	29 ± 4	41 ± 15
$12+\log(\mathrm{O/H})_{\mathrm{O3N2}}$	$8.03-8.26$	42	2.22	10.8 ± 0.7	21.2 ± 1.3	35 ± 2	2.9 ± 0.7
($N_{\mathrm{tot}}=171$)	$8.27-8.35$	43	2.21	18.8 ± 0.8	35.9 ± 1.5	30 ± 5	7 ± 3
	$8.35-8.44$	43	2.26	28.4 ± 1.0	57.5 ± 2.1	31 ± 4	30 ± 9
	$8.44-8.74$	43	2.13	52.0 ± 1.0	86.4 ± 1.6	39 ± 5	35 ± 12
O_{32}	$0.23-1.46$	42	2.29	34.4 ± 1.1	72.7 ± 2.3	45 ± 5	26 ± 8
($N_{\mathrm{tot}}=170$)	$1.46-2.21$	43	2.29	17.3 ± 0.7	36.6 ± 1.5	26 ± 4	11 ± 3
	$2.22-3.28$	43	2.27	4.7 ± 0.7	9.9 ± 1.5	26 ± 3	4.8*
	$3.28-13.52$	42	2.29	4.1 ± 0.6	8.9 ± 1.2	20 ± 2	4.4*
$\log(M_*/M_\odot)$	$9.00-9.84$	98	2.22	0.9 ± 0.4	2.5*	9 ± 1	7*
($N_{\mathrm{tot}}=296$)	$9.84-10.04$	50	2.29	4.9 ± 0.6	10.8 ± 1	19 ± 2	11 ± 2
	$10.04-10.28$	50	2.23	16.0 ± 0.7	10.8 ± 1.3	31.3 ± 1	25 ± 4
	$10.29-10.52$	50	2.27	30.3 ± 0.8	31.3 ± 1.3	62.2 ± 2	32 ± 5
	$10.53-11.37$	48	2.24	69.5 ± 1.0	62.2 ± 1.8	130.9 ± 2	22 ± 3
Age [Myr]	$71-453$	49	2.27	6.5 ± 0.5	13.8 ± 1.1	30 ± 3	6 ± 1
($N_{\mathrm{tot}}=296$)	$453-570$	50	2.23	9.9 ± 0.6	19.4 ± 1.3	24 ± 2	10 ± 2
	$570-904$	50	2.29	12.6 ± 0.5	26.9 ± 1.1	17 ± 2	9 ± 3
	$904-1278$	50	2.16	18.1 ± 0.8	32.4 ± 1.4	24 ± 3	27 ± 11
	$1278-2600$	49	2.18	22.3 ± 1.0	41.0 ± 1.8	20 ± 3	22 ± 9
	$2600-4250$	48	2.24	34.9 ± 1.3	67.9 ± 2.5	29 ± 5	29 ± 12

Notes. Entries show properties of the stacks shown with orange symbols ($1.37\le z\le2.60$) in Figures 5.3 and 5.6. Each entry includes the parameter range, number of objects in each stack, median redshift, 24μm stacked flux density and its measurement uncertainty, rest-frame 7.7μm luminosity and its measurement uncertainty, 3σ-clipped mean $\mathrm{SFR}_{\mathrm{H}\alpha,\mathrm{H}\beta}$ and its error of the mean, and the average of $L_{7.7}/\mathrm{SFR}_{\mathrm{H}\alpha,\mathrm{H}\beta}$ ratios and its error. The latter should not be confused with the ratio of averages (refer to the text and Appendix 5.8).

* These object are undetected in the 24μm image stacks (before the aperture correction) and the values are 3σ upper limits.

Table 5.2 Properties of $L_{7.7}/L_{\rm IR}$ stacks

Parameter	Parameter Range	N	$\tilde{z}$	$\langle f_{24}\rangle$ [μJy]	$\langle f_{100}\rangle$ [μJy]	$\langle f_{160}\rangle$ [μJy]	$\langle L_{7.7}\rangle$ [10^9 L$_\odot$]	$\langle L_{\rm IR}\rangle$ [10^{10} L$_\odot$][a]	$\langle L_{7.7}\rangle/\langle L_{\rm IR}\rangle$
$12+\log({\rm O/H})_{\rm N2}$[b]	$8.02-8.47$	80	2.27	$12.4/pm0.5$	59 ± 30	472 ± 88	26 ± 1	12 ± 3	0.22 ± 0.05
($N_{\rm tot}=160$)	$8.47-8.55$	40	2.27	27.0 ± 0.9	347 ± 41	413 ± 126	56 ± 2	25 ± 4	0.22 ± 0.03
	$8.55-8.72$	40	2.30	34.0 ± 0.9	411 ± 51	486 ± 108	72 ± 2	26 ± 4	0.28 ± 0.04
$12+\log({\rm O/H})_{\rm O3N2}$	$7.98-8.35$	86	2.21	11.5 ± 0.4	199 ± 30	374 ± 98	22.3 ± 0.9	16 ± 3	0.14 ± 0.03
($N_{\rm tot}=172$)	$8.35-8.44$	43	2.26	26.6 ± 0.8	550 ± 50	454 ± 109	54 ± 2	30 ± 3	0.18 ± 0.02
	$8.44-8.74$	43	2.13	46.3 ± 0.9	616 ± 54	875 ± 110	77 ± 2	33 ± 3	0.24 ± 0.02
O_{32}	$0.25-1.46$	42	2.29	37.6 ± 0.8	329 ± 42	607 ± 105	79 ± 2	27 ± 3	0.29 ± 0.04
($N_{\rm tot}=171$)	$1.46-2.71$	65	2.27	10.8 ± 0.5	52 ± 36	441 ± 101	23 ± 1	11 ± 3	0.21 ± 0.06
	$2.71-18.71$	64	2.29	3.7 ± 0.4	286 ± 40	209 ± 81	8 ± 1	15 ± 2	0.05 ± 0.01
$\log(M_*/M_\odot)$	$8.26-9.6$	92	2.15	-3.2 ± 0.4	-125 ± 27	-281 ± 101	2.2*	8.9*	–
($N_{\rm tot}=476$)	$9.6-10$	137	2.20	4.7 ± 0.4	127 ± 27	247 ± 61	9.0 ± 0.7	10 ± 1	0.09 ± 0.02
	$10-10.6$	173	2.19	21.3 ± 0.5	261 ± 22	306 ± 63	39.5 ± 0.9	16 ± 2	0.24 ± 0.02
	$10.6-11.6$	74	2.19	69.4 ± 0.9	854 ± 38	1625 ± 102	121.7 ± 1.6	62 ± 3	0.20 ± 0.01
Age [Myr]	$71-570$	100	2.26	7.6 ± 0.4	172 ± 31	515 ± 84	15.8 ± 0.9	17 ± 3	0.09 ± 0.02
($N_{\rm tot}=299$)	$570-1278$	100	2.22	15.8 ± 0.5	291 ± 36	-166 ± 97	30.8 ± 1.0	10 ± 3	0.31 ± 0.11
	$1278-2600$	50	2.18	22.3 ± 1.0	318 ± 44	-88 ± 148	41.0 ± 1.8	15 ± 4	0.27 ± 0.07
	$2600-4250$	49	2.23	34.3 ± 1.3	263 ± 55	793 ± 131	65.8 ± 2.5	25 ± 5	0.26 ± 0.06

Notes. Entries show properties of stacks in Figures 5.4 and 5.6. Each entry includes the parameter range, number of objects in each bin, median redshift, 24μm, 100μm, and 160μm stacked flux densities and their measurement uncertainties, rest-frame 7.7μm luminosity and its measurement uncertainty, $L_{\rm IR}$ and its uncertainty, and ratio of stacked $L_{7.7}$ to stacked $L_{\rm IR}$ and its error.

* Stacks are undetected in 24μm, 100μm, and 160μm, and hence, $L_{7.7}$ and $L_{\rm IR}$ are 3σ upper limits. $L_{7.7}/L_{\rm IR}$ is meaningless in this case.

[a] $L_{\rm IR}$ is derived from f_{100} and f_{160} fit to CE01 templates. Its error is the standard deviation of 10,000 $L_{\rm IR}$ realizations that are calculated by fitting IR templates to the perturbed f_{100} and f_{160}. If both f_{100} and f_{160} are undetected we used upper limits, but if only one is undetected we used the flux and its error to find the best-fit model and the associated $L_{\rm IR}$.

[b] N2 stacks are limited to objects at $2.0\leq z\leq2.6$, because otherwise the highest metallicity bin is dominated by low-z galaxies with $\hat{z}\sim1.6$. The rest of the stacks (O3N2, O_{32}, M_*) include all objects at $1.37\leq z\leq2.60$. The median redshifts in these bins are consistent and are above 2. We should note that O_{32} sample has only 8 galaxies with $z<2.0$.

Chapter 6

The MOSDEF Survey: Direct Observational Constraints on the Ionizing Photon Production Efficiency, $\xi_{\rm ion}$, at $z \sim 2$*

Abstract We utilize spectroscopic measurements of Hα and Hβ for a large sample of 672 galaxies from the MOSFIRE Deep Evolution Field survey to constrain ionizing photon production efficiencies ($\xi_{\rm ion}$) at $z = 1.4 - 2.6$. We find that $\xi_{\rm ion}$ is elevated in galaxies with intense radiation fields (i.e., high [OIII]/[OII] and high [OIII]/Hβ) and low oxygen abundances (low [NII]/Hα). However, $\xi_{\rm ion}$ does not change with the offset from the BPT $z \sim 0$ star-forming locus, suggesting no change in the hardness of ionizing radiation with the offset

*A version of this chapter is submitted to *The Astrophysical Journal*

from the $z \sim 0$ sequence. Galaxies with blue UV spectral slopes ($\beta \lesssim -2.0$) have elevated $\xi_{\rm ion}$. If this is the case at $z > 6$, then it would imply that these galaxies need an average Lyman continuum escape fraction of $(14 \pm 4)\%$ to maintain cosmic reionization, a value that is lower than that commonly assumed in reionization models. We constrain the scatter in $\xi_{\rm ion}$ and conclude that the large scatter of 0.29 dex cannot be solely explained by measurement uncertainties or variations in the assumed dust attenuation curve. Rather, our results imply that the scatter is dominated by galaxy-to-galaxy variations in the stellar population properties, including the slope and upper mass cutoff of the initial mass function, stellar metallicity, star formation burstiness, and binary/single star evolution. We demonstrate that even with robustly dust-corrected Hα measurements, the UV dust attenuation curve is an important source of uncertainty that on average can cause a ~ 0.3 dex systematic uncertainty in $\xi_{\rm ion}$ measurements. Our results demonstrate the advantages and disadvantages of using Balmer emission lines in constraining $\xi_{\rm ion}$ for future observations with the *James Webb Space Telescope* to investigate the redshift evolution of $\xi_{\rm ion}$ and its role in the reionization era.

6.1 Introduction

Star-forming systems dominate the galaxy population at $z \gtrsim 1.5$, both in number and mass density (Madau & Dickinson 2014). The light emitted from these galaxies is largely dominated by massive stars, either in the form of non-ionizing UV and re-processed IR emission, or in the form of nebular emission lines emitted from the gas ionized by such stars. Therefore, our understanding of galaxy evolution is intimately tied to the physics of massive stars and the surrounding gas that is ionized by their radiation.

An important parameter that is determined by the population of massive stars is the galaxy hydrogen-ionizing photon production rate. The emission rate of ionizing photons impacts our measurements derived from nebular lines, such as star-formation rates (SFRs) and gas-phase metallicities. The production rate of Lyman-continuum (LyC) ionizing photons per unit UV continuum luminosity, usually measured at 1500 Å, is called the ionizing photon production efficiency, $\xi_{\rm ion}$ (e.g., Robertson et al. 2013).

$\xi_{\rm ion}$ depends on the ionizing photon production rate of hot massive stars, and the relative number of such stars to the non-ionizing stars. The relative number of massive ionizing stars is impacted by the initial mass function (IMF), star formation history, and age of the galaxy. Additionally, the ionizing photon production rate is dependent on the massive stars metallicity, binarity, and rotation (e.g., Stanway et al. 2016; Choi et al. 2017). Hence, determining $\xi_{\rm ion}$ helps us to place constraints on the massive stellar populations in high-redshift galaxies and improve our knowledge of galaxy evolution and stellar population synthesis (SPS) models. Additionally, $\xi_{\rm ion}$ is an important input in models of cosmic reionization and plays an important role in identifying galaxies as the responsible source of reionization (e.g., Bouwens et al. 2015; Robertson et al. 2015).

In high-redshift studies, $\xi_{\rm ion}$ is often *predicted* either solely from SPS models (e.g., Madau et al. 1999) or by correlating the observed UV continuum slope β with the predictions from SPS models considering a variety of metallicity, age, and dust content (e.g., Robertson et al. 2013; Bouwens et al. 2015; Duncan & Conselice 2015). The "canonical" $\xi_{\rm ion}$ value

($\log(\xi_{\rm ion}/{\rm erg\,Hz^{-1}}) \sim 25.2 - 25.3$) is derived from these indirect estimates. One direct way of measuring $\xi_{\rm ion}$ is by modeling UV spectra and determining $\xi_{\rm ion}$ either from the UV metal lines (Stark et al. 2015, 2017) or by evaluating the ratio of ionizing to non-ionizing fluxes (f_{900}/f_{1500}, Reddy et al. 2016b). The main advantage of these methods is that they are less sensitive to uncertainties in dust attenuation corrections. However, they require deep rest-UV spectroscopy, and the results rely either on individual extreme objects at high redshifts (Stark et al. 2017) or on the composite spectrum of a large number of galaxies (Reddy et al. 2016b). In both cases, statistical information on galaxy-to-galaxy variations of $\xi_{\rm ion}$ in large samples is missed.

Another way of measuring $\xi_{\rm ion}$ that enables us to constrain its value for individual galaxies is by using nebular recombination lines, e.g. Hα. In an ionization-bounded nebula, the rate of recombinations balances the rate of ionizing photons with energies above 13.6 eV that are either emitted from the star or produced during recombination to the hydrogen ground level. There are a number of existing studies that used Balmer emission lines to estimate $\xi_{\rm ion}$ at high redshifts. For example, Bouwens et al. (2016a) estimated $\xi_{\rm ion}$ using Hα measurements at $z \sim 4-5$ based on *Spitzer*/IRAC photometry. Nakajima et al. (2016) used Keck/MOSFIRE spectra of Hβ for a sample of 15 galaxies at $z = 3.1 - -3.7$ that included a few candidate LyC leakers on the basis of ground-based imaging. The recent study of Matthee et al. (2017) used Hα for large sample of narrow-band selected Hα and Lyman-α emitters to constrain $\xi_{\rm ion}$ at $z = 2.2$. Despite the advancement of using a single Balmer line to directly measure Lyman continuum photon production rate, these studies did not have access to additional Balmer lines to correct for dust (Bouwens et al. 2016a; Matthee et al.

2017; Nakajima et al. 2016). Moreover, they either relied on small sample sizes (Nakajima et al. 2016), or the ones with large samples did not have spectroscopic measurements of the lines (Bouwens et al. 2016a; Matthee et al. 2017). A detailed and thorough study of $\xi_{\rm ion}$ requires large and representative samples with spectroscopic Hα and Hβ observations to directly measure nebular line luminosity and properly correct for dust.

In this study, we use data from the MOSFIRE Deep Evolution Field (MOSDEF) survey (Kriek et al. 2015), where near-IR spectra with coverage of Hβ and Hα for a representative sample of 672 galaxies at $1.37 \leq z \leq 2.61$ are available. Access to both Hα and Hβ spectroscopic measurements enables us to measure robustly dust-corrected Hα luminosities (Reddy et al. 2015; Shivaei et al. 2015b; Shivaei et al. 2016) and ionizing photon production rates. Moreover, the wealth of rest-optical emission lines that are accessible through MOSDEF (e.g., [OII], [OIII], [NII]) helps us to study trends of $\xi_{\rm ion}$ with other commonly measured properties of galaxies, such as gas-phase metallicity and ionization parameter (Shapley et al. 2015; Sanders et al. 2015, 2016a). Our sample is further accompanied by the rich 3D-*HST* photometry dataset (Skelton et al. 2014) that aids in modeling the stellar populations (e.g., stellar reddening and stellar mass). The main goals of this study are a) to explore the variations of $\xi_{\rm ion}$ with galaxy global properties, ISM characteristics, and redshift, b) to explore the origin of the observed scatter in the $\xi_{\rm ion}$ distribution of galaxies, and c) to provide an observationally constrained canonical $\xi_{\rm ion}$ value for typical star-forming galaxies at $z \sim 2$.

The layout of the paper is as follows. In Section 6.2, we introduce the MOSDEF survey and our methods of line measurements and SED fitting. In Section 6.3, we describe details of $\xi_{\rm ion}$ measurements for individual galaxies and average values from composite spectra. We show in Section 6.4 the relationship between $\xi_{\rm ion}$ and UV continuum slope, UV magnitude, line ratios that are tracers of gas-phase metallicity and the hardness and intensity of ionization field, stellar mass, and redshift. We outline a detailed discussion on the potential sources of the large scatter in $\xi_{\rm ion}$ measurements in Section 6.5. Our results are summarized in Section 6.6. Throughout this paper, line wavelengths are presented in vacuum and magnitudes are given in the AB system (Oke & Gunn 1983). We assume a Chabrier (2003) IMF. A cosmology with $H_0 = 70\,{\rm km s^{-1} Mpc^{-1}}, \Omega_\Lambda = 0.7, \Omega_{\rm m} = 0.3$ is adopted.

6.2 Data and Measurements

6.2.1 The MOSDEF Survey

The recently-completed MOSDEF survey was a four-year near-IR spectroscopic survey that used the Keck/MOSFIRE spectrograph (McLean et al. 2012) to study the properties of $\sim$ 1500 galaxies and AGN at $1.4 \leq z \leq 3.8$ in the five CANDELS fields: AEGIS, COSMOS, GOODS-N, GOODS-S, and UDS (Grogin et al. 2011; Koekemoer et al. 2011). The fields were also covered by the *Hubble Space Telescope* (*HST*)/WFC3 grism observations of the 3D-*HST* survey (Skelton et al. 2014; Momcheva et al. 2016). The MOSDEF parent sample was selected down to $H = 24.0$, 24.5, and 25.0 at $z = 1.37 - 1.70$, $2.09 - 2.61$, and $2.95 - 3.80$, respectively. For the details of the survey, observing strategy, and data reduction refer to Kriek et al. (2015).

In this paper, we remove objects with AGN contamination based on their X-ray emission, IRAC colors (using the Donley et al. 2012 criteria), and optical line ratios derived from the MOSDEF spectra ([NII]/Hα> 0.5; Coil et al. 2015; Azadi et al. 2017).

6.2.2 Line Luminosities and Nebular Dust Correction

Emission line fluxes are estimated by fitting Gaussian functions to the 1D spectra, where the uncertainties are derived by perturbing the spectrum of each object according to its error spectrum and measuring the line fluxes in the perturbed spectra (Kriek et al. 2015; Reddy et al. 2015). Slit loss corrections are applied by normalizing the spectrum of a star in each observing mask to match the 3D-*HST* total photometric flux (Skelton et al. 2014). Additionally, we use the *HST* images of our resolved galaxy targets to estimate and correct for differential flux loss relative to that of the star (Kriek et al. 2015).

We correct Hα and Hβ fluxes for underlying Balmer absorption, determined from the best-fit SED models (Section 6.2.3). To correct the nebular line luminosities for dust attenuation, we calculate the Balmer decrement (Hα/Hβ) and assume the Cardelli et al. (1989) galactic extinction curve (Reddy et al. 2015; Shivaei et al. 2015b; Shivaei et al. 2016).

6.2.3 SED Fitting and Stellar Dust Correction

We fit UV to near-IR photometry from 3D-*HST* (Skelton et al. 2014; Momcheva et al. 2016), corrected for emission line contamination according to the MOSDEF spectra, with Bruzual & Charlot (2003, BC03) models through a minimum χ^2 method to find the best-fit models and derive stellar masses and stellar color-excesses (Reddy et al. 2015). For our models, we assume a Chabrier (2003) IMF, an exponentially rising star formation history (as was shown to best reproduce the observed SFRs at $z \sim 2$, Reddy et al. 2012b), and two combinations of metallicities and attenuation curves: a solar metallicity with the Calzetti et al. (2000) curve as it is commonly assumed in high-redshift studies, and a sub-solar ($0.2\,Z_\odot$) with an SMC curve (Gordon et al. 2003) motivated by recent studies that suggested a steeper attenuation curve with a sub-solar metallicity ($\sim 0.14-0.20\,Z_\odot$) is more applicable to galaxies at high redshifts (Capak et al. 2015; Bouwens et al. 2016b; Reddy et al. 2017). We measure stellar $E(B-V)$ and UV luminosity (L_ν) at 1500 Å from the best-fit SED models. UV slope (β) is measured by fitting a power law ($f_\lambda \propto \lambda^\alpha$) to the photometry at rest-wavelengths $1268 - 2580$ Å.

6.3 Measurement of $\xi_{\rm ion}$

The LyC production efficiency is defined as the ratio of the production rate of ionizing photons ($N(\rm H^0)$) in units of $\rm s^{-1}$ to UV continuum luminosity density in units of $\rm erg\,s^{-1}\,Hz^{-1}$:

$$\xi_{\rm ion} = \frac{N(\rm H^0)}{L_{\rm UV}}\ [\rm s^{-1}/erg\,s^{-1}\,Hz^{-1}]. \tag{6.1}$$

For an ionization bounded nebula, where the rate of recombination balances the rate of ionizing photons, one can convert Hα luminosity to the production rate of LyC photons. This conversion mainly depends on the nebular conditions, including electron density, number density of ionized hydrogen, and gas temperature (Spitzer 1978; Osterbrock 1989), and hence is not sensitive to the choice of stellar population model. Based on

Leitherer & Heckman (1995), the conversion is:

$$L(\text{H}\alpha)\ [\text{erg}\,\text{s}^{-1}] = 1.36 \times 10^{-12} N(\text{H}^0)\ [\text{s}^{-1}]. \tag{6.2}$$

An important assumption in calculating the LyC photon production rate based on the observed Hα luminosity is the amount of dust attenuation of ionizing photons internal to H II regions. Using a sample of seven local galaxies, Inoue (2002) concluded that the dust optical depth of LyC photons in H II regions is almost equal to the dust optical depth of the diffuse ISM [1]. On the other hand, at $z \sim 2$, Reddy et al. (2016a) used rest-UV spectroscopy and showed that photoelectric absorption dominates the depletion of ionizing photons. As the results of Reddy et al. (2016a) were based on a sample with a similar redshift range to ours, we follow their conclusion and assume negligible dust attenuation of ionizing photons internal to H II regions.

The other uncertainty in the Hα-derived production rate of ionizing photons is the escape fraction of LyC photons (f_{esc}). A non-zero f_{esc} implies a larger intrinsic ξ_{ion} by $\frac{1}{(1-f_{\text{esc}})}$ with respect to the measured ξ_{ion} based on Hα luminosity. We assume the relation between covering fraction of neutral hydrogen (f_{cov}) and $E(B-V)$ from Reddy et al. (2016b) to estimate f_{esc} (i.e., $1 - f_{\text{cov}}$) from our SED-inferred $E(B-V)$. For the nine galaxies in our entire sample where $E(B-V) = 0$ (four, if we use an SMC curve with 0.2 solar metallicity), we set $f_{\text{esc}} = 0.4$, which is the maximum value of the sample, to avoid an unrealistic escape fraction of 100%. Assuming the Calzetti (SMC) attenuation curve for the

[1] If we assume that the gas-to-dust ratio in our galaxies is similar to that of the local star-forming regions used in the Inoue (2002) study (an assumption that is not necessarily correct), their result implies that $\sim 30\%$ of LyC photons in our MOSDEF galaxies with $\langle E(B-V)\rangle \sim 0.2$, are depleted by dust attenuation internal to H II regions, which increases ξ_{ion} by ~ 0.1 dex.

SED models, the average $f_{\rm esc}$ for the full sample is 0.04 (0.09). We correct the measured $\xi_{\rm ion}$ values on an individual galaxy-by-galaxy basis accordingly.

In practice, we have to correct the unobscured Hα and UV luminosities for dust attenuation before applying Equations 6.1 and 6.2. There are a number of studies in the literature that examined measurements of UV and optical attenuation for stellar and nebular emission at high redshifts (Noll et al. 2009; Wild et al. 2011; Reddy et al. 2012b, 2015; Shivaei et al. 2015a; De Barros et al. 2016; Shivaei et al. 2016, among many more). To correct for nebular attenuation, it is favored to use Balmer decrement with an assumption of the Cardelli et al. (1989) galactic extinction curve (Calzetti et al. 2000; Steidel et al. 2014; Reddy et al. 2015; Shivaei et al. 2016). The dust-corrected Hα luminosity would increase on average by ~ 0.06 dex if we use the Calzetti et al. (2000) curve instead of the Cardelli et al. (1989) curve. Estimating the stellar UV dust attenuation is more uncertain. As mentioned in Section 6.2.3, we use $E(B-V)$ from the best-fit SED models with the assumption of the Calzetti+solar metallicity or the SMC+sub-solar metallicity. The effect of UV dust attenuation on $\xi_{\rm ion}$ is discussed in Section 6.4.4.

6.3.1 Composite Measurements

In Section 6.4, in order to include Hβ undetected galaxies in our analysis we use a stacking technique to derive average $\xi_{\rm ion}$ values in bins of galaxy parameters [2], as follows. Individual spectra are shifted to the rest-frame with a wavelength grid of $\delta\lambda = 0.5$ Å. Parts of the individual spectra where the ratio of the error spectra to the median error is greater than 3 are removed, as they are dominated by sky lines. The composite spectrum is created

[2]Source code is available at: https://github.com/IreneShivaei/specline

by taking the mean (or mean weighted by the error spectra) of the luminosities of individual spectra contributing to the stack in each wavelength bin. The composite error spectrum is estimated as the uncertainty on the weighted mean (i.e., $\frac{1}{\sqrt{\sum_i \sigma_i^2}}$, where σ_i^2 is the variance).

We fit the composite Hα, Hβ, [OIII], and [NII] lines with single Gaussian profiles and the [OII] line with a double Gaussian profile. We estimate the composite line errors by perturbing the stacked spectrum within the composite error spectrum for 1000 times. The Hα and Hβ composite lines are corrected for Balmer absorption using the mean absorption of the individual galaxies contributing to the stack, inversely weighted by individual flux uncertainties.

To derive Balmer decrements, we normalize individual spectra to their Hα luminosities before making the composite spectrum and take the inverse value of the normalized composite Hβ line as the mean Hα/Hβ ratio. In a similar manner, we measure the UV-normalized Hα luminosity to derive the observed (uncorrected for dust) Hα/UV ratio, which is required in Equations 6.1 and 6.2. The [OIII]/Hβ and [OIII]/[OII] stacks for the Hβ and [OII] undetected galaxies, respectively, are also measured from the [OIII]-normalized composite spectra.

6.4 $\xi_{\rm ion}$ Evolution with Galaxies Properties and Redshift

In this section, we evaluate the variations of $\xi_{\rm ion}$ as a function of galaxies' stellar (Section 6.4.1) and gas properties (Section 6.4.2). We also discuss the evolution of $\xi_{\rm ion}$ with

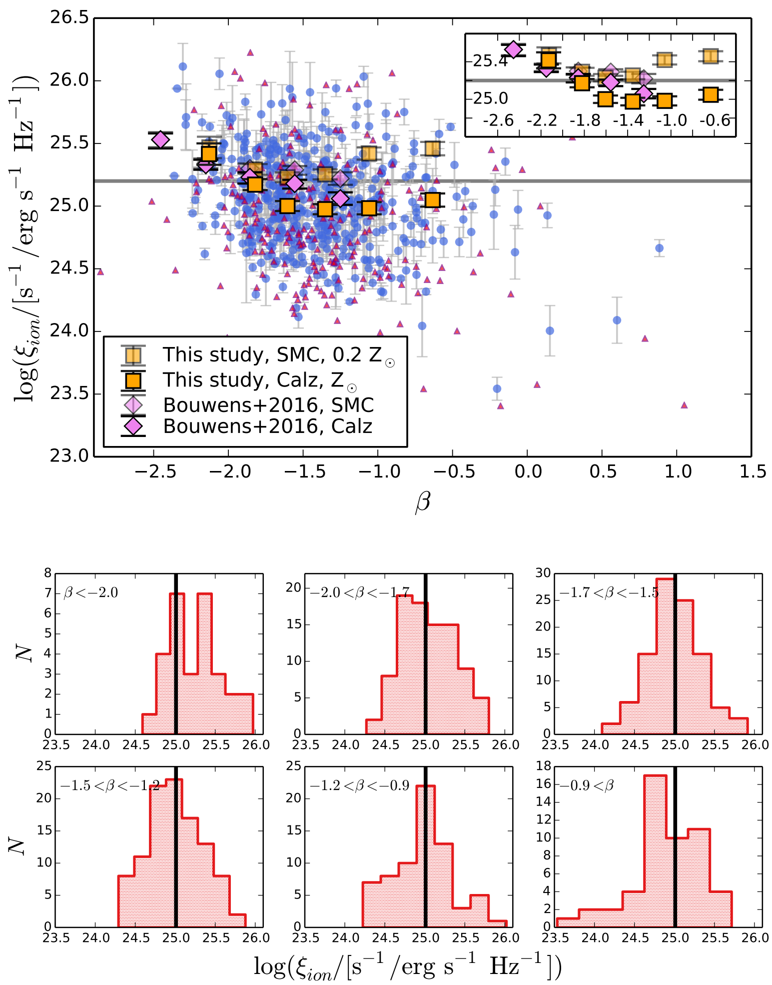

Figure 6.1 (*Top:*) production efficiency of ionizing photons as a function of UV continuum slope, β. Small blue circles and red upward triangles show individual measurements of $\xi_{\rm ion}$ for the Hα-Hβ detected sample, and $3\,\sigma$ lower limit for the Hβ-undetected sample, respectively. In the individual measurements we use a Calzetti curve and a solar metallicity to dust-correct the UV luminosity (Equation 6.1). We use a Cardelli attenuation curve for nebular dust correction. Orange squares are stack measurements of $\xi_{\rm ion}$ in bins of β for the full sample (detected and undetected Hβ). Solid orange stacks assume the Calzetti curve with a solar metallicity for UV dust correction, and light orange stacks assume an SMC curve with sub-solar ($0.2\,Z_\odot$) metallicity. The assumption of a sub-solar metallicity leads to a bluer intrinsic UV slope, β_0. Also shown is the result of Bouwens et al. (2015) study of $z = 3.8 - 5.0$ galaxies in solid and light violet diamonds for the Calzetti and SMC curves with a solar metallicity ($\beta_0 = -2.23$), respectively. As they did not have Hβ measurements, Bouwens et al. (2015) used stellar reddening and the same attenuation curve for both nebular Hα and stellar UV luminosities. The horizontal line shows $\log(\xi_{\rm ion}/[{\rm s}^{-1}/{\rm erg\,s}^{-1}\,{\rm Hz}^{-1}]) = 25.2$ from Robertson et al. (2013). (*Botton:*) distribution of $\xi_{\rm ion}$ for the sample of Hα-Hβ detected galaxies in six bins of β shown in the top plot. $\xi_{\rm ion}$ is measured using the Calzetti curve. It is clear that $\xi_{\rm ion}$ is elevated in our bluest galaxies.

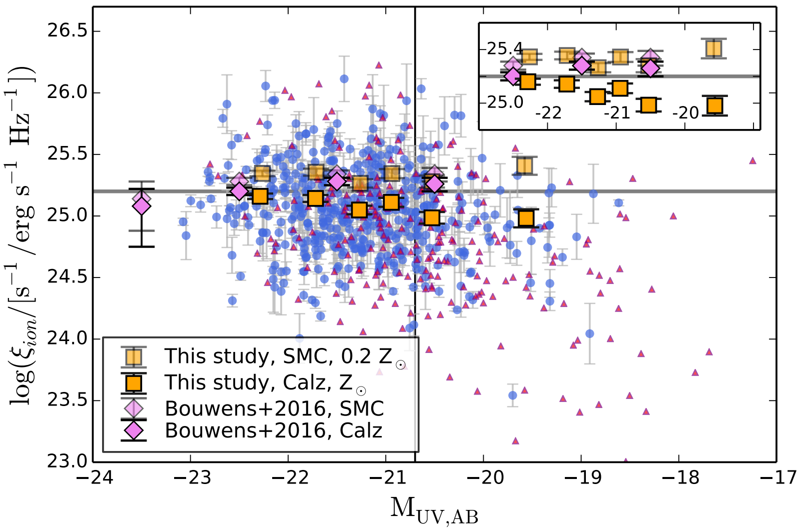

Figure 6.2 Dependence of $\xi_{\rm ion}$ on UV absolute magnitude. The symbols are the same as in Figure 6.1. The vertical line shows the characteristic UV magnitude at $1.9 \leq z < 2.7$ from Reddy & Steidel (2009).

redshift and stellar mass (Section 6.4.3), and the systematic uncertainties associated with the assumed dust attenuation curve (Section 6.4.4).

6.4.1 $\xi_{\rm ion}$ and UV properties, implications for reionization

In high-redshift studies, the UV continuum slope (β) is often used as a proxy for the ionizing photon production efficiency (e.g., Robertson et al. 2013; Duncan & Conselice 2015), mainly because rest-frame UV is shifted to longer optical wavelengths and it is easily accessible through ground based observations across a large range of redshift. Here, we have an independent measure of $\xi_{\rm ion}$ using nebular emission lines and can investigate the correlation between $\xi_{\rm ion}$ and β.

In the top panel of Figure 6.1, we show the relation between $\xi_{\rm ion}$ and β for our sample (orange squares, $z = 1.4 - 2.6$) and for the higher-redshift sample of Bouwens et al.

(2016a, violet diamonds, $z = 3.8 - 5.0$).[3] The solid and light symbols correspond to the Calzetti and SMC curves assumptions for UV attenuation correction, respectively. We will discuss the discrepancy between the two assumed attenuation curves later in Section 6.4.4. Based on the Calzetti points, $\xi_{\rm ion}$ is constant at $\beta \gtrsim -1.6$, and there is a significant increase of $\xi_{\rm ion}$ by ~ 0.5 dex in the bluest bin with $\beta = -2.1$. The increase is consistent with the higher-redshift results of Bouwens et al. (2016a). On the bottom panel of Figure 6.1, we also show the $\xi_{\rm ion}$ distribution in bins of β with the vertical black line indicating the average of the full sample. It is clear that $\xi_{\rm ion}$ distribution shifts to lower values proceeding to larger β's.

Studies of cosmic reionization struggle to show whether faint galaxies at $z > 6$ have high enough escape fractions to maintain reionization (e.g., Vanzella et al. 2010; Siana et al. 2015). If the galaxies with the bluest β ($\langle\beta\rangle = -2.1$) in our sample are similar to faint galaxies at $z > 6$, their elevated $\xi_{\rm ion}$ of $\log(\xi_{\rm ion}/[{\rm s^{-1}/erg\,s^{-1}\,Hz^{-1}}]) = 25.42 \pm 0.09$, compared to the "canonical" $\xi_{\rm ion}$ value of 25.20 that is commonly assumed in reionization models (Robertson et al. 2013), implies that a lower escape fraction of ionizing photons is needed for galaxies to reionize the universe (see Robertson et al. 2013, 2015; Bouwens et al. 2016a; Stanway et al. 2016). Even without the assumption of the $E(B-V)$-based $f_{\rm esc}$ (see Section 6.3), $\xi_{\rm ion}$ in the bluest bin is 25.34 ± 0.08 for the Calzetti curve and 25.39 ± 0.08 for an SMC curve, which is ~ 0.17 dex larger than the Robertson et al. (2013) assumed value.

Based on the constraints on the Thomson scattering and ionized hydrogen filling factor at $z = 6 - 9$ from CMB observations, Bouwens et al. (2015) estimated the evolution

[3] The Bouwens et al. (2016a) study did not have Hβ measurements and corrected their photometry-based Hα luminosities using stellar $E(B-V)$, assuming a similar reddening towards nebular and stellar regions.

of the cosmic ionizing emissivity. The cosmic ionizing emissivity, or the number density of ionizing photons per second capable of reionizing hydrogen in the IGM, $\dot{N}_{\rm ion}$, is a product of three terms: the total UV luminosity density $\rho_{\rm UV}$, $\xi_{\rm ion}$, and the fraction of the ionizing photons that escape into the IGM, $f_{\rm esc}$. Bouwens et al. (2015) compared the observationally-constrained evolution of $\dot{N}_{\rm ion}$ with the evolution of the UV luminosity density integrated down to $M_{\rm UV} = -13$ and concluded that in order for galaxies to reionize the IGM with a clumping fraction of $C_{\rm HII} = 3$, we need to have $\log(f_{\rm esc}\xi_{\rm ion}) = 24.50 \pm 0.1$. Using this constraint and our $\xi_{\rm ion}$ value at $\beta = -2.1$ (without the assumption of $E(B-V)$-derived $f_{\rm esc}$), we evaluate an escape fraction of 0.14 ± 0.04, which is consistent with the low LyC escape fraction observed in $z \sim 2-4$ galaxies (e.g., Chen et al. 2007; Nestor et al. 2013; Siana et al. 2015; Grazian et al. 2017; Japelj et al. 2017). Simulations also predict a low ($\lesssim 0.05$) time-averaged $f_{\rm esc}$ due to large time variability of $f_{\rm esc}$ (e.g., Ma et al. 2015).

We also show $\xi_{\rm ion}$ as a function of UV magnitude in Figure 6.2 for both the Calzetti and SMC curves with points from the higher redshift study of Bouwens et al. (2016a) included. As evident, we do not see any trend between $\xi_{\rm ion}$ and UV luminosity. $\xi_{\rm ion}$ is constant for galaxies below and above the characteristic UV magnitude at $1.9 \leq z < 2.7$, $M^*_{\rm AB} = -20.70$ (Reddy & Steidel 2009).

6.4.2 $\xi_{\rm ion}$ and ISM properties: O_{32} and BPT diagram

The ionizing photon production efficiency, by definition, depends on the hardness and intensity of the source radiation field. In MOSDEF, we have the leverage of access to multiple rest-optical emission lines whose ratios give us an independent way of constraining

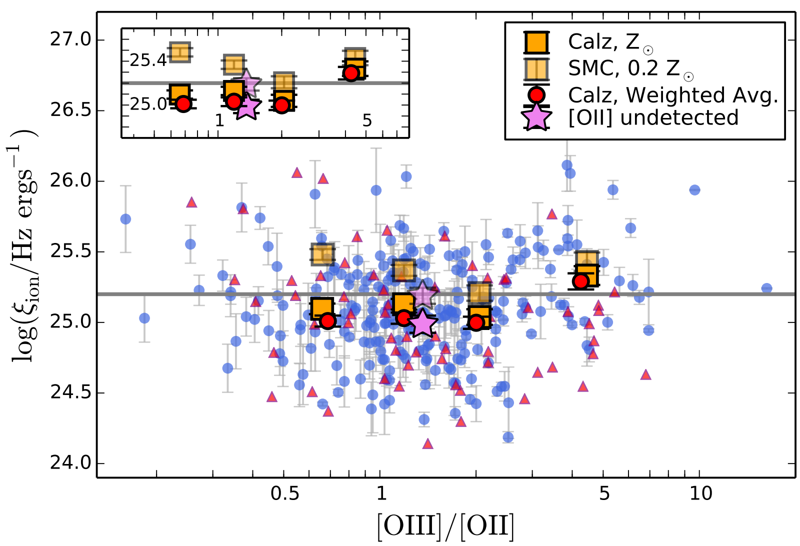

Figure 6.3 Dependence of $\xi_{\rm ion}$ on [OIII]/[OII] ratio. The orange and blue symbols are the same as in Figure 6.1 for the sample of Hα, [OIII], and [OII] detected galaxies. Red circles show weighted averages of only the Hα-Hβ detected sample (the blue individual points), which are consistent with the orange stacks that include Hβ-undetected galaxies as well. The violet star is the stack of undetected [OII] objects ([OIII] detected), which does not display a higher $\xi_{\rm ion}$ compared to the rest of the stacks. The horizontal line shows $\log(\xi_{\rm ion}/[{\rm s^{-1}/erg\,s^{-1}\,Hz^{-1}}]) = 25.2$ from Robertson et al. (2013).

the source ionizing radiation. In this section, we investigate the change of $\xi_{\rm ion}$ as a function of [OIII]/[OII] ratio (O_{32}), [OIII]/Hβ ratio (O3), and across the BPT diagram (Baldwin et al. 1981).

As [OIII] and [OII] are from the same element but with different ionization potentials, O_{32} is used as an empirical proxy for ionization parameter. In Figure 6.3, we show the relation between $\xi_{\rm ion}$ and O_{32}. In the Calzetti stacks, $\xi_{\rm ion}$ is constant at $O_{32} \lesssim 3$ and increases by $\sim 70\%$ at $O_{32} \sim 5$. This increase is significant at the $> 3\,\sigma$ level. High O_{32} indicates high ionization parameter (Penston et al. 1990), and hence a high ionizing photon production efficiency. High O_{32} may also be indicative of a density-bounded HII region (see e.g., Nakajima & Ouchi 2014; Trainor et al. 2016), where the star-forming cloud is completely ionized and its radius is determined by the gas distribution and not the ionization equilibrium. In a density-bounded nebula the outer layer with lower ionization species that produce [OII] is reduced, but the higher ionization [OIII] zone that form preferentially at the inner radii of the HII region is unaffected. Consequently, the ratio of [OIII]/[OII] in a density-bounded nebula is larger than that of an ionization-bounded nebula. On the other hand, a density-bounded nebula would have a higher leakage of ionizing photons (high $f_{\rm esc}$) compared to an ionization-bounded nebula (see Giammanco et al. 2005; Jaskot & Oey 2013; Nakajima & Ouchi 2014). In that case, a fraction of ionizing photons emitted from the source escape the nebula before producing recombination lines. As a result, if the high O_{32} ratios are to some extent associated with density-bounded systems, their intrinsic $\xi_{\rm ion}$ is even higher than that inferred from Hα.

The trend of $\xi_{\rm ion}$ with O_{32} is different in the SMC stacks compared to the Calzetti stacks. $\xi_{\rm ion}$ assuming an SMC curve for UV dust correction increases in both the low and high O_{32} bins (Figure 6.3). The discrepancy between the Calzetti and the SMC results is largest in the lowest O_{32} bin, as these galaxies are also more dusty, and hence the effect of any uncertainty in their dust correction is enhanced. The different trends of the Calzetti and the SMC stacks show the importance of systematic uncertainties associated with UV dust corrections (Section 6.4.4).

To see whether galaxies with undetected [OII] are intrinsically different than the [OII] detected objects, we stack the spectra of undetected [OII] objects (detected in [OIII]). We normalize the spectra of individual galaxies to their [OIII] luminosity, calculate the normalized [OII] luminosity of the composite spectrum, and correct it for dust attenuation by measuring $E(B-V)_{\rm neb}$ from the Hβ composite spectrum, normalized to Hα luminosity (assuming the Cardelli extinction curve, Section 6.3.1). The stack is shown in Figure 6.3 and indicates similar O_{32} and $\xi_{\rm ion}$ as the rest of the sample with $O_{32} \lesssim 3$. The [OII] line in 35% of the undetected [OII] objects lie very close to a sky line. This fraction for the detected [OII] sample is 25%. A high fraction of contamination by sky lines implies that the [OII] line is not necessarily intrinsically faint in [OII] undetected objects.

The top panel of Figure 6.4 shows the galaxies in the [OIII]/Hβ versus [NII]/Hα N2-BPT diagram color coded by $\log(\xi_{\rm ion})$. The position of galaxies in the N2-BPT diagram is indicative of both the stellar ionizing radiation field and the conditions of the gas in the star-forming regions. A higher ionization parameter increases O3 and keeps N2 almost constant at N2 $\lesssim -0.9$ (low metallicity, Kewley et al. 2013). In agreement with this statement, in

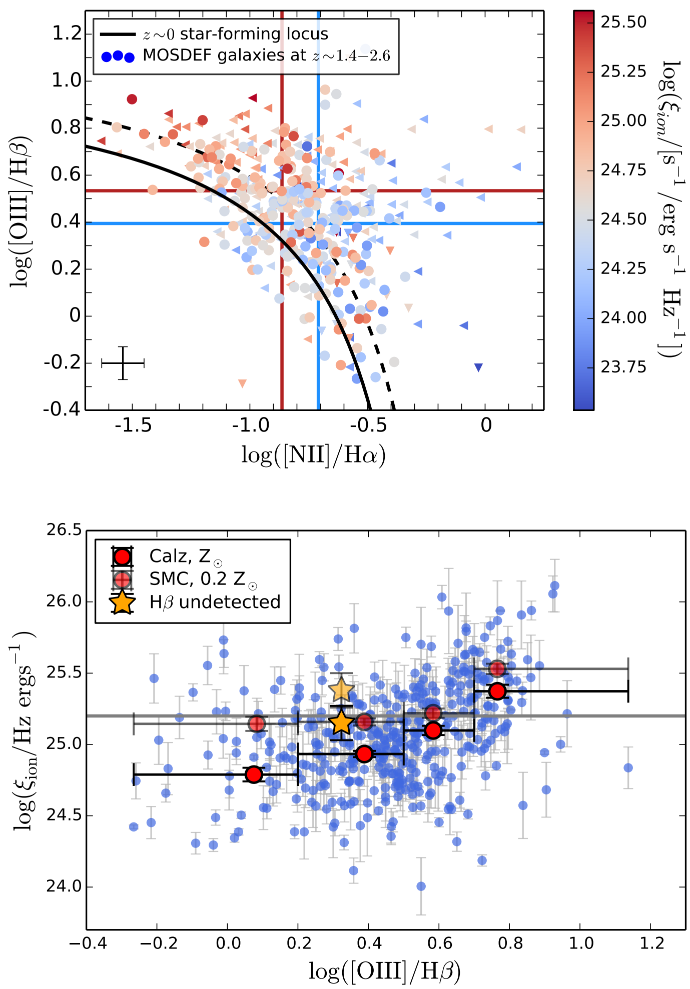

Figure 6.4 (*Top:*) change of $\xi_{\rm ion}$ across the N2 BPT diagram. As a reference, we show the locus of star-forming galaxies at $z \sim 0$ (Kewley et al. 2013) with a black solid line. $\xi_{\rm ion}$ in both plots is measured with the assumption of the Calzetti attenuation curve for UV dust correction. Circles denote objects with $> 3\,\sigma$ detection in all four lines. Downward triangles are $3\,\sigma$ upper limits on [OIII]/Hβ, where [OIII] is not detected. Triangles pointing to the left show $3\,\sigma$ upper limits on [NII]/Hα, where [NII] is not detected. The error bar on the corner indicates the typical uncertainties. $\xi_{\rm ion}$ is enhanced at high [OIII]/Hβ and low [NII]/Hα. The horizontal and vertical lines show average [OIII]/Hβ and [NII]/Hα, respectively, for upper (red) and lower (blue) half of $\xi_{\rm ion}$ distribution. The distribution is the same for the sample with only $z > 2$ galaxies. The $z < 2$ sample is not large enough to statistically constrain the relation. The dashed line is the shifted $z \sim 0$ sequence to divide the sample in two bins with equal number of galaxies. There is no change in the average $\xi_{\rm ion}$ above and below the dashed curve. (*Botton:*) Dependence of $\xi_{\rm ion}$ on [OIII]/Hβ. The red symbols are weighted averages of $\xi_{\rm ion}$ in bins of [OIII]/Hβ. The yellow star indicates the stack of Hβ undetected galaxies (the stack is performed in a similar manner to the [OII] undetected galaxies explained earlier in Section 6.4.2), which has a lower $\xi_{\rm ion}$ compared to that of the highest [OIII]/Hβ bin. The horizontal line shows $\log(\xi_{\rm ion}/[{\rm s^{-1}/erg\,s^{-1}\,Hz^{-1}}]) = 25.2$ from Robertson et al. (2013).

Figure 6.4-top we also see that $\xi_{\rm ion}$ increases with increasing O3 at low N2. On the other hand, a *harder* ionizing radiation field has a larger fraction of ionizing photons to enhance [N II] and [O III] and increases both O3 and N2. Some studies have suggested that the offset of $z \sim 2$ galaxies from the locus of $z \sim 0$ star-forming galaxies in N2-BPT diagram (seen in Figure 6.4-top) is due to a harder stellar ionizing radiation field (Steidel et al. 2014; Steidel et al. 2016; Strom et al. 2017). To examine whether $\xi_{\rm ion}$ varies with the offset from the BPT star-forming sequence, we shift the $z \sim 0$ locus (adopted from Kewley et al. 2013) towards higher O3 and higher N2, such that our sample with detected diagnostic lines is divided in equal numbers. There are 125 galaxies on each side of the shifted sequence, shown with dashed curve in Figure 6.4. The average $\xi_{\rm ion}$ above and below the shifted sequence are respectively $\log(\xi_{\rm ion}/[{\rm s^{-1}/erg\,s^{-1}\,Hz^{-1}}]) = 25.07 \pm 0.03$ and 25.04 ± 0.03, suggesting no change in the hardness of ionizing radiation with the offset from the $z \sim 0$ sequence.

In summary, Figures 6.3 and 6.4 indicate an increase of the production efficiency of ionizing photons in star-forming galaxies with high ionization parameter (high O3, Figure 6.4; high O_{32}, Figure 6.3) at low metallicities (low N2, Figure 6.4). Similar to the conditions in high O_{32}, high O3 may also be indicative of density bounded systems, and hence, in such galaxies Hα underestimates $\xi_{\rm ion}$.

We note that a part of the strong relations between $\xi_{\rm ion}$ with O3 and N2 might be affected by the fact that the same emission lines, Hα and Hβ, are used in $\xi_{\rm ion}$, O3, and N2. The relation between $\xi_{\rm ion}$ and O_{32} is immune from this degeneracy, as the two quantities are derived completely independently.

We further investigate the only three objects in the lower-right part of the BPT diagram that have $\log(\xi_{\rm ion}/[{\rm s^{-1}/erg\,s^{-1}\,Hz^{-1}}]) > 25.5$ (Figure 6.4-top). Their high $\xi_{\rm ion}$ is inconsistent with their location in the low excitation and high metallicity corner of the BPT diagram. The elevated $\xi_{\rm ion}$ cannot be explained by low stellar metallicity, as the three galaxies have high N2 values (low measurement uncertainty, ~ 0.05 dex). The Hβ line of the highest $\xi_{\rm ion}$ object among the three (with $\log(\xi_{\rm ion}/[{\rm s^{-1}/erg\,s^{-1}\,Hz^{-1}}]) = 25.72$) is located close to a sky line and is marginally detected at $S/N = 3.2$, which leads to an uncertain nebular dust correction ($E(B-V)_{\rm neb} = 1.12 \pm 0.11$) and [OIII]/H$\beta$ ratio ($\log([{\rm O\,III}]/{\rm H}\beta) = -0.011 \pm 0.017$). Its SED-inferred UV slope ($\beta = 0.24$) is also not consistent with the observed UV slope ($\beta = -1.78$), making its UV dust correction uncertain as well. The other two objects with $\log(\xi_{\rm ion}/[{\rm s^{-1}/erg\,s^{-1}\,Hz^{-1}}]) = 25.62$ and 25.54, have robust line measurements with high S/N. They are fairly massive ($M_* \sim 10^{10.6}\,{\rm M_\odot}$) and old (age ~ 3 Gyr, assuming an exponentially rising star-formation history with $\tau = 5$ Gyr), which suggests that a starburst is not driving a high value of $\xi_{\rm ion}$. The last possibility to explain the elevated $\xi_{\rm ion}$ is a shallow IMF that produces large fraction of hot ionizing stars leading to a high ratio of ionizing to non-ionizing photons. These two objects are interesting targets for follow-up rest-UV observations to directly trace their ionizing radiation and explore the physical reason of their inconsistent high $\xi_{\rm ion}$ with low O3 and high N2.

6.4.3 $\xi_{\rm ion}$ evolution with cosmic time and stellar mass

One motivation for constraining $\xi_{\rm ion}$ is that it is an important input of cosmic reionization models. To see whether our measurements of $\xi_{\rm ion}$ at $z \sim 2$ can be extended to

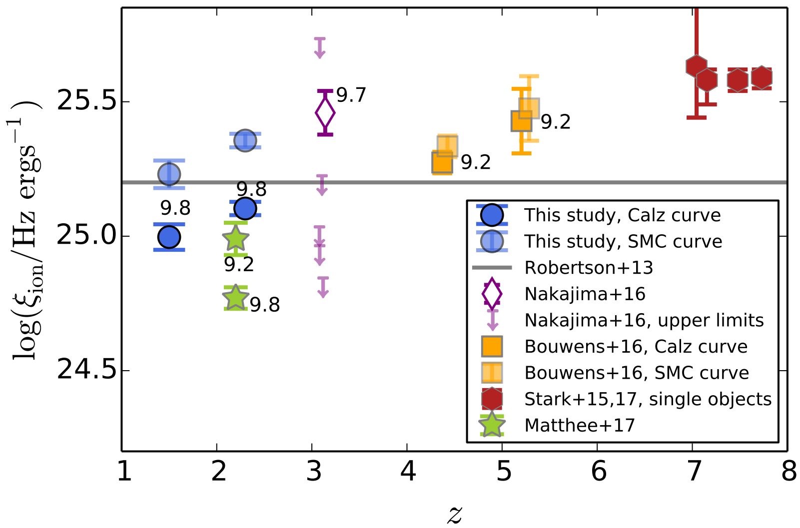

Figure 6.5 Ionizing photon production efficiency as a function of redshift. Our measurements in two redshift bins are shown with blue symbols. We include $\xi_{\rm ion}$ measurements from the literature at different redshifts. For details of each study refer to the text. The numbers next to the markers indicate average mass of the samples. We limit our samples to $\log(M_*/{\rm M}_\odot) < 10.3$ to obtain a more similar mass distribution to that of other high-redshift studies.

$z \gtrsim 6$ galaxies, we compare our results with the studies of higher redshift galaxies from the literature.

In Figure 6.5, the blue symbols are our $\xi_{\rm ion}$ measurements at $z \sim 1.5$ and 2.3, corrected for UV attenuation using the Calzetti (solid blue) and SMC (light blue) curves. To make our sample more similar to that of higher redshift studies, we only take galaxies with $\log(M_*/{\rm M}_\odot) < 10.3$ into consideration. This upper mass limit is chosen to match the maximum mass limit of the Bouwens et al. (2016a) sample at $z \sim 4.4$. Our sample has still a higher average mass than that of Bouwens et al. (2016a), as our sample lacks galaxies with $\log(M_*/{\rm M}_\odot) < 9.0$. The numbers next to the markers in Figure 6.5 indicate the average masses of each sample.

In Figure 6.5, we also show the results of Matthee et al. (2017) at $z \sim 2$ (green stars), which is from a large sample of Hα emitters from a narrow-band survey to estimate $\xi_{\rm ion}$ corrected for dust attenuation based on stellar mass. The two symbols show two different subsamples with different stellar masses indicated in black font next to the markers.

Nakajima et al. (2016) use Hβ luminosity with an assumption of no dust attenuation to estimate $\xi_{\rm ion}$ for a small sample of 15 Lyα emitters (LAEs) and Lyman break galaxies (LBGs) at $z \sim 3$. 12 of their objects are LAEs (plus one AGN and two LBGs), which poses a strong sample selection bias as LAEs occupy different parts of the BPT diagram and have different ionization properties (e.g., Nakajima et al. 2013; Erb et al. 2016). We show the average $\xi_{\rm ion}$ of their detected Hβ sample along with the $3\,\sigma$ upper limits of the undetected ones with purple symbols. They discussed that by assuming the same stellar and nebular color-excess, the median $E(B-V) = 0.03$ derived from SED modeling with an SMC curve, decreases their $\xi_{\rm ion}$ values by ~ 0.1 dex.

The orange squares in Figure 6.5 are from Bouwens et al. (2016a), who estimated Hα from IRAC photometry at $z \sim 4-5$. In the absence of Hβ measurements, Hα luminosities were dust-corrected using stellar reddening derived from SED fitting. The high redshift red symbols in Figure 6.5 are the Stark et al. (2015) and Stark et al. (2017) measurements of four luminous, young, metal-poor galaxies at $z \sim 7$ using UV metal lines. The elevated $\xi_{\rm ion}$ values are not necessarily typical of high-redshift galaxies, as they were pre-selected to have extremely large [OIII]+Hβ equivalent widths. They also have Lyα detection, although the IGM is expected to be significantly neutral at $z = 7-9$. Therefore, Stark et al. (2017) concluded that the hard radiation field of these objects likely reduces the covering fraction

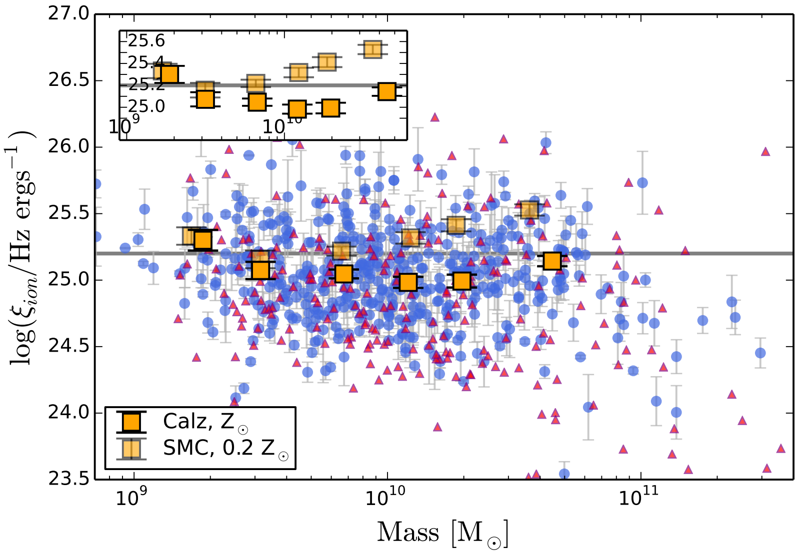

Figure 6.6 Dependence of $\xi_{\rm ion}$ on stellar mass. The symbols are the same as in Figure 6.1.

of neutral hydrogen in the circum-galactic medium and allows transmission of Lyα. The unique selection criteria of these galaxies makes it nontrivial to compare them with our sample at $z \sim 2$ in the context of $\xi_{\rm ion}$ redshift evolution.

Although at first sight, Figure 6.5 suggests a redshift evolution of increasing $\xi_{\rm ion}$ at higher redshifts, an important caveat of the analysis is that each sample is tracing galaxies over different stellar masses. To determine to what extend $\xi_{\rm ion}$ is affected by stellar mass, we stack our sample in bins of mass in Figure 6.6. $\xi_{\rm ion}$ is almost constant at high masses but the 0.23 ± 0.10 dex increase in the lowest mass bin may be indicative of a mass dependency of $\xi_{\rm ion}$. The weak trend of $\xi_{\rm ion}$ with stellar mass is also seen in predictions from simulations (Wilkins et al. 2016). We cannot test whether the observed increase of $\xi_{\rm ion}$ at lower masses persists, as the MOSDEF sample is only complete to $10^9\,M_\odot$. Future studies with *James Webb Space Telescope* (*JWST*) will be specifically useful to span the dynamical range of such studies to lower masses and constrain the redshift evolution of $\xi_{\rm ion}$ in a more robust manner. However, as discussed in Section 6.4.4, the UV dust attenuation curve remains a significant uncertainty in assessing $\xi_{\rm ion}$.

6.4.4 Systematic uncertainties of dust attenuation

An important aspect of Figures 6.1-6.6 is the systematic uncertainty in $\xi_{\rm ion}$ associated with the choice of attenuation curve for the UV dust correction. In all of the plots we show calculations of $\xi_{\rm ion}$ using both the Calzetti curve with a solar metallicity (solid symbols) and an SMC curve with sub-solar metallicity (light symbols). The latter assumption is motivated by recent studies that suggest an SMC curve with a bluer intrinsic β is more appropriate for high-redshift galaxies (Reddy et al. 2017).

Using an SMC curve systematically increases $\xi_{\rm ion}$ by $\sim 0.1 - 0.4$ dex. The discrepancy is larger for more dusty and massive galaxies (see Figure 6.1 and 6.6). Using a single attenuation curve for all galaxies with such a wide range of mass and dustiness is probably not realistic. If the shape of dust attenuation curve varies with galaxy properties (as has been shown in other studies, such as Noll et al. 2009; Kriek & Conroy 2013; Reddy et al. 2015; Salmon et al. 2016), it would affect the trends we see between $\xi_{\rm ion}$ and galaxy parameters. For example, it has been suggested that for young galaxies a curve that is steeper than the Calzetti curve provides a better agreement with IR observations (Reddy et al. 2006a; Siana et al. 2009; Reddy et al. 2010; Shivaei et al. 2015a; Shivaei et al. 2017). A more recent study of Reddy et al. (2017) suggested an SMC curve for massive galaxies and an attenuation curve steeper than SMC for young and low-mass galaxies at $z \sim 2$. A steeper attenuation curve leads to lower UV dust attenuation and higher $\xi_{\rm ion}$. For simplicity, in this

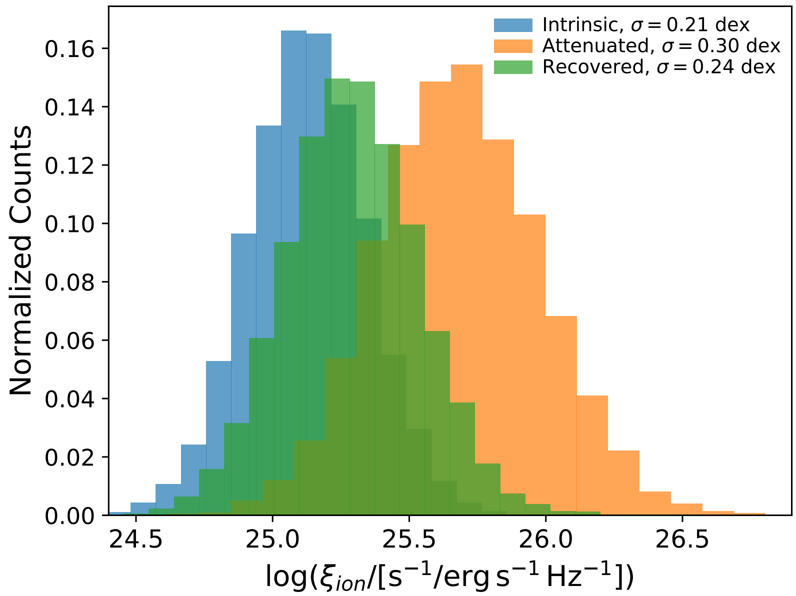

Figure 6.7 Simulation of a $\xi_{\rm ion}$ distribution with an intrinsic scatter of 0.21 dex. The distribution is shown in blue. To test the effect of galaxy-to-galaxy variations of the dust attenuation curve in the $\xi_{\rm ion}$ scatter, we attenuated each object with a different attenuation curve (orange) and corrected the dust obscured luminosities this time by assuming a single attenuation curve (green). The recovered scatter is larger than the intrinsic one, which introduces a ~ 0.1 dex uncertainty in the measured scatter of $\xi_{\rm ion}$ distribution.

study we use a single attenuation curve for the entire sample and present results of both the Calzetti and SMC curves throughout the analysis. Future UV and IR observations are needed to shed more light on this issue.

6.5 Scatter in $\xi_{\rm ion}$

In the previous sections, we focused on the average values of $\xi_{\rm ion}$ either as a function of galaxy properties at $z \sim 2$ or throughout cosmic time. Another important aspect of our study is that we have individual measurements of $\xi_{\rm ion}$, which enables us to study the underlying physics that causes the scatter in the $\xi_{\rm ion}$ distribution.

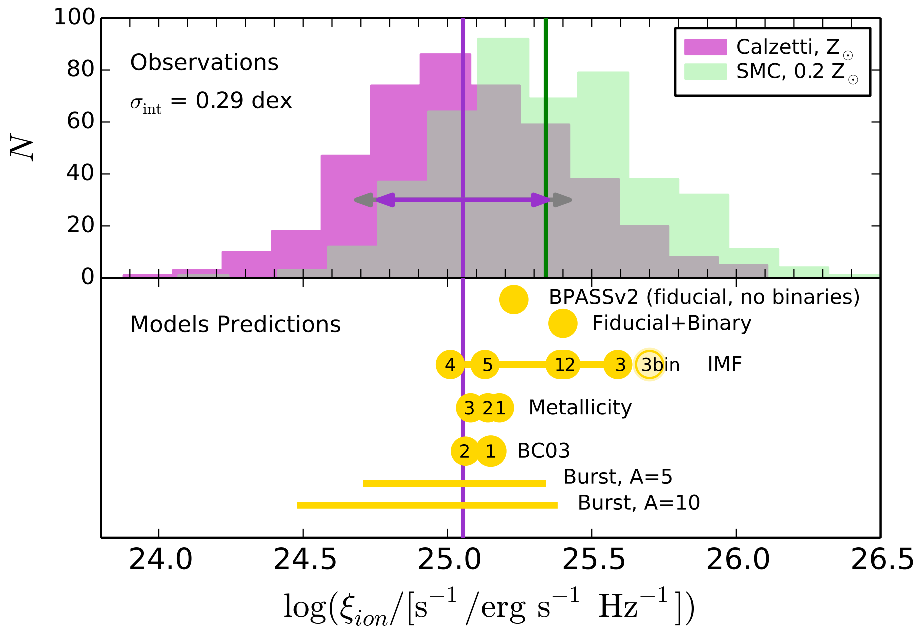

Figure 6.8 *Top:* distribution of $\xi_{\rm ion}$ for our whole sample of $1.4 \leq z \leq 2.6$ galaxies, assuming the Calzetti attenuation curve for the UV dust correction in violet and an SMC curve in green. The observed and intrinsic (i.e., measurement-subtracted) scatters are 0.37 and 0.29 dex for the Calzetti distribution and are shown with grey and violet arrows, respectively. Vertical lines show the averages of the sample. Assuming an SMC curve systematically increases $\xi_{\rm ion}$ by ~ 0.3 dex, indicating the sensitivity of $\xi_{\rm ion}$ measurements on the assumed UV attenuation curve. *Bottom:* $\xi_{\rm ion}$ predictions from stellar population models of BPASSv2 and BC03. Each row shows the variation of $\xi_{\rm ion}$ by changing the labeled quantity in the model, described in detail in Table 6.1. Numbers refer to the model assumptions reported in Table 6.1. The transparent marker (labeled 3bin, $\log(\xi_{\rm ion}/[{\rm s^{-1}/erg\,s^{-1}\,Hz^{-1}}]) = 25.70$) is the IMF model #3 in Table 6.1 including binary evolution.

Figure 6.8 shows the distribution of $\xi_{\rm ion}$ for the MOSDEF galaxies at $1.4 \leq z \leq 2.6$ (top panel). The observed scatter is 0.37 dex (0.35 dex) assuming a Calzetti (SMC) attenuation curve for the UV dust correction (shown with grey arrow in Figure 6.8). The average measurement uncertainty, which is dominated by the uncertainty in Hα and Hβ luminosities, is 0.22 dex. Subtracting the measurement uncertainty from the observed scatter in quadrature results in an "intrinsic" scatter of 0.29 dex (0.27 dex) assuming a Calzetti (SMC) attenuation curve for UV dust correction (shown with purple arrow in Figure 6.8). In the following two sections we investigate the effect of the galaxy-to-galaxy variations of attenuation curve (Section 6.5.1) and massive star populations (Section 6.5.2) on the scatter in $\xi_{\rm ion}$.

6.5.1 Galaxy-to-galaxy Variations in the Dust Attenuation Curve

Other than the measurement uncertainties, another source of uncertainty in the scatter of $\xi_{\rm ion}$ is caused by neglecting the galaxy-to-galaxy variations in the dust attenuation curve. To estimate the uncertainty caused by the assumption of a single attenuation curve for all galaxies (the Calzetti or SMC for the stellar attenuation and the Cardelli for the nebular attenuation), we perform a simple test as follows. We simulate distributions of dust-corrected intrinsic Hα and UV luminosities and calculate the distribution of $\xi_{\rm ion}$ accordingly with an intrinsic scatter of 0.21 dex and average value of $\log(\xi_{\rm ion}/[{\rm s^{-1}/erg\,s^{-1}\,Hz^{-1}}]) = 25.13$ (blue histogram in Figure 6.7). Given the Hα and UV luminosity of each galaxy, we predict stellar and nebular $E(B-V)$ using the empirical relations we derived based on our sample between L(Hα)-$E(B-V)_{\rm nebular}$ and L(UV)-$E(B-V)_{\rm stellar}$ with an assumed scatter in each relation. Then, we attenuate each individual galaxy with a different attenuation curve (κ_λ)

randomly picked between that of the Reddy et al. (2015) and the Calzetti curve for L(Hα) and the Reddy et al. (2015) and the SMC curve for L(UV). The curves were chosen such that we cover the maximum range of κ_λ based on the commonly used attenuation curves. The result is shown as a green histogram in Figure 6.7 with 0.30 dex scatter, which is similar to the scatter in the observed uncorrected $\xi_{\rm ion}$ distribution. In the final step, we recover the dust-corrected values this time by assuming a single attenuation curve for all galaxies—the Calzetti curve for UV and the Cardelli curve for Hα. The recovered scatter is 0.24 dex, shown with the orange histogram in Figure 6.7.

Subtracting the intrinsic and the recovered scatters introduces ~ 0.1 dex uncertainty in the $\xi_{\rm ion}$ scatter due to neglecting the galaxy-to-galaxy variations in the attenuation curve. However, the uncertainty cannot solely explain the large 0.29 dex measurement-subtracted scatter. Subtracting 0.1 dex uncertainty from 0.29 dex scatter in quadrature results in a 0.27 dex scatter.

6.5.2 Galaxy-to-galaxy Variations in Properties of Massive Star Populations

As shown in the previous section, there is a large intrinsic scatter of 0.29 dex in the $\xi_{\rm ion}$ distribution that cannot be explained by either the measurement uncertainties or the galaxy-to-galaxy variations of the dust attenuation curve. We explore the potential physical sources of the scatter by investigating the predictions from the stellar population synthesis (SPS) models of Bruzual & Charlot (2003, hereafter BC03) and the BPASSv2 models (Eldridge & Stanway 2016; Stanway et al. 2016). To determine the predicted $\xi_{\rm ion}$ from an SPS model, we integrate λL_λ below 912 Å, divide by hc, where h is Planck's constant and c is the speed of light, to convert the integrated value to the rate of ionizing photons, and divide the rate of ionizing photons to UV luminosity density (L_ν) at 1500 Å. The predicted values for a range of IMF parameters, metallicities, star-formation histories, and the effect of binaries are shown in Table 6.1 and the bottom panel of Figure 6.8.

The commonly-used BC03 model for a Salpeter IMF, a constant star formation history, and $Z = 0.02$ ($1.5\,Z_\odot$, based on the most recent solar abundances, Asplund et al. 2009) predicts $\log(\xi_{\rm ion}/[{\rm s^{-1}/erg\,s^{-1}\,Hz^{-1}}]) = 25.06$. The BPASSv2 model with the same assumptions produce a similar value of $\log(\xi_{\rm ion}/[{\rm s^{-1}/erg\,s^{-1}\,Hz^{-1}}]) = 25.08$.

Our fiducial BPASSv2 model without binary evolution, assuming a Salpeter IMF, a constant star formation history, and a sub-solar metallicity ($0.15\,Z_\odot$) predicts $\log(\xi_{\rm ion}/[{\rm s^{-1}/erg\,s^{-1}\,Hz^{-1}}]) = 25.23$. Including binaries in the fiducial model leads to an even higher $\xi_{\rm ion}$ by $\sim 50\%$. The effect of binary evolution is to transfer mass and angular momentum from the massive star to its less-massive companion. This transfer causes the companion to spin faster, which leads to rotational mixing of its layers and more efficient burning of hydrogen in its interior (e.g., Cantiello et al. 2007; de Mink et al. 2013). Consequently, the main-sequence lifetime increases and the star becomes hotter, which increases $\xi_{\rm ion}$ compared to that of a single star evolution (Stanway et al. 2016).

Bursts of star formation result in the largest change of $\xi_{\rm ion}$, from $\log(\xi_{\rm ion}/[{\rm s^{-1}/erg\,s^{-1}\,Hz^{-1}}]) = 24.7$ to 25.3 for a burst of $5\,{\rm M_\odot\,yr^{-1}}$ on top of a constant star formation history of $1\,{\rm M_\odot\,yr^{-1}}$. Due to different timescales of Hα and UV light (Kennicutt & Evans 2012; Shivaei et al. 2015b), at the onset of a burst there are more ionizing photons produced at a given UV luminosity and hence a larger $\xi_{\rm ion}$, while after the end of the burst the ratio of ionizing to non-ionizing fluxes decreases. A burst with a higher amplitude of $10\,\mathrm{M_\odot\,yr^{-1}}$ would cause a larger variation in $\xi_{\rm ion}$, but such strong bursts are not likely for the mass range of our galaxies (e.g. Hopkins et al. 2014; Domínguez et al. 2015).

Variations in the stellar metallicity also change $\xi_{\rm ion}$, with lower metallicity models producing higher $\xi_{\rm ion}$. Low metallicity stars have higher effective temperatures and harder ionizing radiations due to less metal blanketing, an effect through which high energy photons are absorbed by metals in stellar atmospheres. Higher metal opacity in low metallicity massive stars also causes lower mass loss rate due to winds, and hence increases the main sequence lifetime of low metallicity stars (Maeder & Conti 1994). Also, at low metallicity the Hayashi limit, an almost vertical line on the HR diagram that denotes the largest radius that a star at a given mass can have in order to maintain hydrostatic equilibrium, moves to higher temperatures (Elias et al. 1985). In our models, changing the stellar metallicity from $0.15\,Z_\odot$ to $1.5\,Z_\odot$ (based on most recent solar abundances, Asplund et al. 2009), results in $\sim 40\%$ change in ionizing photon production efficiency.

Variations in the slope and the upper mass cutoff of IMF result in large change of 0.58 dex in $\xi_{\rm ion}$. We change the slope of high mass end from -2.00 to -2.70. We also consider both 100 and $300\,\mathrm{M_\odot}$upper mass cutoffs. The latter is motivated by observational evidence for the presence of stars with masses $> 150\,\mathrm{M_\odot}$in nearby star clusters (Crowther et al. 2010; Smith et al. 2016). An IMF with a shallower slope of the high mass end and/or a higher upper mass cutoff results in a larger fraction of hot and massive stars. The highest $\xi_{\rm ion}$ value among our assumed parameter space belongs to a binary model with the shallowest IMF slope ($\alpha = -2.0$), upper mass cutoff of $300\,\mathrm{M_\odot}$, and a subsolar metallicity

($0.15\,Z_\odot$). The predicted $\xi_{\rm ion}$ for this model is $\log(\xi_{\rm ion}/[{\rm s^{-1}/erg\,s^{-1}\,Hz^{-1}}]) = 25.70$ and is shown with a light yellow circle in Figure 6.8.

The assumed dust attenuation curve for the UV stellar continuum correction causes a large *systematic* uncertainty of ~ 0.3 dex, as shown with green and violet histograms in Figure 6.8. However, as shown above the galaxy-to-galaxy variation of the dust attenuation curve does not significantly contribute to the scatter of the $\xi_{\rm ion}$ distribution (~ 0.1 dex). Therefore, we conclude that the measurement-subtracted intrinsic scatter of 0.29 dex that we measure for the $\xi_{\rm ion}$ distribution is indicative of variations in the stellar population of individual galaxies, such as variations in the IMF, stellar metallicity, star formation history, stellar population age, and binary/single evolutionary pathways for massive stars.

6.6 Summary

We use a large sample of 672 galaxies from the MOSDEF sample with Hα and Hβ spectroscopic measurements at $z = 1.37 - 2.61$ to constrain the ionizing photon production efficiency, $\xi_{\rm ion}$. We use dust-corrected Hα to calculate the rate of ionizing photons, and divide that by UV luminosity at 1500 Å, dust-corrected using SED-derived color-excess, to estimate $\xi_{\rm ion}$. Our main results are as follows.

- We find an enhanced value of $\xi_{\rm ion}$ in galaxies with blue observed UV slope ($\log(\xi_{\rm ion}/[{\rm s^{-1}/erg\,s^{-1}\,Hz^{-1}}]) = 25.34 \pm 0.08$ at $\beta = -2.1$, Section 6.4.1). These blue-β and low-mass galaxies are more similar to high-redshift galaxies that are thought to be the main drivers of cosmic reionization. Based on this assumption, we conclude

Table 6.1 $\xi_{\rm ion}$ Predictions from SPS Models

SPS Model	IMF [[i] α, $M_*^{\rm max}/{\rm M}_\odot$]	SFH	Z	Binary	$\log(\xi_{\rm ion}/[1/{\rm erg\,Hz^{-1}}])$
BPASSv2 (*Fiducial, F*)	[-2.35, 100]	Constant over 300 Myr	0.002 ($0.15\,Z_\odot$)	No	25.23
(F)	(F)	(F)	(F)	Yes	25.40
(F)	[-2.35, 300]	(F)	(F)	Yes	25.59
(F)	1) [-2.35, 300] 2) [-2.00, 100] 3) [-2.00, 300] 4) [-2.70, 100] 5) [-2.70, 300]	(F)	(F)	(F)	25.39 25.41 25.59* 25.01 25.13
(F)	(F)	(F)	1) 0.006 2) 0.01 3) 0.02	(F)	25.18 25.14 25.08
BC03	(F)	(F)	1) 0.004 2) 0.02	(F)	25.15 25.06
BC03	(F)	Burst 1) [ii]A=5, D=100 Myr 2) A=10, D=100 Myr	0.004	(F)	[24.72 – 25.33] [24.49 – 25.37]

From left to right, the columns indicate: SPS model, IMF, star formation history, metallicity, whether binary stars are included in the models, and the predicted $\xi_{\rm ion}$. Entries with (F) mean the parameter is the same as the fiducial model (first row).

[i] α is the IMF slope from $0.5\,{\rm M}_\odot$ to $M_*^{\rm max}$, the upper mass cutoff.

[ii] A and D are the amplitude and the duration of the burst, respectively. The bursts are simulated on top of a constant star formation of $1\,{\rm M}_\odot\,{\rm yr}^{-1}$. For example, A=5 means there is a burst with amplitude of 5 times the underlying SFR. * The highest $\xi_{\rm ion}$ value in our parameter space is $\log(\xi_{\rm ion}/[{\rm s^{-1}/erg\,s^{-1}\,Hz^{-1}}]) = 25.70$ for the BPASSv2 model with binary evolution, an IMF slope of -2.0, upper mass cutoff of $300\,{\rm M}_\odot$, and $Z = 0.002$. The value is shown with a transparent circle marker labeled *3bin* in Figure 6.8.

that if $\log(\xi_{\rm ion}/[{\rm s^{-1}/erg\,s^{-1}\,Hz^{-1}}]) = 25.34 \pm 0.08$, then the average escape fraction must be $f_{\rm esc} = 14\% \pm 4\%$ to keep the universe ionized at $z > 6$.

- We show that $\xi_{\rm ion}$ is almost constant at $\mathrm{O_{32}} \lesssim 3$ and increases by $\sim 70\%$ at $\mathrm{O_{32}} \sim 5$ to $\log(\xi_{\rm ion}/[{\rm s^{-1}/erg\,s^{-1}\,Hz^{-1}}]) = 25.33 \pm 0.07$ (Section 6.4.2). The increase is consistent with our expectations as both quantities trace ionization parameter. However, if high $\mathrm{O_{32}}$ galaxies are density-bounded, then Hα would under-predict the ionizing luminosity.

- In the N2 BPT diagram, our results show an increase of the production efficiency of ionizing photons at high ionization parameter (high [OIII]/Hβ) and low metallicity (low [NII]/Hα, Figure 6.4). $\xi_{\rm ion}$ does not change with the offset from the BPT $z \sim 0$ star-forming locus, suggesting no change in the hardness of ionizing radiation with the offset from the $z \sim 0$ sequence (Section 6.4.2).

- We do not see a strong correlation between $\xi_{\rm ion}$ and stellar mass. However, there is a 0.23 ± 0.10 dex increase of $\xi_{\rm ion}$ in the lowest mass bin with $\langle M_* \rangle = 10^{9.3}\,{\rm M_\odot}$(Figure 6.6). Samples with a wider range in mass that span to $M_* < 10^9\,{\rm M_\odot}$are needed to complete the picture.

- We compare our results at $z \sim 1.5$ and 2.3 with higher-redshift studies. As the samples are tracing galaxies with different stellar masses, it is not trivial to conclude robustly whether the redshift evolution in Figure 6.5 is indicative of $\xi_{\rm ion}$ evolution or is caused by sample selection biases (Section 6.4.3).

- We investigate the sources of the large *intrinsic* (i.e., measurement uncertainty subtracted) scatter of 0.29 dex in the $\xi_{\rm ion}$ distribution by investigating the galaxy-to-galaxy variations in dust attenuation curve, IMF, stellar metallicity, star formation burstiness, and binary/single eovlutionary paths (Section 6.5, Figure 6.7). We show that galaxy-to-galaxy variations in dust attenuation curve introduce ~ 0.1 dex uncertainty in the scatter (Section 6.4.4). We conclude that the remaining 0.27 dex scatter originates from galaxy-to-galaxy variations in the stellar population properties of our galaxies (Section 6.5.2), as follows. Binary evolution increases $\xi_{\rm ion}$ predictions from SPS models by $\sim 50\%$. Variations in the upper mass cutoff and the slope of the IMF cause a large variation in $\xi_{\rm ion}$ by 0.58 dex, as a higher IMF upper mass cutoff and shallower slope increases the fraction of hot and massive ionizing stars. $\xi_{\rm ion}$ also varies by stellar metallicity and is lower in metal-poor galaxies, mainly due to the decreased affect of metal blanketing. A starburst with an amplitude of 5 times the underlying star formation rate can change $\xi_{\rm ion}$ from $\log(\xi_{\rm ion}/[{\rm s^{-1}/erg\,s^{-1}\,Hz^{-1}}]) = 24.7$ to 25.3. However, a high frequency of strong bursts is unlikely for most of our galaxies with masses $\gtrsim 10^{9.5}\,{\rm M_\odot}$.

- We demonstrate that even with robust dust-corrected Hα measurements and $N({\rm H^0})$ estimates, the UV dust attenuation curve is an important source of uncertainty in $\xi_{\rm ion}$ measurements. An SMC curve with intrinsically blue UV slope (a result of a sub-solar metallicity assumption), systematically increases $\xi_{\rm ion}$ estimates by as large as 0.4 dex compared to the results of the shallower Calzetti curve with solar abundances. The systematic change is shown in all Figures 6.1-6.6. A more realistic mass-dependent

UV dust attenuation curve, such that the curve is steeper for low-mass galaxies than massive ones, would affect our results and enhance the $\xi_{\rm ion}$ variations we observe as a function of mass and β (Section 6.4.4). This systematic uncertainty is very important to consider in future rest-optical observations with *JWST*.

We thank Rychard Bouwens and George Rieke for helpful comments. Funding for the MOSDEF survey is provided by NSF AAG grants AST-1312780, 1312547, 1312764, and 1313171 and archival grant AR-13907, provided by NASA through a grant from the Space Telescope Science Institute. The data presented herein were obtained at the W.M. Keck Observatory, which is operated as a scientific partnership among the California Institute of Technology, the University of California and the National Aeronautics and Space Administration. The Observatory was made possible by the generous financial support of the W.M. Keck Foundation. The authors wish to recognize and acknowledge the very significant cultural role and reverence that the summit of Maunakea has always had within the indigenous Hawaiian community. We are most fortunate to have the opportunity to conduct observations from this mountain.

Chapter 7

Epilogue

We have made significant progress in calibrating the commonly-used star formation rate indicators and better understanding mass assembly, dust enrichment, and characteristics of massive stars in galaxies at $z \sim 2$. We constrained the properties of SFR-M_* relation, the variations of the mid-IR dust emission in different environments, and production efficiency of ionizing photons. We demonstrated that uncertainties associated with the assumed dust attenuation curve and stellar population synthesis model dominate the variations in the ratio of ionizing (Hα) to non-ionizing (UV) emission. Despite these advancements, there are a number of issues that remain unresolved but are critical towards our understanding of star formation and mass assembly at $z \gtrsim 2$.

A population of galaxies that is widely missed from the MOSDEF sample and the works presented in this thesis is faint and low-mass galaxies ($M_* \lesssim 10^9\,\mathrm{M}_\odot$). Faint and low-mass galaxies are important pieces in the galaxy formation and evolution puzzle, as they are abundant in the universe and contribute significantly to the chemical enrichment of the intergalactic medium. The slope of SFR-M_*, which we measured in Chapters 3 and 5 (limited to $M_* \sim 10^{9.5-11}\,M_\odot$), is shallower than the unity slope predicted from simulations (Davé 2008; Sparre et al. 2015a). Based on models, a shallow slope of 0.6 cannot hold down to low masses with $M_* \lesssim 109.5\,M_\odot$, as it would lead to a too rapid evolution in the stellar mass function (Weinmann et al. 2012; Ilbert et al. 2013). Therefore, it is expected that the slope flattens as we move towards lower masses. Another puzzling characteristic of the low-mass galaxies is their star formation histories. Simulations predict that star formation in low-mass galaxies is stochastic (Hopkins et al. 2014; Sparre et al. 2015b; Domínguez et al. 2015). Studying the star formation stochasticity is essential for our understanding of galaxy evolution, as the feedback from star formation bursts affects the ionizing flux escape fraction, as well as the strength of the observed nebular lines. Moreover, galaxies with low masses and low metallicities are assumed to contribute significantly to the cosmic reionization at $z \gtrsim 6$ (Robertson et al. 2013; Bouwens et al. 2015). Hence, constraining their ionizing photon production efficiency and escape fraction is crucial for better understanding the reionization era. The launch of *JWST* will be of major importance for addressing these questions. *JWST* NIRSpec and NIRCam instruments will provide higher sensitivities and wider wavelength coverages that enable us to address the aforementioned questions and extend the studies presented in this thesis to lower masses and higher redshifts. Advancements in this area, specifically regarding measurements of star formation burstiness and ionizing photon production efficiency and escape fraction, may also be achieved by incorporating rest-frame UV spectra and utilizing spectral features that are sensitive to the presence of massive stars and ages of starbursts (Leitherer et al. 1995; Shapley et al. 2003; Reddy et al. 2016b; Stark et al. 2017).

Other open issues include the formation and destruction mechanisms of dust grains, the physical explanation of the observed low PAH intensity in metal-poor environments, the properties of PAH molecules at high redshift, including the PAH charge, size, and molecular structure, as well as temperature and type of the source. Studying PAH properties at high redshifts will help us reveal valuable information about the ISM conditions and stellar populations of early galaxies. Progress on this front requires simultaneous observations of multiple mid-IR aromatic bands (as opposed to a single emission at 7.7 μm with *Spitzer*/MIPS). The Mid-Infrared Instrument (MIRI) onboard *JWST* with nine photometric bands from 5 to 28 μm will push the boundaries of our knowledge about dust and PAHs at $z \sim 1-2$, owing to its significantly higher sensitivity and spacial resolution compared to our current facilities.

Another urgent question that remains is the appropriate dust attenuation curve that applies to high-redshift galaxies. The assumption of a single attenuation curve for the entire population of high-redshift galaxies that spans a wide range in mass and specific SFR is not realistic. With the current datasets from rest-UV and rest-optical spectroscopic surveys, we start to empirically derive average dust attenuation curves and characterize important features in the curves, such as the ubiquity (or lack) of the 2175Å extinction feature at high redshifts. However, to properly constrain dustiness (i.e., IR to UV luminosity ratio) in high-redshift galaxies, we need to increase the resolution of our far-IR photometry and directly trace the peak of IR emission at $z \sim 1-3$, which will not be feasible in a foreseeable future.

Bibliography

Adelberger, K. L., Steidel, C. C., Shapley, A. E., et al. 2004, ApJ, 607, 226 [2.2.1]

Aird, J., Coil, A. L., Moustakas, J., et al. 2012, /apj, 746, 90 [3.3.4]

Asplund, M., Grevesse, N., Sauval, A. J., & Scott, P. 2009, Annual Review of Astronomy and Astrophysics, 47, 481 [5.3, 6.5.2]

Atek, H., Kneib, J.-P., Pacifici, C., et al. 2014, ApJ, 789, 96 [3.1, 3.5, 3.6, 5.5.1]

Azadi, M., Coil, A. L., Aird, J., et al. 2017, ApJ, 835, 27 [5.2.1, 6.2.1]

Baldwin, J. A., Phillips, M. M., & Terlevich, R. 1981, PASP, 93, 5 [5.3.1, 6.4.2]

Bavouzet, N., Dole, H., Le Floc'h, E., et al. 2008, A&A, 479, 83 [5.5, 5.5.2]

Behroozi, P. S., Wechsler, R. H., & Conroy, C. 2013b, ApJ, 770, 57 [3.1]

Beintema, D. A., van den Ancker, M. E., Molster, F. J., et al. 1996, A&A, 315, L369 [5.6]

Boersma, C., Hony, S., & Tielens, A. G. G. M. 2006, A&A, 447, 213 [5.6]

Bouwens, R. J., Illingworth, G. D., Oesch, P. A., et al. 2015, ApJ, 811, 140 [6.1, 6.1, 6.4.1, 7]

Bouwens, R. J., Smit, R., Labbé, I., et al. 2016a, ApJ, 831, 176 [1.2, 6.1, 6.4.1, 3, 6.4.3]

Bouwens, R. J., Illingworth, G. D., Oesch, P. A., et al. 2010, ApJL, 709, L133 [2.1]

Bouwens, R. J., Aravena, M., Decarli, R., et al. 2016b, ApJ, 833, 72 [6.2.3]

Brammer, G. B., van Dokkum, P. G., & Coppi, P. 2008, ApJ, 686, 1503 [3.3.1]

Brammer, G. B., van Dokkum, P. G., Franx, M., et al. 2012, ApJS, 200, 13 [3.2.4]

Brinchmann, J., Charlot, S., White, S. D. M., et al. 2004, MNRAS, 351, 1151 [3.3]

Brown, S. 2011, World Applied Programming, 1, 288 [5.8]

Bruzual, G., & Charlot, S. 2003, MNRAS, 344, 1000 [3.2.4, 5.2.3, 6.2.3, 6.5.2]

Calzetti, D., Armus, L., Bohlin, R. C., et al. 2000, ApJ, 533, 682 [1.1.1, 2.1, 2.2.2, 2.5, 2.6, 3, 3.2.4, 3.5.1, 4.3, 6.2.3, 6.3]

Calzetti, D., Kinney, A. L., & Storchi-Bergmann, T. 1994, ApJ, 429, 582 [2.1, 3.5.1]

Calzetti, D., Kennicutt, R. C., Engelbracht, C. W., et al. 2007, ApJ, 666, 870 [5.1]

Cantiello, M., Yoon, S.-C., Langer, N., & Livio, M. 2007, A&A, 465, L29 [6.5.2]

Capak, P. L., Carilli, C., Jones, G., et al. 2015, Nature, 522, 455 [6.2.3]

Caputi, K. I., Lagache, G., Yan, L., et al. 2007, ApJ, 660, 97 [5.5, 5.5.2]

Cardelli, J. A., Clayton, G. C., & Mathis, J. S. 1989, ApJ, 345, 245 [1.1.1, 2.1, 2.5, B, 3.2.4, 3.4, 3.5.1, 4.2, 5.2.2, 5.2.3, 6.2.2, 6.3]

Cau, P. 2002, A&A, 392, 203 [5.6]

Chabrier, G. 2003, PASP, 115, 763 [3.1, 3.2.4, 4.1, 5.1, 5.2.3, 5.5.2, 6.1, 6.2.3]

Chary, R., & Elbaz, D. 2001, ApJ, 556, 562 [2.4, 2.4, 4.2, 4.4, 5.1, 5.2, 5.2.6]

Chen, H.-W., Prochaska, J. X., & Gnedin, N. Y. 2007, ApJL, 667, L125 [6.4.1]

Cherchneff, I. 2006, A&A, 456, 1001 [5.6]

Choi, J., Conroy, C., & Byler, N. 2017, ApJ, 838, 159 [6.1]

Cid Fernandes, R., Mateus, A., Sodré, L., Stasińska, G., & Gomes, J. M. 2005, MNRAS, 358, 363 [2.1]

Coil, A. L., Aird, J., Reddy, N., et al. 2015, ApJ, 801, 35 [3.2.2, 4.2, 5.2.1, 6.2.1]

Conroy, C. 2013, Annual Review of Astronomy and Astrophysics, 51, 393 [4.1]

Conroy, C., & Gunn, J. E. 2010, ApJ, 712, 833 [4.3]

Conroy, C., Gunn, J. E., & White, M. 2009, ApJ, 699, 486 [4.1, 4.3]

Cook, D. O., Dale, D. A., Johnson, B. D., et al. 2014, MNRAS, 445, 899 [5.1]

Crowther, P. A., Schnurr, O., Hirschi, R., et al. 2010, MNRAS, 408, 731 [6.5.2]

Daddi, E., Dickinson, M., Morrison, G., et al. 2007a, ApJ, 670, 156 [3.1, 3.5, 5.1, 5.5.1]

Dale, D. A., & Helou, G. 2002, ApJ, 576, 159 [2.4, 2.4, 5.2, 5.2.6, 5.5.2]

Dale, D. A., Cohen, S. A., Johnson, L. C., et al. 2009, ApJ, 703, 517 [1.1.2, 5.1]

Darvish, B., Sobral, D., Mobasher, B., et al. 2014, ApJ, 796, 51 [3.6, 5.5.1]

Davé, R. 2008, MNRAS, 385, 147 [5.5.1, 7]

Davé, R., Finlator, K., & Oppenheimer, B. D. 2012, MNRAS, 421, 98 [3.4]

Davé, R., Oppenheimer, B. D., & Finlator, K. 2011a, MNRAS, 415, 11 [3.1, 5.5.1]

Davé, R., Thompson, R., & Hopkins, P. F. 2016, MNRAS, 462, 3265 [5.5.1]

De Barros, S., Reddy, N., & Shivaei, I. 2016, ApJ, 820, 96 [6.3]

de Barros, S., Schaerer, D., & Stark, D. P. 2014, A&A, 563, A81 [2.1]

de Mink, S. E., Langer, N., Izzard, R. G., Sana, H., & de Koter, A. 2013, ApJ, 764, 166 [6.5.2]

Dickinson, M., & FIDEL Team. 2007, in Bulletin of the American Astronomical Society, Vol. 39, American Astronomical Society Meeting Abstracts, 822 [5.2.4]

Dickinson, M., Giavalisco, M., & GOODS Team. 2003, in The Mass of Galaxies at Low and High Redshift, ed. R. Bender & A. Renzini, 324 [2.2.3]

Domínguez, A., Siana, B., Brooks, A. M., et al. 2015, MNRAS, 451, 839 [3.4, 3.7, 4.1, 6.5.2, 7]

Donley, J. L., Koekemoer, A. M., Brusa, M., et al. 2012, ApJ, 748, 142 [5.2.1, 6.2.1]

Draine, B. T., & Li, A. 2007, ApJ, 657, 810 [4.3]

Draine, B. T., Dale, D. A., Bendo, G., et al. 2007b, ApJ, 663, 866 [5.1, 5.3.1, 5.6]

Duncan, K., & Conselice, C. J. 2015, MNRAS, 451, 2030 [6.1, 6.4.1]

Dunne, L., Ivison, R. J., Maddox, S., et al. 2009, MNRAS, 394, 3 [3.5]

Dutton, A. A., van den Bosch, F. C., & Dekel, A. 2010, MNRAS, 405, 1690 [3.1, 3.4, 3.7, 5.5.1]

Dwek, E. 2005, in American Institute of Physics Conference Series, Vol. 761, The Spectral Energy Distributions of Gas-Rich Galaxies: Confronting Models with Data, ed. C. C. Popescu & R. J. Tuffs, 103–122 [5.4, 5.6]

Elbaz, D., Dickinson, M., Hwang, H. S., et al. 2011, A&A, 533, A119 [2.4, 4.1, 4.2, 5.1, 5.2.4, 5.3.1, 5.5.2]

Eldridge, J. J., & Stanway, E. R. 2016, MNRAS, 462, 3302 [6.5.2]

Elias, J. H., Frogel, J. A., & Humphreys, R. M. 1985, ApJS, 57, 91 [6.5.2]

Engelbracht, C. W., Gordon, K. D., Rieke, G. H., et al. 2005, ApJL, 628, L29 [5.1, 5.3.1, 5.6]

Engelbracht, C. W., Rieke, G. H., Gordon, K. D., et al. 2008, ApJ, 678, 804 [5.3]

Erb, D. K., Pettini, M., Steidel, C. C., et al. 2016, ApJ, 830, 52 [6.4.3]

Erb, D. K., Shapley, A. E., Pettini, M., et al. 2006a, ApJ, 644, 813 [2.3.1, 2.1]

Erb, D. K., Steidel, C. C., Shapley, A. E., et al. 2006, ApJ, 646, 107 [1.1.3]

Erb, D. K., Steidel, C. C., Shapley, A. E., et al. 2006c, ApJ, 647, 128 [2.1, 2.3, 2.3.1, 2.5, 5.5.1]

Fadely, R., Allam, S. S., Baker, A. J., et al. 2010, ApJ, 723, 729 [5.3]

Fioc, M., & Rocca-Volmerange, B. 1997, A&A, 326, 950 [2.1]

Förster Schreiber, N. M., Genzel, R., Bouché, N., et al. 2009, ApJ, 706, 1364 [2.1, 2.5]

Frenklach, M., & Feigelson, E. D. 1989, ApJ, 341, 372 [5.6]

Fumagalli, M., Labbé, I., Patel, S. G., et al. 2014, ApJ, 796, 35 [5.1]

Furlong, M., Bower, R. G., Theuns, T., et al. 2015, MNRAS, 450, 4486 [5.5.1]

Galliano, F. 2011, in EAS Publications Series, Vol. 46, EAS Publications Series, ed. C. Joblin & A. G. G. M. Tielens, 43–48 [5.4]

Galliano, F., Dwek, E., & Chanial, P. 2008, ApJ, 672, 214 [5.1, 5.3.1, 5.4, 5.6]

Garn, T., & Best, P. N. 2010, MNRAS, 409, 421 [2.1, 2.5, 3.5.1, 3.8, 3.6]

Giammanco, C., Beckman, J. E., & Cedrés, B. 2005, A&A, 438, 599 [6.4.2]

Gordon, K. D., Clayton, G. C., Misselt, K. A., Landolt, A. U., & Wolff, M. J. 2003, ApJ, 594, 279 [1.1.1, C, E, 6.2.3]

Grazian, A., Giallongo, E., Paris, D., et al. 2017, A&A, 602, A18 [6.4.1]

Grogin, N. A., Kocevski, D. D., Faber, S. M., et al. 2011, ApJS, 197, 35 [3.2.1, 4.2, 5.2.1, 6.2.1]

Gruppioni, C., Pozzi, F., Rodighiero, G., et al. 2013, MNRAS, 432, 23 [5.5.2]

Guiderdoni, B., & Rocca-Volmerange, B. 1987, A&A, 186, 1 [2.1]

Haynes, B. S., & Wagner, H. G. 1981, Progress in Energy and Combustion Science, 7, 229 [1.1.2]

Hayward, C. C., Lanz, L., Ashby, M. L. N., et al. 2014, MNRAS, 445, 1598 [3.1, 4.1]

Hemmati, S., Miller, S. H., Mobasher, B., et al. 2014, ApJ, 797, 108 [3.7]

Hirashita, H., Buat, V., & Inoue, A. K. 2003, A&A, 410, 83 [2.6.1]

Hopkins, A. M., & Beacom, J. F. 2006, ApJ, 651, 142 [5.5.2]

Hopkins, P. F., Keres, D., Oñorbe, J., et al. 2014, MNRAS, 445, 581 [3.4, 6.5.2, 7]

Hunt, L. K., Izotov, Y. I., Sauvage, M., & Thuan, T. X. 2011, in EAS Publications Series, Vol. 46, EAS Publications Series, ed. C. Joblin & A. G. G. M. Tielens, 143–148 [5.1]

Hunt, L. K., Thuan, T. X., Izotov, Y. I., & Sauvage, M. 2010, ApJ, 712, 164 [5.1, 5.3.1, 5.6]

Ilbert, O., McCracken, H. J., Le Fèvre, O., et al. 2013, A&A, 556, A55 [7]

Ilbert, O., Arnouts, S., Le Floc'h, E., et al. 2015, A&A, 579, A2 [4.1]

Inoue, A. K. 2002, ApJL, 570, L97 [6.3, 1]

Isobe, T., Feigelson, E. D., Akritas, M. G., & Babu, G. J. 1990, ApJ, 364, 104 [3.3.2]

Japelj, J., Vanzella, E., Fontanot, F., et al. 2017, MNRAS, 468, 389 [6.4.1]

Jaskot, A. E., & Oey, M. S. 2013, ApJ, 766, 91 [6.4.2]

Jones, T., Martin, C., & Cooper, M. C. 2015, ApJ, 813, 126 [5.2.2, 5.3, 5.3.1]

Kannan, R., Stinson, G. S., Macciò, A. V., et al. 2014, MNRAS, 437, 3529 [3.1, 5.5.1]

Karim, A., Schinnerer, E., Martnez-Sansigre, A., et al. 2011, ApJ, 730, 61 [3.5]

Kennicutt, R. C. 1998, Annual Review of Astronomy and Astrophysics, 36, 189 [1.1.1, 2, 2.1, 2.3.1, 2.3.2, 2.4, 2, 2.5, 2.6.1, 2.6.1, 3.2.4, 3.4, 4.2, 4.4, 4.5, 5.2.3, 5.5.2]

Kennicutt, R. C., & Evans, N. J. 2012, Annual Review of Astronomy and Astrophysics, 50, 531 [1.1.1, 3.4, 6.5.2]

Kennicutt, Jr., R. C. 1998, ApJ, 498, 541 [5.5.1]

Kennicutt, Jr., R. C., Tamblyn, P., & Congdon, C. E. 1994, ApJ, 435, 22 [2.6.1]

Kennicutt, Jr., R. C., Hao, C.-N., Calzetti, D., et al. 2009, ApJ, 703, 1672 [4.4]

Kewley, L. J., Dopita, M. A., Leitherer, C., et al. 2013, ApJ, 774, 100 [5.3.1, 6.4.2, 6.4]

Koekemoer, A. M., Faber, S. M., Ferguson, H. C., et al. 2011, ApJS, 197, 36 [3.2.1, 4.2, 5.2.1, 6.2.1]

Koyama, Y., Smail, I., Kurk, J., et al. 2013, MNRAS, 434, 423 [3.6, 5.5.1]

Kriek, M., & Conroy, C. 2013, ApJL, 775, L16 [6.4.4]

Kriek, M., van Dokkum, P. G., Franx, M., Illingworth, G. D., & Magee, D. K. 2009, ApJL, 705, L71 [2.1]

Kriek, M., van Dokkum, P. G., Franx, M., et al. 2007, ApJ, 669, 776 [2.1]

—. 2008, ApJ, 677, 219 [1.1.3]

Kriek, M., Shapley, A. E., Reddy, N. A., et al. 2015, ApJS, 218, 15 [1.1.3, 1, 2.7, 3.1, 3.2.1, 3.2.3, 3.2.4, 1, 3.3.1, 4.1, 4.2, 5.1, 5.2.1, 5.2.2, 6.1, 6.2.1, 6.2.2]

Latter, W. B. 1991, ApJ, 377, 187 [5.4, 5.6]

Law, D. R., Steidel, C. C., Shapley, A. E., et al. 2012, ApJ, 759, 29 [2.2.1]

Lee, N., Sanders, D. B., Casey, C. M., et al. 2015, ApJ, 801, 80 [3.6]

Leitherer, C., & Heckman, T. M. 1995, ApJS, 96, 9 [6.3]

Leitherer, C., Robert, C., & Heckman, T. M. 1995, ApJS, 99, 173 [7]

Leja, J., van Dokkum, P. G., Franx, M., & Whitaker, K. E. 2015, ApJ, 798, 115 [5.5.1]

Lutz, D., Poglitsch, A., Altieri, B., et al. 2011, A&A, 532, A90 [4.2]

Ma, X., Kasen, D., Hopkins, P. F., et al. 2015, MNRAS, 453, 960 [6.4.1]

Madau, P. 1995, ApJ, 441, 18 [4.3]

Madau, P., & Dickinson, M. 2014, Annual Review of Astronomy and Astrophysics, 52, 415 [1.1, 2.1, 5.5.2, 6.1]

Madau, P., Haardt, F., & Rees, M. J. 1999, ApJ, 514, 648 [6.1]

Madau, P., Pozzetti, L., & Dickinson, M. 1998, ApJ, 498, 106 [2.1, 2.5, 2.6.1]

Madden, S. C., Galliano, F., Jones, A. P., & Sauvage, M. 2006, A&A, 446, 877 [5.1, 5.6]

Maeder, A., & Conti, P. S. 1994, ARA&A, 32, 227 [6.5.2]

Magdis, G. E., Rigopoulou, D., Huang, J.-S., & Fazio, G. G. 2010, MNRAS, 401, 1521 [3.4]

Magdis, G. E., Rigopoulou, D., Helou, G., et al. 2013, A&A, 558, A136 [5.1]

Magnelli, B., Elbaz, D., Chary, R. R., et al. 2011, A&A, 528, A35 [2.4, 5.5.2]

Magnelli, B., Popesso, P., Berta, S., et al. 2013, A&A, 553, A132 [4.2, 5.2.4]

Matthee, J., Sobral, D., Best, P., et al. 2017, MNRAS, 465, 3637 [6.1, 6.4.3]

McLean, I. S., Steidel, C. C., Epps, H. W., et al. 2012, in Society of Photo-Optical Instrumentation Engineers (SPIE) Conference Series, Vol. 8446, Society of Photo-Optical Instrumentation Engineers (SPIE) Conference Series, 0 [1.1.3, 3.1, 3.2.1, 4.1, 5.2.1, 6.2.1]

Meurer, G. R., Heckman, T. M., & Calzetti, D. 1999, ApJ, 521, 64 [3.2.4]

Mitra, S., Davé, R., & Finlator, K. 2015, MNRAS, 452, 1184 [4.1]

Mobasher, B., Dahlen, T., Ferguson, H. C., et al. 2015, ApJ, 808, 101 [4.1]

Momcheva, I. G., Brammer, G. B., van Dokkum, P. G., et al. 2016, ApJS, 225, 27 [4.2, 4.3, 5.2.1, 5.2.3, 6.2.1, 6.2.3]

Muzzin, A., van Dokkum, P., Kriek, M., et al. 2010, ApJ, 725, 742 [2.1]

Nakajima, K., Ellis, R. S., Iwata, I., et al. 2016, ApJL, 831, L9 [6.1, 6.4.3]

Nakajima, K., & Ouchi, M. 2014, MNRAS, 442, 900 [6.4.2]

Nakajima, K., Ouchi, M., Shimasaku, K., et al. 2013, ApJ, 769, 3 [6.4.3]

Nayyeri, H., Mobasher, B., Hemmati, S., et al. 2014, ApJ, 794, 68 [3.1]

Nestor, D. B., Shapley, A. E., Kornei, K. A., Steidel, C. C., & Siana, B. 2013, ApJ, 765, 47 [6.4.1]

Noeske, K. G., Weiner, B. J., Faber, S. M., et al. 2007a, ApJL, 660, L43 [3.1, 4.1, 5.5.1]

Noll, S., Pierini, D., Cimatti, A., et al. 2009, A& A, 499, 69 [6.3, 6.4.4]

Nordon, R., Lutz, D., Shao, L., et al. 2010, A&A, 518, L24 [2.4, 5.5.2]

Normand, P., Rouan, D., Lacombe, F., & Tiphene, D. 1995, Astronomy and Astrophysics, 297, 311 [5.1]

O'Halloran, B., Satyapal, S., & Dudik, R. P. 2006, ApJ, 641, 795 [5.6]

Oke, J. B., & Gunn, J. E. 1983, ApJ, 266, 713 [2.1, 6.1]

Oliver, S. J., Wang, L., Smith, A. J., et al. 2010, A&A, 518, L21 [4.2]

Osterbrock, D. E. 1989, Astrophysics of gaseous nebulae and active galactic nuclei [6.3]

Pannella, M., Carilli, C. L., Daddi, E., et al. 2009, ApJL, 698, L116 [3.1, 3.5]

Peeters, E., Spoon, H. W. W., & Tielens, A. G. G. M. 2004, ApJ, 613, 986 [5.6]

Penston, M. V., Robinson, A., Alloin, D., et al. 1990, A&A, 236, 53 [6.4.2]

Pérez-González, P. G., Rieke, G. H., Egami, E., et al. 2005, ApJ, 630, 82 [5.5.2]

Pérez-Montero, E. 2014, MNRAS, 441, 2663 [5.3.1]

Pettini, M., & Pagel, B. E. J. 2004, MNRAS, 348, L59 [5.2.2]

Price, S. H., Kriek, M., Brammer, G. B., et al. 2014, ApJ, 788, 86 [2.1]

Reddy, N., Dickinson, M., Elbaz, D., et al. 2012a, ApJ, 744, 154 [2.2.3, 2.4, 2.4, 4.1, 5.3.2, 5.5.2]

Reddy, N. A., Erb, D. K., Pettini, M., Steidel, C. C., & Shapley, A. E. 2010, ApJ, 712, 1070 [1.1.1, 2.1, 2.2.3, 2.2.3, 2.3.1, 2.4, 2.5, 2.6.2, 2.7, 3.5.1, 4.2, 5.1, 5.2.4, 5.5, 5.5.2, 6.4.4]

Reddy, N. A., Pettini, M., Steidel, C. C., et al. 2012b, ApJ, 754, 25 [2.2.1, 2.2.2, 2.3.2, 2.6.1, 3.1, 3.5, 5.1, 5.2.3, 5.5.1, 6.2.3, 6.3]

Reddy, N. A., & Steidel, C. C. 2009, ApJ, 692, 778 [2.1, 3.1, 6.2, 6.4.1]

Reddy, N. A., Steidel, C. C., Erb, D. K., Shapley, A. E., & Pettini, M. 2006b, ApJ, 653, 1004 [2.6.2, 2.7, 3.3, 3.3.1, 5.5.1]

Reddy, N. A., Steidel, C. C., Fadda, D., et al. 2006a, ApJ, 644, 792 [2.2.1, 3.1, 5.1, 6.4.4]

Reddy, N. A., Steidel, C. C., Pettini, M., et al. 2008, ApJS, 175, 48 [5.5.2]

Reddy, N. A., Steidel, C. C., Pettini, M., & Bogosavljević, M. 2016a, ApJ, 828, 107 [6.3]

Reddy, N. A., Steidel, C. C., Pettini, M., Bogosavljević, M., & Shapley, A. E. 2016b, ApJ, 828, 108 [6.1, 6.3, 7]

Reddy, N. A., Kriek, M., Shapley, A. E., et al. 2015, ApJ, 806, 259 [3.2.4, 3.5.1, 4.2, 4.3, 5.2.2, 5.2.3, 5.6, 6.1, 6.2.2, 6.2.3, 6.3, 6.4.4, 6.5.1]

Reddy, N. A., Oesch, P. A., Bouwens, R. J., et al. 2017, ArXiv e-prints, arXiv:1705.09302 [6.2.3, 6.4.4]

Rieke, G. H., Alonso-Herrero, A., Weiner, B. J., et al. 2009, ApJ, 692, 556 [2.4, 2.4, 5.1, 5.2, 5.2.6, 5.5.2]

Rigby, J. R., Marcillac, D., Egami, E., et al. 2008, ApJ, 675, 262 [5.3, 5.5]

Riguccini, L., Le Floc'h, E., Ilbert, O., et al. 2011, A&A, 534, A81 [5.5.2]

Robertson, B. E., Ellis, R. S., Furlanetto, S. R., & Dunlop, J. S. 2015, ApJl, 802, L19 [1.2, 6.1, 6.4.1]

Robertson, B. E., Furlanetto, S. R., Schneider, E., et al. 2013, ApJ, 768, 71 [1.2, 6.1, 6.1, 6.4.1, 6.3, 6.4, 7]

Rodighiero, G., Vaccari, M., Franceschini, A., et al. 2010, Astronomy and Astrophysics, 515, A8 [5.5.2]

Rodighiero, G., Daddi, E., Baronchelli, I., et al. 2011, ApJL, 739, L40 [3.1, 3.5]

Rodighiero, G., Renzini, A., Daddi, E., et al. 2014, MNRAS, 443, 19 [4.1]

Sales, D. A., Pastoriza, M. G., & Riffel, R. 2010, ApJ, 725, 605 [5.1]

Salim, S., Rich, R. M., Charlot, S., et al. 2007, ApJS, 173, 267 [5.5.1]

Salmon, B., Papovich, C., Long, J., et al. 2016, ApJ, 827, 20 [6.4.4]

Salpeter, E. E. 1955, ApJ, 121, 161 [2.1, 2.2.2, 2.1, 3]

Sanders, D. B., Mazzarella, J. M., Kim, D.-C., Surace, J. A., & Soifer, B. T. 2003, AJ, 126, 1607 [5.5.2]

Sanders, R. L., Shapley, A. E., Kriek, M., et al. 2015, ApJ, 799, 138 [5.2.2, 6.1]

—. 2016a, ApJ, 816, 23 [5.2.2, 5.3.1, 5.5, 6.1]

Sandstrom, K. M., Bolatto, A. D., Draine, B. T., Bot, C., & Stanimirović, S. 2010, ApJ, 715, 701 [5.6]

Santini, P., Fontana, A., Grazian, A., et al. 2009, A&A, 504, 751 [3.5, 5.5.1]

Sawicki, M. 2012, MNRAS, 421, 2187 [3.1, 3.4]

Schenker, M. A., Ellis, R. S., Konidaris, N. P., & Stark, D. P. 2013, ApJ, 777, 67 [2.1]

Schreiber, C., Pannella, M., Elbaz, D., et al. 2015, A&A, 575, A74 [3.1, 3.8, 3.6, 4.1, 5.5.1]

Seok, J. Y., Hirashita, H., & Asano, R. S. 2014, Monthly Notices of the Royal Astronomical Society, 439, 2186 [5.1]

Shapley, A. E. 2011, Annual Review of Astronomy and Astrophysics, 49, 525 [2.1, 3.1]

Shapley, A. E., Steidel, C. C., Erb, D. K., et al. 2005, ApJ, 626, 698 [2.2.1]

Shapley, A. E., Steidel, C. C., Pettini, M., & Adelberger, K. L. 2003, ApJ, 588, 65 [7]

Shapley, A. E., Reddy, N. A., Kriek, M., et al. 2015, ApJ, 801, 88 [5.2.2, 5.3.1, 6.1]

Sharples, R. M., Bender, R., Lehnert, M. D., et al. 2004, in Society of Photo-Optical Instrumentation Engineers (SPIE) Conference Series, Vol. 5492, Ground-based Instrumentation for Astronomy, ed. A. F. M. Moorwood & M. Iye, 1179–1186 [4.1]

Shim, H., Chary, R.-R., Dickinson, M., et al. 2011, ApJ, 738, 69 [2.1]

Shipley, H. V., Papovich, C., Rieke, G. H., Brown, M. J. I., & Moustakas, J. 2016, ApJ, 818, 60 [5.1]

Shivaei, I., Reddy, N. A., Steidel, C. C., & Shapley, A. E. 2015a, ApJ, 804, 149 [1.2, 3.5.1, 4.1, 4.2, 5.1, 5.5.1, 6.3, 6.4.4]

Shivaei, I., Reddy, N. A., Shapley, A. E., et al. 2015b, ApJ, 815, 98 [1.2, 4.1, 4.2, 6.1, 6.2.2, 6.5.2]

Shivaei, I., Kriek, M., Reddy, N. A., et al. 2016, ApJL, 820, L23 [1.2, 5.2.2, 5.2.3, 5.2.4, 5.3.1, 5.5.1, 5.6, 6.1, 6.2.2, 6.3]

Shivaei, I., Reddy, N. A., Shapley, A. E., et al. 2017, ApJ, 837, 157 [1.2, 6.4.4]

Siana, B., Smail, I., Swinbank, A. M., et al. 2009, ApJ, 698, 1273 [5.3, 6.4.4]

Siana, B., Shapley, A. E., Kulas, K. R., et al. 2015, ApJ, 804, 17 [6.4.1]

Skelton, R. E., Whitaker, K. E., Momcheva, I. G., et al. 2014, ApJS, 214, 24 [3.2.1, 3.2.4, 3.3, 3.4, 3.7, 4.3, 5.2.1, 5.2.2, 5.2.3, 6.1, 6.2.1, 6.2.2, 6.2.3]

Smith, J. D. T., Draine, B. T., Dale, D. A., et al. 2007, ApJ, 656, 770 [1.1.2, 5.1, 5.3, 5.6]

Smith, L. J., Crowther, P. A., Calzetti, D., & Sidoli, F. 2016, ApJ, 823, 38 [6.5.2]

Sobral, D., Best, P. N., Smail, I., et al. 2014, MNRAS, 437, 3516 [3.5, 3.8, 3.6]

Sparre, M., Hayward, C. C., Feldmann, R., et al. 2015b, MNRAS, in press [4.1, 7]

Sparre, M., Hayward, C. C., Springel, V., et al. 2015a, MNRAS, 447, 3548 [3.1, 3.4, 3.7, 5.5.1, 7]

Speagle, J. S., Steinhardt, C. L., Capak, P. L., & Silverman, J. D. 2014, ApJS, 214, 15 [3.1, 3.5.2]

Spitzer, L. 1978, Physical processes in the interstellar medium, doi:10.1002/9783527617722 [6.3]

Stanway, E. R., Eldridge, J. J., & Becker, G. D. 2016, MNRAS, 456, 485 [6.1, 6.4.1, 6.5.2]

Stark, D. P., Schenker, M. A., Ellis, R., et al. 2013, ApJ, 763, 129 [2.1]

Stark, D. P., Walth, G., Charlot, S., et al. 2015, MNRAS, 454, 1393 [6.1, 6.4.3]

Stark, D. P., Ellis, R. S., Charlot, S., et al. 2017, MNRAS, 464, 469 [6.1, 6.4.3, 7]

Steidel, C. C., Adelberger, K. L., Shapley, A. E., et al. 2003, ApJ, 592, 728 [2.2.1, 3.5.2]

Steidel, C. C., Erb, D. K., Shapley, A. E., et al. 2010, ApJ, 717, 289 [2.2.1]

Steidel, C. C., Shapley, A. E., Pettini, M., et al. 2004, ApJ, 604, 534 [2.2.1, 3.5.2]

Steidel, C. C., Strom, A. L., Pettini, M., et al. 2016, ApJ, 826, 159 [6.4.2]

Steidel, C. C., Rudie, G. C., Strom, A. L., et al. 2014, ApJ, 795, 165 [2.1, 3.5.1, 1, 6.3, 6.4.2]

Storey, P. J., & Zeippen, C. J. 2000, MNRAS, 312, 813 [5.2.2]

Strom, A. L., Steidel, C. C., Rudie, G. C., et al. 2017, ApJ, 836, 164 [6.4.2]

Tielens, A. G. G. M. 2005, The Physics and Chemistry of the Interstellar Medium [1.1.2]

Tielens, A. G. G. M. 2008, Annual Review of Astronomy and Astrophysics, 46, 289 [1.1.2, 5.1, 5.4, 5.6]

Tomczak, A. R., Quadri, R. F., Tran, K.-V. H., et al. 2016, ApJ, 817, 118 [5.1]

Torrey, P., Vogelsberger, M., Genel, S., et al. 2014, MNRAS, 438, 1985 [3.1, 3.7, 4.1, 5.5.1]

Trainor, R. F., Strom, A. L., Steidel, C. C., & Rudie, G. C. 2016, ApJ, 832, 171 [6.4.2]

Tremonti, C. A., Heckman, T. M., Kauffmann, G., et al. 2004, ApJ, 613, 898 [5.3.1, 5.5]

Utomo, D., Kriek, M., Labbé, I., Conroy, C., & Fumagalli, M. 2014, ApJL, 783, L30 [3.1, 4.1]

van Dokkum, P. G., Kriek, M., Rodgers, B., Franx, M., & Puxley, P. 2005, ApJL, 622, L13 [2.1]

Vanzella, E., Giavalisco, M., Inoue, A. K., et al. 2010, ApJ, 725, 1011 [6.4.1]

Voit, G. M. 1992, MNRAS, 258, 841 [5.1]

Weinmann, S. M., Pasquali, A., Oppenheimer, B. D., et al. 2012, MNRAS, 426, 2797 [5.5.1, 7]

Whitaker, K. E., van Dokkum, P. G., Brammer, G., & Franx, M. 2012b, ApJL, 754, L29 [3.1, 3.5, 3.5.2]

Whitaker, K. E., Franx, M., Leja, J., et al. 2014b, ApJ, 795, 104 [3.1, 3.8, 3.6, 4.1, 5.1, 5.3, 5.5.1]

Wild, V., Charlot, S., Brinchmann, J., et al. 2011, MNRAS, 417, 1760 [2.1, 6.3]

Wilkins, S. M., Feng, Y., Di-Matteo, T., et al. 2016, MNRAS, 458, L6 [6.4.3]

Williams, R. J., Quadri, R. F., Franx, M., van Dokkum, P., & Labbé, I. 2009, ApJ, 691, 1879 [3.1, 3.2.2]

Wu, Y., Charmandaris, V., Hao, L., et al. 2006, ApJ, 639, 157 [5.3.1]

Wuyts, E., Rigby, J. R., Gladders, M. D., et al. 2012, ApJ, 745, 86 [2.6.2, 2.7]

Wuyts, S., Labbé, I., Schreiber, N. M. F., et al. 2008, ApJ, 682, 985 [4.4, 5.1, 5.3.2]

Wuyts, S., Förster Schreiber, N. M., Lutz, D., et al. 2011a, ApJ, 738, 106 [2.1, 2.2.2, 4.5, 5.1, 5.2.3, 5.3.2]

Wuyts, S., Förster Schreiber, N. M., van der Wel, A., et al. 2011b, ApJ, 742, 96 [3.1, 5.1, 5.5.1]

Wuyts, S., Förster Schreiber, N. M., Nelson, E. J., et al. 2013, ApJ, 779, 135 [3.7]

Yoshikawa, T., Akiyama, M., Kajisawa, M., et al. 2010, ApJ, 718, 112 [2.1]

Zackrisson, E., Bergvall, N., & Leitet, E. 2008, ApJL, 676, L9 [2.1]

Zahid, H. J., Dima, G. I., Kewley, L. J., Erb, D. K., & Dav, R. 2012, ApJ, 757, 54 [3.5, 5.5.1]